REPORT DOCUMENTATION PAGE	*Form Approved* *OMB No. 0704-0188*

1. AGENCY USE ONLY *(Leave blank)*	2. REPORT DATE	3. REPORT TYPE AND DATES COVERED
	25.Jun.02	DISSERTATION

4. TITLE AND SUBTITLE SHEAR LAYER STABILITY IN A TWO DIMENSIONAL DISK	5. FUNDING NUMBERS
6. AUTHOR(S) CAPT WOLVERTON ROBERT H	
7. PERFORMING ORGANIZATION NAME(S) AND ADDRESS(ES) UNIVERSITY OF NEW MEXICO	8. PERFORMING ORGANIZATION REPORT NUMBER CI02-147
9. SPONSORING/MONITORING AGENCY NAME(S) AND ADDRESS(ES) THE DEPARTMENT OF THE AIR FORCE AFIT/CIA, BLDG 125 2950 P STREET WPAFB OH 45433	10. SPONSORING/MONITORING AGENCY REPORT NUMBER

11. SUPPLEMENTARY NOTES

12a. DISTRIBUTION AVAILABILITY STATEMENT Unlimited distribution In Accordance With AFI 35-205/AFIT Sup 1	12b. DISTRIBUTION CODE

13. ABSTRACT *(Maximum 200 words)*

20020702 031

14. SUBJECT TERMS	15. NUMBER OF PAGES 113
	16. PRICE CODE

17. SECURITY CLASSIFICATION OF REPORT	18. SECURITY CLASSIFICATION OF THIS PAGE	19. SECURITY CLASSIFICATION OF ABSTRACT	20. LIMITATION OF ABSTRACT

SHEAR LAYER STABILITY

IN A TWO-DIMENSIONAL DISK

BY

ROBERT H. WOLVERTON

B.S., Engineering Sciences, USAF Academy, 1991

M.S., Aeronautical Engineering, University of Washington, 1992

DISSERTATION

Submitted in Partial Fulfillment of the
Requirements for the Degree of

Doctor of Philosophy in Mathematics

The University of New Mexico
Albuquerque, New Mexico

December, 2001

SHEAR LAYER STABILITY

IN A TWO-DIMENSIONAL DISK

ROBERT H. WOLVERTON

Doctor of Philosophy in Mathematics

December, 2001

DEDICATION

In memory of my brother, Paul F. Wolverton.

His abilities far exceeded my own.

ACKNOWLEDGEMENTS

My heartfelt and deepest appreciation of Professor Evangelos A. Coutsias who provided everything required for this journey from faith and guidance to grit and determination. He is without peer.

I am also grateful for my committee members and their service. Thanks to Prof. McIver, Prof. Hagstrom, Prof. Kapitula, Dr. Romero, and Dr. Alsing. Furthermore, I'd like to thank Dr. Nielsen for his support.

All the best plans require implementation. To that end my sincerest thanks to Ms. Roxanne Littlefield; she can bring any bureaucracy to its knees with a single glance. And a brass ovation for the only men who could solve my perpetual computer dilemma, Mr. Dann "Thaiday" Brewer and Mr. Craig "Duct Tape" Lewis, the most resourceful sys-admins in town.

Thanks to USAFA Dept of Mathematical Sciences for providing me the opportunity to pursue my dream. This work was partially supported by the National Computational Science Alliance under DMS000002N using the alliance AHPCC Linux cluster and by the National Science Foundation under DMS9977396.

SHEAR LAYER STABILITY

IN A TWO-DIMENSINAL DISK

BY

ROBERT H. WOLVERTON

ABSTRACT OF DISSERTATION

Submitted in Partial Fulfillment of the
Requirements for the Degree of

Doctor of Philosophy in Mathematics

The University of New Mexico
Albuquerque, New Mexico

December, 2001

TABLE OF CONTENTS

LIST OF FIGURES

SHEAR LAYER STABILITY
IN A TWO-DIMENSIONAL DISK

by

R. H. Wolverton

B.S., Engineering Sciences, US Air Force Academy, 1991

M.S., Aeronautical Engineering, University of Washington, 1992

Ph.D., Mathematics, University of New Mexico, 2001

ABSTRACT

The dynamics of rotating fluids provide a rich aggregate of periodic, quasi-periodic, and irregular behavior. Many investigations of two-dimensional (2D) flows containing fluid velocity inflections present the Kelvin-Helmholtz (KH) instability. In this investigation we study the saturation of the KH instability for a forced circular shear layer in a differentially rotating split-disk.

Complex vortex interactions are reasonably well understood through experimentation but modeling them requires highly accurate numerical schemes. To explore these flows our investigations employ an efficiently parallelized, highly accurate pseudospectral scheme for the solution of the incompressible Navier-Stokes equations in a disk geometry, Torres & Coutsias [32]. Beyond the initial KH instability, secondary transitions in the flow yield symmetry breaking bifurcations resulting in periodic and irregular states. Simulations are provided for the intermediate states between the $n = 4$ and $n = 3$ vortex braids. Oscillating states not previously seen in numerical studies are reported. Unlike the jump transitions between braids of different order, the oscillating states were found to be supercritical bifurcations and thus, not hysteretic. Period doubling bifurcations are observed during some spin-up studies in which intermediate symmetry breaking bifurcations are bypassed.

Accurate spectral simulation offers the means for systematic exploration of the dynamics associated with rotating fluids. Herein we construct such a scheme and present bifurcation analysis for secondary transitions.

1 Introduction

Rotating shear layers occur in a variety of situations from astronomical phenomena to industrial applications. The Great Red Spot on Jupiter and the Blue Spot on Neptune result from differential rotation associated with sharply sheared zonal flows within their respective atmospheres. Similar vortices are created in Earth's atmosphere through the instabilities of differential velocity associated with fluid propagation. Schär & Davies [28] and Simmons & Hoskins [29] considered weather system evolution and baroclinic front instabilities. Weber & Smith [34] followed the life cycle of tropical cyclones, and additional work by Read *et al* [27] considers these instabilities combined with a temperature gradient. Turbo-machinery within a closed housing produces stresses via instabilities in the shear layer created by the high speed rotation. One example is computer hard drives, and Humphrey & Gore [19] consider the design of these drives and the effects of shear layer instabilities.

In planar and circular 2-D flow the Kelvin-Helmholtz instability arises at a shear layer with an inflection in the fluid's velocity profile. A derivation of the instability is provided in section 1.1. The dynamics associated with the Kelvin-Helmholtz instability apply to both viscid and inviscid fluids with viscosity adding disspative capacity to the fluid as internal friction. Nonlinear evolution of a circular shear layer in a rotating fluid has been investigated in several forms beginning with Stewartson's [30] analysis of a small differential rotation in a strong background flow. Greenspan [17] expanded Stewartson's work by presenting in-depth analysis of rotating fluids. Of particular interest are the zones of vertical fluid transport, the Stewartson layers, that develop near the shear layer in a differentially rotating viscous flow.

Experimental verification of shear layer instabilities has been demonstrated in several geometries. While Tomasini *et al* [31] consider the effects of compressibility, all the work discussed throughout this paper is conducted using low speed, incompressible fluids. Hide & Titman [18] completed experiments in a rotating tank equipped with a differentially rotating disk. Their experiment showed a well defined parameter value for the onset of stability, and a vorticity mode number that decreases as the differential velocity in the disk is increased. Flow within a thin annual region was investigated by

Rabaud & Couder [25] who formulated a correlation between the initial instability and the Reynolds number of the flow. Their work was extended by Chomaz *et al* [6] giving a deeper analysis of the secondary transitions occurring after the initial bifurcation. With an experimental apparatus similar to the one used by Hide & Titman [18], Niino & Misawa [23] characterized the initial nonlinear stability of the flow including Stewartson layers. The effects of both internal viscous dissipation and Ekman pumping are analyzed providing insights about the flow within the Stewartson layer. Konijnenberg *et al* [20] continue the experimental investigations using a parabolic bowl. This non-annular, free surface parabolic bowl allows for the formation of a point vortex flow. In a near disk geometry, Früh & Read [15] experimentally analyze secondary transitions using detailed flow visualization of large scale structures via laser-Doppler velocimetry. Experiments completed by Hide & Titman [18], Niino & Misawa [23], Konijnenberg *et al* [20], and Früh & Read [15] use rotating tanks where the fluid layer is thicker than the Ekman layer thickness. In contrast Rabaud & Couder [25] and Chomaz *et al* [6] impose a restriction on the fluid thickness as less than the Ekman layer thickness.

Recent studies have investigated quasi-two-dimensional (Q2D) flow which includes the effects of bottom friction and the resulting Ekman layer. Problems are classified as Q2D when the vertical fluid velocity is represented by an approximation of the planar velocity. Danilov *et al* [9] validate the Q2D approximation for Ekman and Rayleigh friction by comparing experimental and analytical results. The Stewartson layers which support vertical fluid transport near the shear layer have been investigated by several authors, Hide & Titman [18], Niino & Misawa [23], Konijnenberg *et al* [20], etc. Section 1.2.2 provides a detailed discussion of the Stewartson layers. Energy cascades studied by Manin [21] based on Komolgorov wave numbers give a correlation between the wave number and energy cascade rates. Inverse energy cascade and self-organization dominate the dynamics of a rotating fluid in a bounded domain. Churilov & Shukhman [7] analyze and classify the initial bifurcation from steady, homogeneous rotational flow. Bergeron *et al* [3] use weakly nonlinear stability analysis to validate numerical simulation of the initial bifurcation. A perturbation of the initial flow is applied to the azimuthally symmetric state. The resulting perturbed problem is solved in its linear form giving the critical Reynolds number for the bifurcation from

homogeneous, steady flow. The third order Landau equations of the weakly nonlinear theory yield the form of the bifurcation as a supercritical pitchfork. A linear analysis ignoring viscosity conducted by Konijnenberg *et al* [20] considers the β effect on the initial instability of a rotating fluid.

Secondary bifurcations from a steady n vortex flow have been the focus of several experiments and numerical simulations. Chomaz *et al* [6] following the work of Rabaud & Couder [25] determine two distinctly different forms of instability depending on the initial number of vortices. They explain two examples, $n = 5$ and $n = 4$, in detail. Transition from a solution composed of an even number of vortices begins with the first subharmonic symmetry breaking. For a solution composed of an odd number of vortices the first subharmonic is not discretized along the shear layer so a traveling wave develops. In general the amplification of subharmonic and superharmonic waves precede the secondary transitions. The numerical analysis by Rabaud & Couder [25] and Chomaz *et al* [6] uses a double Fourier grid at low resolution and only captures large scale transitions. Supporting the Chomaz *et al* [6] work, Bergeron *et al* [3] use a Fourier-Chebyshev expansion to provide accurate, spectral numerical simulation of the initial bifurcation in an annular geometry. Investigation by Konijnenberg *et al* [20], also using a Fourier-Chebyshev expansion in an annular domain, yields simulations of the β effect that match their experimental findings. Niino & Misawa [23] study the barotropic instability and find supercriticality of the flow and a decrease in the wavenumber of the solution. However, their analysis predicts increasing and decreasing wavenumbers as the Reynolds number of the flow is increased. Danilov *et al* [9] use a double Fourier expansion to simulate magnetohydrodynamic flow in a rectangular domain with emphasis given to vortex interactions. Früh & Read [15] parameterize their experiment for a wide range of Rossby and Ekman numbers. Using the parameterization particular attention is given to the secondary bifurcation regions and period doubling. The vortices are mapped via particle tracking giving a detailed map for the evolution of a vortex. Manin [21] analyzes the merger of two vortices providing insight into the transition to lower frequency solutions within rotating fluids. Rand [26] described the secondary transitions via symmetry breaking bifurcations. He reports that during the transition the group dimension of initially continuous spatio-temporal symmetries drops by one in essence

collapsing to a non-trivial lattice in the plane. Flow evolution through the transitions is qualified in the following progression: homogeneous, periodic, quasi-periodic, and turbulent.

The Kelvin-Helmholtz instability of a viscous, incompressible fluid is a the starting point for a series of rich bifurcations in the 2D circular geometry. Our circular geometry is not annular but rather is a split disk with forcing introduced through Ekman pumping, see figure 1.1.

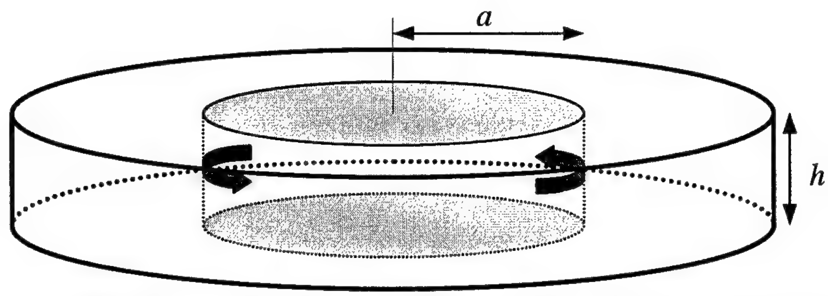

fig 1.1 The disk geometry forced with Ekman pumping from the top and bottom. The shear layer is forced at a distance a *and the height of the cell is* h.

The Ekman pumping is induced by rotating the inner portion of the top and bottom walls. The flow is characterized as Q2D where the vertical fluid transport due to the Ekman forcing is included with a planar approximation. Stability of the initial bifurcation is resolved demonstrating the similarity between the disk and annulus geometries for low Reynolds numbers, and verification of the results is demonstrated both analytically, Bergeron *et al* [3], and experimentally, Früh & Read [15]. Secondary transitions are investigated with emphasis on symmetry breaking bifurcations (including period doubling bifurcations) and periodic states. Using an accurate, pseudospectral scheme, we provide the first simulation of the $4 \oplus 3 \oplus 2$ periodic state and its associated transitions. The notation $4 \oplus 3 \oplus 2$ implies the flow is combination of Fourier modes 4, 3, and 2. The $4 \oplus 3 \oplus 2$ state consists of temporally periodic flow built on the interaction of the $n = 4 \oplus 2$ and $n = 3$ solutions. Also, we provide the first numerical investigation of irregular flow regimes. The irregular flow persists for a narrow range of Reynolds number beyond the $4 \oplus 3 \oplus 2$ periodic state. Finally, we simulate the asymmetric tripole, and introduce the complex nature of its parameter space. The sections of this thesis include (2) Numerics, (3) Stability analysis, and (4) Results.

1.1 Kelvin-Helmholtz instability

This phenomenon results from the intrinsic instability of a sheet vortex to small perturbations. Transition layer instability results in vortex roll-up to the well documented vortex pairing, e.g. Winant & Browand [35]. The Kelvin-Helmholtz instability is characterized by an inflection of the fluid velocity at the critical layer, Chandrasekhar [5]. The inflection creates increasing undulations at the shear layer driving the flow to turbulence in the 3D scenario. An analysis of the instability is presented here to provide background information on a dynamical instability possessed by many unidirectional flows.

A simple model builds upon Bachelor [2] to demonstrate the instability has irrotational flow on both sides of a slightly perturbed vortex sheet. For consistency with the work presented in this paper, the flow is considered within a polar coordinate system. The Kelvin-Helmholtz instability is a local phenomenon, and it suffices to consider a thin sector of the 2-dimensional disk and focus on the area near the shear layer. While the shear layer in the disk geometry has a nontrivial curvature, the shear layer in a thin slice of the flow is nearly linear. The flow is considered in two regions around the vortex sheet, outer and inner see figure 1.2.

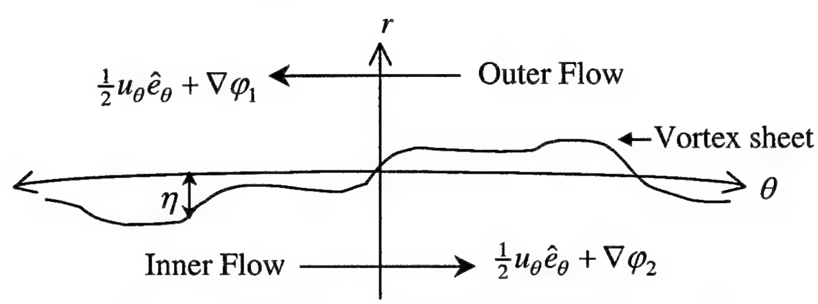

fig 1.2 A perturbed vortex sheet near the shear layer. η is the distance between the vortex sheet and the ideal shear layer.

Since the flow is irrotational and incompressible, the velocity is written in terms of a potential function. The outer flow has a velocity, $\vec{u}_{outer} = -\frac{1}{2}u_\theta\hat{e}_\theta + \nabla\varphi_1$, and the inner flow has a velocity, $\vec{u}_{inner} = \frac{1}{2}u_\theta\hat{e}_\theta + \nabla\varphi_2$, where the disturbance potentials, φ_1 and φ_2, are small. The distance between the slightly deformed vortex sheet and its ideal position constitutes a small perturbation varying with the angle, θ, and with time

$$\eta(\theta,t)$$

All of the small quantities, η, φ_1, and φ_2 are related through the material boundary created by the vortex sheet. A few items to note before continuing are:

1) the gradient of the perturbation is

$$\nabla\eta = \tfrac{1}{r}\partial_\theta \eta$$

2) the total derivative with respect to time is

$$\tfrac{d}{dt} = \partial_t + \bar{u}\cdot\nabla$$

3) the boundary formed by the vortex sheet is located at $a+\eta$ where a is the distance from the center of the disk to the ideal shear layer. Any fluid parameter ξ evaluated at the boundary is written in the form

$$\xi\big|_\partial \equiv \xi\big|_{r=a+\eta}$$

and for the first order approximations the magnitude of the perturbation is nearly zero and the notation for the boundary is defined as

$$\xi\big|_{\bar{\partial}} \equiv \xi\big|_{r=a}$$

We begin by noting the relationship between the perturbation velocity and the gradient of the disturbance potentials in the radial direction. Velocity in the radial directions results from fluctuations in the perturbation and for the outer flow this gives

$$\partial_r\varphi_1\big|_\partial = \tfrac{d\eta}{dt} = \partial_t\eta + \left(-\tfrac{1}{2}u_\theta\hat{e}_\theta + \nabla\varphi_1\right)\Big|_\partial \cdot\nabla\eta$$

which simplifies after completing the dot product

$$\partial_r\varphi_1\big|_\partial = \partial_t\eta - \tfrac{1}{2a}u_\theta\partial_\theta\eta + \tfrac{1}{a}\partial_\theta\varphi_1\partial_\theta\eta$$

Considering the disturbances and the perturbation to be small parameters, the first order approximation for the outer flow velocity gradient in the vertical direction yields

(1.1) $$\partial_r\varphi_1\big|_{\bar{\partial}} = \partial_t\eta - \tfrac{1}{2a}u_\theta\partial_\theta\eta$$

Similarly the radial velocity of the inner flow resulting from the evolution of the vortex sheet perturbation is

(1.2) $$\partial_r\varphi_1\big|_{\bar{\partial}} = \partial_t\eta + \tfrac{1}{2a}u_\theta\partial_\theta\eta$$

In addition to the material connectivity at the vortex sheet, the pressure gradient across the shear layer is zero. As a result the difference in pressure on either side of the vortex sheet is zero. For the incompressible, irrotational flow pressure is given according to

(1.3) $$p = p_0 - \rho\left(\partial_t \varphi + \tfrac{1}{2}\vec{u}\cdot\vec{u}\right)$$

Combining this definition for pressure with the homogeneity of the flow yields continuity for the velocity potential evolution rate across the shear layer. Here is the result via the pressure difference

$$\left.(p_1 - p_2)\right|_\partial = 0 = \left.\partial_t \varphi_1\right|_\partial + \tfrac{1}{2}\left.\vec{u}_{outer}\cdot\vec{u}_{outer}\right|_\partial - \left.\partial_t \varphi_2\right|_\partial - \tfrac{1}{2}\left.\vec{u}_{inner}\cdot\vec{u}_{inner}\right|_\partial$$

and expanding the velocity products gives

$$\left.\partial_t \varphi_1\right|_\partial + \tfrac{1}{2}\left[\left(\partial_r \varphi_1\right)^2 + \tfrac{1}{4}u_\theta^2 - \tfrac{1}{a}u_\theta \partial_\theta \varphi_1 + \tfrac{1}{a^2}\left(\partial_\theta \varphi_1\right)^2\right]_\partial -$$
$$\left.\partial_t \varphi_2\right|_\partial - \tfrac{1}{2}\left[\left(\partial_r \varphi_2\right)^2 + \tfrac{1}{4}u_\theta^2 + \tfrac{1}{a}u_\theta \partial_\theta \varphi_2 + \tfrac{1}{a^2}\left(\partial_\theta \varphi_2\right)^2\right]_\partial = 0$$

The first order approximation for the above equation leaves only the relationship between the time partials for the disturbance potentials and their associated azimuthal gradients. No radial gradients are present in the first order rendering

(1.4) $$\left.\partial_t \varphi_1\right|_{\bar{\partial}} - \left.\partial_t \varphi_2\right|_{\bar{\partial}} - \left.\tfrac{u_\theta}{2a}\partial_\theta \varphi_1\right|_{\bar{\partial}} - \left.\tfrac{u_\theta}{2a}\partial_\theta \varphi_2\right|_{\bar{\partial}} = 0$$

The equations (1.1), (1.2), and (1.4) can be solved if the perturbation and disturbances are expanded with a Fourier basis. It is evident that a sinusoidal dependence of η on θ demands a similar dependence from the disturbance potentials. Thus all the small parameters are represented by the superposition of Fourier modes

$$\eta, \varphi_1, \varphi_2 \propto e^{ik\theta}$$

where each k mode behaves independently. The disturbance potentials are restricted to a subset of the solutions for (1.1), (1.2), and (1.4) through the irrotational nature of the fluid. Namely φ_1 and φ_2 must independently satisfy Laplace's equation

$$\nabla^2 \varphi_j = r^2 \partial_r^2 \varphi_j + r \partial_r \varphi_j + \partial_\theta^2 \varphi_j = 0$$

where $j = 1,2$. In general Laplace's equation in polar coordinates can be solved using a product solution while considering the radial and azimuthal components separately. The solutions are

$$\varphi_1 = \left(c_1 r^k + c_2 r^{-k}\right)e^{ik\theta}$$

$$\varphi_2 = \left(d_1 r^k + d_2 r^{-k}\right)e^{ik\theta}$$

The solutions for φ_1 and φ_2 are consistent with the Fourier modal assumption. To simplify these solutions, we enforce conditions such that the disturbance motion vanishes away from the vortex sheet. Thus the outer flow disturbance potential vanishes for increasing values of r implying $c_1 = 0$. For the inner flow the radius approaches zero requiring $d_2 = 0$. After establishing the disturbance potentials as solutions for Laplace's equation, the time dependence of the potentials is reincorporated. Writing the solutions using time dependent coefficients produces

$$\begin{aligned} \varphi_1 &= B_1(t) r^{-k} e^{ik\theta} \\ \varphi_2 &= B_2(t) r^{k} e^{ik\theta} \end{aligned} \tag{1.5}$$

The perturbation, η, is not a function of the radius and when expanded in Fourier modes takes on the form

$$\eta = A(t) e^{ik\theta} \tag{1.6}$$

At this point all the disturbance parameters have been rendered in their time dependent forms, and we reflect on the goal of this analysis. The modal solution for the perturbation provides time evolution information and leads toward stability considerations. To comment on the stability of the flow near the vortex sheet we need to solve for at least one of the time dependent coefficients $A(t)$, $B_1(t)$, or $B_2(t)$. Substituting the modal product solutions, (1.5) and (1.6), into (1.1) and rearranging the terms yields

$$\partial_t A = \tfrac{1}{2a} u_\theta ikA - kB_1 a^{-k-1} \tag{1.7}$$

and a similar substitution into (1.2) yields

$$\partial_t A = -\tfrac{1}{2a} u_\theta ikA + kB_2 a^{k-1} \tag{1.8}$$

These relations give the time rate of change for the perturbation magnitude and are summed momentarily. To build a relationship between the disturbance potentials, the next substitution inserts the modal solutions into (1.4) yielding

$$\partial_t B_1 a^{-k} - \partial_t B_2 a^{k} - \tfrac{u_\theta}{2a} ikB_1 a^{-k} - \tfrac{u_\theta}{2a} ikB_2 a^{k} = 0 \tag{1.9}$$

Pursuing the representation for $A(t)$, sum the time partials of (1.7) and (1.8) giving

$$2\partial_t^2 A = \tfrac{1}{2a} u_\theta ik\partial_t A - k\partial_t B_1 a^{-k-1} - \tfrac{1}{2a} u_\theta ik\partial_t A + k\partial_t B_2 a^{k-1}$$

Replacing the $\partial_t A$ terms in the above sum with (1.7) and (1.8) yields

$$(1.10)\qquad \begin{aligned} 2\partial_t^2 A &= \left(\tfrac{u_0 k}{2a}\right)^2 A + \tfrac{u_0}{2a} i k^2 B_2 a^{k-1} - k\partial_t B_1 a^{-k-1} + \\ &\left(\tfrac{u_0 k}{2a}\right)^2 A + \tfrac{u_0}{2a} i k^2 B_1 a^{-k-1} + k\partial_t B_2 a^{k-1} \end{aligned}$$

Now multiply ka^{-1} on both sides of (1.9) and add the result to (1.10) removing all the terms containing B_j's. The resulting second order ODE

$$\partial_t^2 A = \left(\tfrac{u_0 k}{2a}\right)^2 A$$

has solutions which are proportional to exponentials

$$A(t) \propto e^{\sigma t} \quad \leftarrow \quad \sigma = \pm \tfrac{u_0 k}{2a}$$

This result shows any non constant perturbation of an infinitesimally thin vortex sheet excites an instability. Using (1.7) and (1.8) we see the stability of the disturbance potentials matches the stability of the perturbation. In practice, since the vortex sheet at the shear layer is not infinitesimally thin and curvature cannot be ignored the instability arises only for flows of sufficient Reynolds number. Drazin & Reid [12] address the impacts of shear layer thickness and curvature on the initial flow instability. A nontrivial shear layer thickness directly affects the high Fourier modes. The stability of these modes is maintained through the viscous dissipation within the layer. The curvature impacts the low Fourier modes. A tight curvature negates the formation of low modes since the wavelength cannot fit along the length of the shear layer. A critical Reynolds number exists for a given set of flow parameters such that the flow is stable when the Reynolds number is below the critical value and unstable otherwise. After the onset of the instability, the flow equalizes forming an n vortex braid where n is the Fourier mode with the lowest critical Reynolds number. The homogeneous flow stability results in section 4 show the balance between curvature and shear layer thickness.

1.2 Problem Formulation

The mathematical model for Newtonian fluid flow has existed from more than 150 years. The equations of motion describing physical fluid flow for this fluid are: continuity (mass conservation), momentum conservation, and balance of energy. The complexity of these equations necessitates the application of relevant, simplifying

assumptions for the flow. The principal assumptions used for this work are: 2-dimentional flow in a closed cylindrical disk, incompressible/homogeneous fluid, low velocity flow, and Ekman forcing resulting from top and bottom friction. Other assumptions are discussed as they are applied throughout the derivations. Fluid continuity and momentum balance adequately model the flow field and provide a set of equations that may be analyzed or solved numerically. Since thermal excitation of the flow is not considered and buoyancy effects are neglected, the energy balance does not provide additional dynamic information. The time evolution of energy, enstrophy, and angular momentum is used to check the numerical accuracy of the simulation. Also, the circulation is enforced via incorporation into the no-slip boundary conditions.

1.2.1 Equations of motion

First consider the continuity equation. Continuity of a fluid is identical to considering the conservation of fluid mass, and fluid continuity is represented as

$$\frac{d\rho}{dt} + \rho\nabla\cdot\vec{u} = 0 \tag{1.11}$$

where ρ is the fluid density and $\vec{u} \equiv u_r\hat{e}_r + u_\theta\hat{e}_\theta + u_z\hat{e}_z$ is the fluid velocity. The continuity equation is transformed by the assumptions of fluid homogeneity, $\frac{d\rho}{dt} = 0$, and incompressibility, $\nabla\cdot\vec{u} = 0$. Once transformed, (1.11) simplifies to the incompressibility condition

$$\nabla\cdot\vec{u} = 0 \tag{1.12}$$

i.e. the velocity field is solenoidal. Note: the flow is assumed to take place in only 2-dimensions thus $u_z \equiv 0$ leaving $\vec{u} \equiv u_r\hat{e}_r + u_\theta\hat{e}_\theta = \langle u_r, u_\theta\rangle$.

The next equation under consideration is the most meaningful for this work. The momentum conservation equation (hereafter referred to as the Navier-Stokes equation) results from Newton's law of motion written for a fluid continuum

$$\frac{d\vec{u}}{dt} = -\frac{1}{\rho}\nabla p + \nabla\phi + \nu\nabla^2\vec{u} + \frac{\nu}{3}\nabla(\nabla\cdot\vec{u}) \tag{1.13}$$

where ν is the kinematic viscosity, $\nabla\phi$ are conservative body forces per unit density, and $\vec{u} = \langle u_r, u_\theta\rangle$ is the velocity written in vector notation. The 2D assumption neglects the possibility of recirculation in the vertical direction implying $\partial_z u_z \equiv 0$. Considering the terms on the right hand side of (1.13), the first term represents flow acceleration due

to a pressure gradient while the third term shows the velocity dissipation resulting from viscosity. The final term vanishes due to the incompressibility of the fluid.

Additional terms appear in the momentum balance when the reference frame is changed to a constant rotation in the plane of fluid flow. The frame change removes a rigid rotation from the flow and produces a relative velocity field

(1.14) $$\vec{u}_\Omega = \vec{u} - \vec{\Omega} \times \vec{r}$$

where $\vec{u}_\Omega$ is the velocity in the rotating frame, $\vec{u}$ is the velocity in the fixed frame, $\vec{\Omega} \equiv \Omega \hat{e}_z$ giving Ω as the constant angular velocity of the rotating frame, and $\vec{r} = r\hat{e}_r$ with r being the distance from the origin. The new frame adds two accelerations, Coriolis and centripetal, into the momentum balance. The Coriolis acceleration results from the gradient in the tangential velocity and has the form

(1.15) $$2\vec{\Omega} \times \vec{u}_\Omega = -2\Omega u_{\Omega,\theta}\hat{e}_r = \left(-2\Omega u_\theta + 2\Omega^2 r\right)\hat{e}_r$$

where $u_{\Omega,r}$ is the radial component of the velocity in the rotating frame. The centripetal acceleration acts normal to the tangential velocity as

(1.16) $$\vec{\Omega} \times \left(\vec{\Omega} \times \vec{r}\right) = -\Omega^2 r\hat{e}_r$$

The centripetal acceleration can be written as the gradient of a potential and included with the body force term. Using vector identity A.1 with $\vec{a} = \vec{b} = \vec{\Omega}$ and $\vec{c} = \vec{r}$

$$\vec{\Omega} \times \left(\vec{\Omega} \times \vec{r}\right) = \cancel{\left(\vec{\Omega} \cdot \vec{r}\right)}\vec{\Omega} - \Omega^2 \vec{r}$$

the centripetal acceleration equates to a gradient

(1.17) $$\vec{\Omega} \times \left(\vec{\Omega} \times \vec{r}\right) = -\nabla \phi_c$$

where the potential function, ϕ_c, is given by

(1.18) $$\phi_c = \tfrac{1}{2}\left|\vec{\Omega} \times \vec{r}\right|^2$$

The gradient is appropriate in this case since $\vec{\Omega}$ is constant implying $\partial_r \Omega = \partial_\theta \Omega = 0$. As a result the gradient of the centripetal potential gives

$$-\nabla \phi_c = -\nabla\left(\tfrac{1}{2}\left|\vec{\Omega} \times \vec{r}\right|\right) = \left(-\Omega^2 r - \Omega r^2 \cancel{\partial_r \Omega}\right)\hat{e}_r - \Omega r \cancel{\partial_\theta \Omega}\hat{e}_\theta = -\Omega^2 \vec{r}$$

This leaves the Coriolis acceleration which is discussed in more detail during the development of the vorticity form of the Navier-Stokes equation. Including the above

analysis into (1.13), assuming no body forces, and expanding the total derivative gives the familiar Navier-Stokes equation within a rotating frame

$$\partial_t \vec{u} + \vec{u}\cdot\nabla\vec{u} + 2\vec{\Omega}\times\vec{u} = -\tfrac{1}{\rho}\nabla p + \nu\nabla^2\vec{u} \tag{1.19}$$

At this point Ekman friction is added to the model and incorporated into the Navier-Stokes equation. To see how this is accomplished consider the velocity field in terms of a principal flow and a secondary flow residing within the Stewartson layers. The velocity field is represented as

$$\vec{u} = \vec{u}_L + \vec{u}'$$

where $\vec{u}_L$ is the 2-dimensional flow and $\vec{u}'$ is the small magnitude 3-dimensional flow resulting from Ekman friction and noise. Stewartson [30] revealed two layers of vertical transport at the shear layer of a differentially rotating fluid. These nested shear layers of thickness $E^{\frac{1}{4}}$ and $E^{\frac{1}{3}}$ are required to balance the mass transport of the Ekman layers which form at the upper and lower boundaries proportional to $E^{\frac{1}{2}}$.

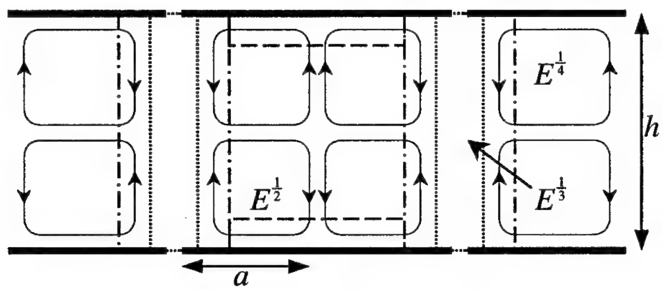

fig 1.3 Stewartson layers in the differentially rotating disk. h *is the height of the disk and* a *is the distance from the center of the disk to the shear layer.*

The resulting Ekman circulation, figure 1.3, occurs in the $E^{\frac{1}{4}}$ and $E^{\frac{1}{2}}$ layers. Niino & Misawa [23] establish the flow in the $E^{\frac{1}{3}}$ layer vanishes when averaged over the height of the disk. Consider the left hand side of equation (1.19) with the primary and small magnitude velocity

$$\tfrac{d}{dt}\left(\vec{u}_L + \vec{u}'\right) + \left(\vec{u}_L + \vec{u}'\right)\cdot\nabla\left(\vec{u}_L + \vec{u}'\right) = \tfrac{d\vec{u}_L}{dt} + \vec{u}_L\cdot\nabla\vec{u}_L + \vec{u}'\cdot\nabla\vec{u}' \tag{1.20}$$

The quadratic term, $\vec{u}'\cdot\nabla\vec{u}'$, contributes a momentum flux that is equivalent to a stress acting on the primary flow. This stress needs to be represented in terms of the primary velocity field in order to be included with the model. We assume the physical boundary of the disk is smooth contributing no noise, and the Ekman layer contributes a nontrivial vertical diffusion. The horizontal contribution from the Ekman layer is neglected since

its magnitude is small when compared with the primary 2-dimensional flow. The Navier-Stokes equation, (1.19), becomes

(1.21) $$\partial_t \vec{u} + \vec{u}\cdot\nabla\vec{u} + 2\vec{\Omega}\times\vec{u} = -\tfrac{1}{\rho}\nabla p + \nu\nabla^2\vec{u} + A_v\partial_z^2\vec{u}$$

The $A_v\partial_z^2\vec{u}$ term results from the vertical transport of the fluid due to the Ekman friction, Pedlosky [24]. Combining the 2-dimensional flow with the closed cylinder on top and bottom, we assume the velocity profile is parabolic in the azimuthal direction. Under this assumption the vertical diffusion is given within the plane of interest as a difference in velocity, $A_v\partial_z^2\vec{u} = \frac{8\nu}{h^2}\left(\vec{u}^* - \vec{u}\right)$. A complete discussion of this term is provided in section 1.2.2. Applying this representation for Ekman forcing into (1.21) yields the final 2D approximation of the Navier-Stokes equation in velocity form

(1.22) $$\partial_t \vec{u} + \vec{u}\cdot\nabla\vec{u} + 2\vec{\Omega}\times\vec{u} = -\tfrac{1}{\rho}\nabla p + \nu\nabla^2\vec{u} + \tfrac{8\nu}{h^2}\left(\vec{u}^* - \vec{u}\right)$$

where $\vec{u} = \langle u_r, u_\theta \rangle$ is the 2D velocity vector, ρ is the fluid density, p is the pressure, ν is the fluid viscosity, h is the height of the cylindrical disk, and $\vec{u}^*$ is the forcing vector.

With the continuity and Navier-Stokes equations available in velocity form as (1.12) and (1.22), respectively, we continue by converting the Navier-Stokes equation into the more useable vorticity-stream function form. To this end recall the definition of vorticity as

(1.23) $$\vec{\omega} \equiv \nabla\times\vec{u} = \omega\hat{e}_z$$

and the stream function is defined by its relationship to velocity

(1.24) $$\vec{u} = \nabla\psi\times\hat{e}_z$$

Using these definitions and the following identities, the velocity form of the Navier-Stokes equation is transformed to the vorticity-stream function form. Using vector identity A.2 let $\vec{a} = \vec{b} = \vec{u}$ yielding

$$\vec{u}\cdot\nabla\vec{u} = \tfrac{1}{2}\nabla\vec{u}^2 + \vec{\omega}\times\vec{u}$$

Using vector identity A.3 let $\vec{a} = \vec{u}$ yielding

$$\nabla^2\vec{u} = \nabla\cancel{\left(\nabla\cdot\vec{u}\right)} - \nabla\times\vec{\omega}$$

Begin the transition by substituting the above identities into (1.22) giving

(1.25) $$\partial_t \vec{u} + \left(\vec{\omega} + 2\vec{\Omega}\right)\times \vec{u} = -\tfrac{1}{\rho}\nabla p - \tfrac{1}{2}\nabla \vec{u}^2 - \nu\nabla\times\vec{\omega} + \tfrac{8\nu}{h^2}(\vec{u}^* - \vec{u})$$

In order to convert (1.25) entirely to vorticity and stream function, apply the curl operator to both sides of the equations. Applying the curl and using the definitions (1.23) and (1.24) gives

(1.26) $$\partial_t \vec{\omega} + \nabla\times\left(\left(\vec{\omega} + 2\vec{\Omega}\right)\times\left(\nabla\psi\times\hat{e}_z\right)\right) = -\nu\nabla\times\left(\nabla\times\vec{\omega}\right) + \tfrac{8\nu}{h^2}(\vec{\omega}^* - \vec{\omega})$$

Notice the gradient fields vanish under the curl. One must be careful since the pressure has been removed from the equations via a mathematical procedure. The physical existence of the pressure cannot be ignored. For our problem with a completely enclosed fluid any force due to pressure is balanced through an equal force at the boundary. However, analysis incorporating a free surface must adapt boundary conditions to resolve the pressure differential at the free surface. A detailed discussion of the pressure calculation is beyond the scope of this work. Continuing the derivation using vector identity A.3 with $\vec{a} = \nabla\times\vec{u} = \vec{\omega}$ yields

$$\nabla\times\left(\nabla\times\vec{\omega}\right) = \nabla\cancel{\left(\nabla\cdot\vec{\omega}\right)} - \nabla^2\vec{\omega}$$

while vector identity A.4 with $a = \omega$ and $\vec{b} = \nabla\psi$ yields

$$\nabla\times\left(\omega\nabla\psi\right) = \nabla\omega\times\nabla\psi + \omega\cancel{\left(\nabla\times\nabla\psi\right)}$$

Applying these identities to (1.25) gives

(1.27) $$\partial_t \vec{\omega} + \nabla\left(\vec{\omega} + 2\vec{\Omega}\right)\times\nabla\vec{\psi} = \nu\nabla^2\vec{\omega} + \tfrac{8\nu}{h^2}(\vec{\omega}^* - \vec{\omega})$$

Now the Coriolis acceleration is removed when considering the vorticity formulation because Ω is a constant implying $\nabla\Omega \equiv 0$. The final form of the Navier-Stokes equation in vorticity-stream function form

(1.28) $$\partial_t \vec{\omega} + J(\vec{\omega},\vec{\psi}) = \nu\nabla^2\vec{\omega} + \tfrac{8\nu}{h^2}(\vec{\omega}^* - \vec{\omega})$$

where ω is the magnitude of vorticity vector, ψ is the stream function, and $J(\vec{\omega},\vec{\psi})$ is the Jacobian, $J(\vec{\omega},\vec{\psi}) = \tfrac{1}{r}\left(\partial_r\vec{\omega}\partial_\theta\vec{\psi} - \partial_r\vec{\psi}\partial_\theta\vec{\omega}\right)$.

From the standpoint of numerical solvability, (1.28) gives a Helmholtz equation, and taking the curl of (1.24) produces a Poisson equation. These equations

(1.29) $$\partial_t \vec{\omega} - \nu\nabla^2\vec{\omega} = \tfrac{8\nu}{h^2}(\vec{\omega}^* - \vec{\omega}) - J(\vec{\omega},\vec{\psi})$$

(1.30) $$\nabla^2\vec{\psi} = -\vec{\omega}$$

constitute the vorticity-stream function formulation for this problem and are the mathematical model including all our assumptions. The method for solving the system (1.29)/(1.30) is discussed in section 2.

1.2.2 Ekman friction

The Ekman friction on the top and bottom of the disk induces vertical motion in the fluid through a phenomenon known as the Ekman spiral. This motion occurs within the Stewartson layers and shown in figure 1.3. The magnitude of the Ekman spiral velocity in the (r,θ) plane is small when compared to the primary rotation. Thus, the component of Ekman velocity in the plane is neglected while the vertical component is retained. To incorporate the fluid pump created by the Ekman friction, the Ekman number is defined

$$E = \frac{2\nu}{\Omega h^2}$$

where ν is the viscosity, Ω is the mean rotation of the system, and h is the height of the fluid in the disk. The vertical velocity induced by the Ekman pumping can be written in terms of the planar vorticity, and Früh [14] relates the vertical velocity to vorticity using

$$u_z = \frac{\sqrt{E}}{Ro}\left(\vec{\omega}^* - \vec{\omega}\right)$$

where $Ro = \frac{U}{2\Omega L}$ is the Rossby number, U is the horizontal velocity scale, and L is the Ekman layer thickness. The Ekman layer thickness is given as

$$L = E^{\frac{1}{4}}h$$

per the Stewartson layer thickness of vertical transport. Similarly, Pedlosky [24] solves the velocity diffusion equation finding

(1.31) $$A_v\partial_z^2\vec{u} = \frac{\sqrt{E}}{Ro}\left(\vec{u}^* - \vec{u}\right)$$

where $A_v = h^2E$ for a geometry with a closed boundary on all sides. Both Früh [14] and Pedlosky [24] performed asymptotic expansions on the flow in terms of the Rossby number. Combining these results shows the vertical velocity and vertical diffusion are related through the vorticity. Continuing with the Pedlosky approach, assume the fluid

has a parabolic profile for the velocity in the $\theta - z$ plane. The horizontal velocity scale is given by

$$U = \left(\frac{h^4\Omega}{64a^2\nu}\right)^{\frac{1}{2}}$$

Adapting the horizontal velocity scale into the Rossby number modifies the coefficient in (1.31) producing

$$\frac{\sqrt{E}}{Ro} = \frac{\frac{1}{h}\sqrt{\frac{\nu}{\Omega}}}{\frac{U}{2\Omega L}} = \frac{\frac{2L\sqrt{\nu\Omega}}{h}}{\frac{h^2}{8a}\sqrt{\frac{\Omega}{\nu}}} = \frac{16a\nu L}{h^3}$$

Our final assumption requires the disk height to be close in magnitude to the Ekman layer thickness. This condition minimizes the influence of the centrifugal and Coriolis forces on the instabilities. Thus entering $h \approx L$ and the normalized distance to the shear layer, $a = \frac{1}{2}$ gives the form of the Ekman pumping

$$A_v \partial_z^2 \vec{u} = \frac{\sqrt{E}}{Ro}\left(\vec{u}^* - \vec{u}\right) = \frac{8\nu}{h^2}\left(\vec{u}^* - \vec{u}\right)$$

This term represents the vertical fluid motion as a function of the planar velocity and matches our specific disk geometry.

1.2.3 Energy evolution

The equation for energy balance is not used to solve for vorticity or stream function, but rather to provides a verification tool for the numerical solution. Thermal considerations are not included with the energy evolution equation since no external thermal gradients are applied to the system and the buoyancy effects are neglected. Without the thermal components the energy equation shows a loss as viscous dissipation effects are converted to internal energy. The energy evolution equation is derived from the momentum balance. Consider (1.22) and dot the equation with $\vec{u}$. The result

$$\frac{1}{2}\partial_t\left(\vec{u}\cdot\vec{u}\right) + \vec{u}\cdot\left(\vec{u}\cdot\nabla\vec{u}\right) + \vec{u}\cdot\left(2\vec{\Omega}\times\vec{u}\right) = -\frac{1}{\rho}\vec{u}\cdot\nabla p + \nu\vec{u}\cdot\nabla^2\vec{u} + \frac{8\nu}{h^2}\vec{u}\cdot\left(\vec{u}^* - \vec{u}\right)$$

can be integrated over the circular domain of radius one. Note: since $\vec{u}$ lies in the planar domain and $\vec{\Omega}$ and $\vec{\varpi}$ are normal to the plane, the ensuing dot products are zero; $\vec{u}\cdot\vec{\Omega} = 0$, $\vec{u}\cdot\vec{\varpi} = 0$, $\vec{u}\cdot\left(\vec{\varpi}\times\vec{u}\right) = 0$, and $\vec{u}\cdot\left(\vec{\Omega}\times\vec{u}\right) = 0$. In order to simplify the energy balance, change to an integral form by multiplying by a differential area and integrating

$$(1.32)\qquad \begin{aligned}&\partial_t \iint \tfrac{1}{2}\vec{u}\cdot\vec{u}\,dS + \iint \vec{u}\cdot\left(\vec{u}\cdot\nabla\vec{u}\right)dS = \\ &\quad -\iint \tfrac{1}{\rho}\vec{u}\cdot\nabla p\,dS + \nu\iint \vec{u}\cdot\nabla^2\vec{u}\,dS + \tfrac{8\nu}{h^2}\iint \vec{u}\cdot\left(\vec{u}^* - \vec{u}\right)dS\end{aligned}$$

There is no potential energy with this geometry and the kinetic energy is

$$T = \iint \tfrac{1}{2}\vec{u}\cdot\vec{u}\,dS$$

Thus the time evolution of energy is $\frac{dT}{dt}$. To simplify (1.32) consider each term individually. The second term on the left hand side can be rewritten using vector identity A.2 letting $\vec{a} = \vec{b} = \vec{u}$ and then dotting $\vec{u}$ into both sides gives

$$\vec{u}\cdot\nabla\left(\vec{u}\cdot\vec{u}\right) = 2\vec{u}\cdot\left(\vec{u}\cdot\nabla\vec{u}\right) + 2\vec{u}\cdot\cancel{\left(\vec{u}\times\vec{\omega}\right)}$$

Using this result the second term is rewritten as

$$(1.33)\qquad \iint \vec{u}\cdot\left(\vec{u}\cdot\nabla\vec{u}\right)dS = \iint \tfrac{1}{2}\vec{u}\cdot\nabla\left(\vec{u}\cdot\vec{u}\right)dS$$

Continuing use vector identity A.5 with $a = \vec{u}\cdot\vec{u}$ and $\vec{b} = \vec{u}$ yielding

$$\nabla\cdot\left(\left(\vec{u}\cdot\vec{u}\right)\vec{u}\right) = \left(\vec{u}\cdot\vec{u}\right)\cancel{\left(\nabla\cdot\vec{u}\right)} + \vec{u}\cdot\nabla\left(\vec{u}\cdot\vec{u}\right)$$

Applying this result to (1.33) gives

$$(1.34)\qquad \iint \vec{u}\cdot\left(\vec{u}\cdot\nabla\vec{u}\right)dS = \iint \tfrac{1}{2}\nabla\cdot\left(\left(\vec{u}\cdot\vec{u}\right)\vec{u}\right)dS$$

To complete the final step for this term, apply the 2D case of the divergence theorem (Gauss' theorem) given here

$$\iint \nabla\cdot\vec{a}\,dS = \oint \vec{a}\cdot\vec{n}\,ds$$

and (1.34) becomes

$$(1.35)\qquad \iint \vec{u}\cdot\left(\vec{u}\cdot\nabla\vec{u}\right)dS = \oint \left(\vec{u}\cdot\vec{u}\right)\vec{u}\cdot\vec{n}\,ds$$

where $\vec{n}$ is the unit vector normal to the boundary of the fluid. Moving to the right hand side of (1.32), the first term can be rewritten using vector identity A.5. Let $a = p$ and $\vec{b} = \vec{u}$ yielding

$$\nabla\cdot\left(p\vec{u}\right) = p\cancel{\nabla\cdot\vec{u}} + \vec{u}\cdot\nabla p$$

and again apply Gauss' theorem to obtain

$$(1.36)\qquad \iint \tfrac{1}{\rho}\vec{u}\cdot\nabla p\,dS = \iint \tfrac{1}{\rho}\nabla\cdot\left(p\vec{u}\right)dS = \oint \tfrac{p}{\rho}\vec{u}\cdot\vec{n}\,ds$$

Since our simulation is conducted in a closed cylinder, the unit normal vector is everywhere normal to the surface of the cylinder. Also, the velocity normal to the surface is necessarily zero because there is no flux through the wall i.e. no fluid passes through the cylinder walls. Since velocity normal to the wall is zero, the dot product with the unit normal vector is also zero, $\vec{u}\cdot\vec{n}=0$. Hence, both terms (1.35) and (1.36) contribute nothing to the energy evolution. Rewriting the energy equation shows that the energy evolution results exclusively from the viscous effects

$$\frac{dT}{dt}=\nu\iint\vec{u}\cdot\nabla^2\vec{u}dS+\frac{8\nu}{h^2}\iint\vec{u}\cdot\left(\vec{u}^*-\vec{u}\right)dS \tag{1.37}$$

At this point the integrands are simplified, and the energy evolution is written for our specific numerical work. Using vector identity A.6, let $\vec{a}=\nabla$ and $\vec{b}=\vec{u}$ then dot the velocity into both sides of the identity for

$$\vec{u}\cdot\nabla^2\vec{u}-\vec{u}\cdot\nabla\left(\cancel{\nabla\cdot\vec{u}}\right)=-\vec{u}\cdot\left[\nabla\times\left(\nabla\times\vec{u}\right)\right]=-\vec{u}\cdot\left(\nabla\times\vec{\omega}\right)$$

Continuing use vector identity A.7 with $\vec{a}=\vec{u}$ and $\vec{b}=\vec{\omega}$ giving

$$-\vec{u}\cdot\left(\nabla\times\vec{\omega}\right)=\nabla\cdot\left(\vec{u}\times\vec{\omega}\right)-\vec{\omega}\cdot\left(\nabla\times\vec{\omega}\right)=\nabla\cdot\left(\vec{u}\times\vec{\omega}\right)-\vec{\omega}\cdot\vec{\omega}$$

Combining the above equations and employing Gauss' divergence theorem leads to

$$\iint\vec{u}\cdot\nabla^2\vec{u}dS=\iint\nabla\cdot\left(\vec{u}\times\vec{\omega}\right)dS-W=\oint\left(\vec{u}\times\vec{\omega}\right)\cdot\vec{n}ds-W \tag{1.38}$$

where $\vec{n}$ is the unit vector normal to the boundary and $W\equiv\iint\omega^2dS$ is the enstrophy.

Now the integrand of the line integral is rewritten

$$\left(\vec{u}\times\vec{\omega}\right)\cdot\vec{n}=\left(u_\theta\omega\hat{e}_r-u_r\omega\hat{e}_\theta\right)\cdot\hat{e}_r=u_\theta\omega$$

and is evaluated at the boundary. Incorporating (1.38) and expanding the second term on the right hand side of (1.37) produces an energy evolution with the form

$$\frac{dT}{dt}=\nu\int_0^{2\pi}u_\theta\omega\Big|_{r=1}d\theta-\nu W+\frac{8\nu}{h^2}\int_0^1\int_0^{2\pi}\vec{u}\cdot\vec{u}^*d\theta rdr-\frac{16\nu}{h^2}T \tag{1.39}$$

Here we note the energy evolution is a function of the enstrophy and the kinetic energy.

1.2.4 Enstrophy evolution

While not one of the equations of motion, the enstrophy evolution provides an important diagnostic test for the numerical simulation. The enstrophy is the mean square measure of vorticity, and its evolution can by calculated analytically. Beginning with the Navier-Stokes equation in vorticity form

$$\partial_t \omega = \nabla \times \left(\vec{u} \times \left(\vec{\omega} + 2\vec{\Omega}\right)\right) + \nu \nabla^2 \omega + \tfrac{8\nu}{h^2}(\omega^* - \omega)$$

multiply both sides by the vorticity giving

$$\tfrac{1}{2}\partial_t \omega^2 = \vec{\omega} \cdot \left[\nabla \times \left(\vec{u} \times \left(\vec{\omega} + 2\vec{\Omega}\right)\right)\right] + \nu \vec{\omega} \cdot \nabla^2 \omega + \tfrac{8\nu}{h^2} \vec{\omega} \cdot (\omega^* - \omega)$$

As with the energy evolution, integrate this equation over the unit circle giving

$$\begin{aligned}(1.40) \qquad \tfrac{1}{2}\iint \partial_t \omega^2 dS = \iint \vec{\omega} \cdot \left[\nabla \times \left(\vec{u} \times \left(\vec{\omega} + 2\vec{\Omega}\right)\right)\right] dS &+ \\ \nu \iint \vec{\omega} \cdot \nabla^2 \vec{\omega} dS + \tfrac{8\nu}{h^2} \iint \vec{\omega} \cdot (\vec{\omega}^* - \vec{\omega}) dS &\end{aligned}$$

Enstrophy is defined by $W = \iint \omega^2 dS$ so the right hand side of (1.40) already represents enstrophy evolution, $\frac{dW}{dt}$.

For the first step to simplify the terms in (1.40) recall the 2D assumption for the flow in the disk. The $\vec{\omega} + 2\vec{\Omega}$ vector is normal to the 2D surface of flow, $\vec{\omega} + 2\vec{\Omega} = (\omega + 2\Omega)\hat{e}_z$. As a result any dot product between the vorticity vector and a vector contained in the 2D flow equals zero e.g. $\vec{u} \cdot \left(\vec{\omega} + 2\vec{\Omega}\right) = 0$ and $\left(\vec{\omega} + 2\vec{\Omega}\right) \cdot \nabla = 0$. Using the 2D assumption and vector identity A.6 with $\vec{a} = \vec{u}$ and $\vec{b} = \vec{\omega} + 2\vec{\Omega}$ yields

$$\nabla \times \left(\vec{u} \times \vec{\omega} + 2\vec{\Omega}\right) = \cancel{\left(\vec{\omega} + 2\vec{\Omega}\right) \cdot \nabla} \vec{u} - \left(\vec{\omega} + 2\vec{\Omega}\right)\cancel{\left(\nabla \cdot \vec{u}\right)} - \vec{u} \cdot \nabla\left(\vec{\omega} + 2\vec{\Omega}\right) + \vec{u}\left(\cancel{\nabla \cdot \left(\vec{\omega} + 2\vec{\Omega}\right)}\right)$$

Multiplying by $\vec{\omega}$ and recalling $2\vec{\Omega}$ is a constant gives

$$\vec{\omega} \cdot \left[\nabla \times \left(\vec{u} \times \vec{\omega} + 2\vec{\Omega}\right)\right] = -\vec{\omega} \cdot \left(\vec{u} \cdot \nabla \vec{\omega}\right) + \vec{\omega} \cdot \vec{u} \cdot \cancel{\nabla 2\vec{\Omega}} = -\tfrac{\vec{u}}{2} \cdot \nabla \omega^2$$

This expression matches the integrand of the first term on the right hand side of (1.40). Rewriting the first term gives

$$(1.41) \qquad \iint \vec{\omega} \cdot \left[\nabla \times \left(\vec{u} \times \vec{\omega} + 2\vec{\Omega}\right)\right] dS = -\tfrac{1}{2}\iint \vec{u} \cdot \nabla \omega^2 dS$$

Next apply vector identity A.5 letting $a = \omega^2$ and $\vec{b} = \vec{u}$

$$\nabla\cdot\left(\omega^2\vec{u}\right)=\omega^2\cancel{\nabla\cdot\vec{u}}+\vec{u}\cdot\nabla\omega^2$$

and Gauss' theorem to (1.41) giving the now familiar form

$$\iint\vec{\omega}\cdot\left[\nabla\times\left(\vec{u}\times\vec{\omega}+2\vec{\Omega}\right)\right]dS=-\tfrac{1}{2}\iint\nabla\cdot\left(\omega^2\vec{u}\right)dS=-\tfrac{1}{2}\oint\omega^2\vec{u}\cdot\vec{n}ds \tag{1.42}$$

where $\vec{n}$ is the unit vector normal to the boundary. Again the velocity normal to the cylinder walls is zero negating any contribution from the above term.

As with the energy evolution, only the terms resulting from viscous interactions contribute to the enstrophy evolution. The resulting enstrophy evolution equation is

$$\tfrac{dW}{dt}=2\nu\iint\vec{\omega}\cdot\nabla^2\vec{\omega}dS+\tfrac{16\nu}{h^2}\iint\vec{\omega}\cdot\left(\vec{\omega}^*-\vec{\omega}\right)dS \tag{1.43}$$

Further adaptation of the enstrophy evolution begins by simplifying the first term on the right hand side of (1.43). This is accomplished by considering Green's theorem

$$\iint a\nabla^2 bdS=\oint a\nabla b\cdot\vec{n}-\iint\nabla a\cdot\nabla bdS$$

while allowing $a=b=\omega$. The first term is written as

$$\nu\iint\omega\nabla^2\omega dS=\nu\oint\omega\nabla\omega\cdot\vec{n}ds-\nu\iint\left(\nabla\omega\right)^2dS$$

where $\nabla\omega=\partial_r\omega\hat{e}_r+\frac{1}{r}\partial_\theta\omega\hat{e}_\theta$ in the 2D circular geometry of the disk. Applying this transformation and an expansion of the last term on the right hand side, equation (1.43) becomes

$$\tfrac{d\Omega}{dt}=2\nu\oint\omega\nabla\omega\cdot\vec{n}ds-2\nu\iint\left(\nabla\omega\right)^2dS+\tfrac{16\nu}{h^2}\iint\vec{\omega}\cdot\vec{\omega}^*dS-\tfrac{16\nu}{h^2}W \tag{1.44}$$

The evaluation of the integrals for our specific flow parameters begins with the representation of the integrands

$$\omega\nabla\omega\cdot\vec{n}=\omega\left(\partial_r\omega\hat{e}_r+\tfrac{1}{r}\partial_\theta\omega\hat{e}_\theta\right)\cdot\hat{e}_r\big|_{r=1}=-\omega\partial_r\omega\big|_{r=1}=-\tfrac{1}{2}\partial_r\omega^2$$

$$\vec{\omega}\cdot\vec{\omega}^*=\omega\hat{e}_z\cdot\omega^*\hat{e}_z=\omega\omega^*$$

The final form for (1.44) is

$$\tfrac{dW}{dt}=\pi\nu\partial_r\left(\omega^2\right)_0-2\nu\int_0^{2\pi}\int_0^1\left(\left(\partial_r\omega\right)^2+\left(\tfrac{1}{r}\partial_\theta\omega\right)^2\right)rdrd\theta+$$
$$\tfrac{16\nu}{h^2}\int_0^1\omega^*\left(\int_0^{2\pi}\omega d\theta\right)rdr-\tfrac{16\nu}{h^2}W$$

1.2.5 Angular momentum evolution

The angular momentum is another diagnostic tool used to check the accuracy of the spectral simulation. The following discussion is adapted from Coutsias & Lynov [8]. Using the given geometry we consider a 2D domain in polar coordinates and enclosed on all sides by a rigid boundary.

The scalar angular momentum is defined as

$$A \equiv \vec{A}\cdot\hat{e}_z = \iint \left(\vec{u}\times\vec{r}\right)\cdot\vec{n}dS$$

where $\vec{r}$ is in the plane and $\vec{n} = \hat{e}_z$. Combining (1.25) and the above definition we see the time evolution of angular momentum is

$$\tfrac{dA}{dt} = \iint \left(\partial_t\vec{u}\times\vec{r}\right)\cdot\hat{e}_z dS = \sum_{n=1}^{4} I_n$$

where the I_n terms are

(1.45) $$I_1 = \iint \left[\left(\vec{u}\times\vec{\omega}\right)\times\vec{r}\right]\cdot\hat{e}_z dS$$

(1.46) $$I_2 = -\iint \left[\nabla\left(\tfrac{1}{2}u^2 + p\right)\times\vec{r}\right]\cdot\hat{e}_z dS$$

(1.47) $$I_3 = -\nu\iint \left[\left(\nabla\times\vec{\omega}\right)\times\vec{r}\right]\cdot\hat{e}_z dS = \nu\iint \left(\nabla^2\vec{u}\times\vec{r}\right)\cdot\hat{e}_z dS$$

(1.48) $$I_4 = \tfrac{8\nu}{h^2}\iint \left[\left(\vec{u}^* - \vec{u}\right)\times\vec{r}\right]\cdot\hat{e}_z dS$$

Each I_n term is evaluated independently. For I_1 notice the combination of cross products gives

$$\left(\vec{u}\times\vec{\omega}\right)\times\vec{r} = \left(\vec{u}\cdot\vec{r}\right)\vec{\omega}$$

Substituting the above relation and the definitions for velocity and vorticity into (1.45) yields

(1.49) $$I_1 = \int_0^1\int_0^{2\pi} u_r r\left[\tfrac{1}{r}\left(\partial_r\left(ru_\theta\right) - \partial_\theta u_r\right)\right] rd\theta dr$$

The integrand is expanded to the form

(1.50) $$r^2 u_r\left[\tfrac{1}{r}\left(\partial_r\left(ru_\theta\right) - \partial_\theta u_r\right)\right] = r^2 u_r\partial_r u_\theta + ru_r u_\theta - ru_r\partial_\theta u_r$$

At this point recall the flow is divergence free. Expanding the divergence of the velocity while multiplying $r^2 u_\theta$ to both side of the equation gives

$$r^2 u_\theta (\nabla \cdot \vec{u}) = 0 = r u_\theta u_r + r^2 u_\theta \partial_r u_r + r u_\theta \partial_\theta u_\theta$$

Adding the zero divergence into (1.50) and rearranging the terms gives

$$r^2 u_r \left[\tfrac{1}{r}\left(\partial_r (r u_\theta) - \partial_\theta u_r\right)\right] = r^2 u_r \partial_r u_\theta + r^2 u_\theta \partial_r u_r + 2 r u_r u_\theta + r u_\theta \partial_\theta u_\theta - r u_r \partial_\theta u_r$$
$$= \partial_r \left(r^2 u_r u_\theta\right) + \partial_\theta \left(r u_\theta^2\right) - \tfrac{1}{2} \partial_\theta \left(r u_r^2\right)$$

Rewriting the integral (1.49) with the above partial derivatives yields

$$I_1 = \int_0^{2\pi} \int_0^1 \partial_r \left(r^2 u_r u_\theta\right) dr d\theta + \int_0^1 \int_0^{2\pi} \partial_\theta \left(r u_\theta^2\right) d\theta dr - \tfrac{1}{2} \int_0^1 \int_0^{2\pi} \partial_\theta \left(r u_r^2\right) d\theta dr$$

The integral evaluates to zero because $u_\theta\big|_{r=0} = 0$ and $u_r\big|_{r=1} = 0$, and the other two integrals evaluate to zero because the velocity is periodic in the θ component. For the second term apply the vector identity A.4 with $a = \tfrac{1}{2}u^2 + p$ and $\vec{b} = \vec{r}$ producing

$$I_2 = -\iint \left[\nabla\left(\tfrac{1}{2}u^2 + p\right) \times \vec{r}\right] \cdot \hat{e}_z dS$$
$$= -\iint \nabla \times \left(\tfrac{1}{2}u^2 + p\right)\vec{r} \cdot \hat{e}_z dS + \iint \left(\tfrac{1}{2}u^2 + p\right)\cancel{(\nabla \times \vec{r})} \cdot \hat{e}_z dS$$

Continue by applying Stokes' theorem

$$\iint (\nabla \times \vec{a}) \cdot \vec{n} dS = \oint \vec{a} \cdot \overline{ds}$$

and the second term equates to zero

$$I_2 = -\iint \left[\nabla \times \left(\tfrac{1}{2}u^2 + p\right)\vec{r}\right] \cdot \hat{e}_z dS = \oint \left(\tfrac{1}{2}u^2 + p\right)\vec{r} \cdot \overline{ds} = 0$$

since the radial vector is normal to the boundary, $\vec{r} \perp \overline{ds}$. Moving to the third term begin with vector identity A.3. Allowing $\vec{a} = \vec{u}$ while including the definition for vorticity gives

$$\nabla^2 \vec{u} = \nabla \cancel{(\nabla \cdot \vec{u})} - \nabla \times (\nabla \times \vec{u}) = -\nabla \times \vec{\omega}$$

Incorporating the curl of the vorticity and the above identity with (1.47) yields

$$I_3 = \nu \iint \left(\nabla^2 \vec{u} \times \vec{r}\right) \cdot \hat{e}_z dS = -\nu \iint r \partial_r \omega \hat{e}_z \cdot \hat{e}_z dS = -\nu \int_0^{2\pi} \int_0^1 r^2 \partial_r \omega dr d\theta$$

Evaluating the integral gives the following formula

$$I_3 = -2\pi \nu \omega_0 (1) + 4\pi \nu u_0 (1)$$

where ω_0 and u_0 are the zero Fourier mode terms for vorticity and velocity, respectively. The non-zero Fourier modes integrate to zero over the range $\theta : 0 \to 2\pi$. The final term

is expanded for the integral. We can reduce the integrand of (1.48) since both $\vec{r}$ and $\vec{u}$ reside in the plane giving

$$I_4 = \tfrac{8\nu}{h^2}\iint\left[\left(\vec{u}^* - \vec{u}\right)\times\vec{r}\right]\cdot\hat{e}_z dS = -\tfrac{8\nu}{h^2}\iint r\left(u_\theta^* - u_\theta\right)dS$$

Recall the forcing, u_θ^*, is independent of θ and velocity is written through the stream function

$$u_\theta = \partial_r \psi$$

Again due to periodicity in the azimuthal direction all the non-zero Fourier modes vanish. Evaluating the final integral gives

$$I_4 = -\tfrac{16\pi\nu}{h^2}\int_0^1 r^2\left[u_\theta^*(r) - \partial_r\psi_0(r)\right]dr$$

Combining all of the terms gives the angular momentum evolution as

$$\tfrac{dA}{dt} = -2\pi\nu\omega_0(1) + 4\pi\nu u_0(1) - \tfrac{16\pi\nu}{h^2}\int_0^1 r^2\left[u_\theta^*(r) - \partial_r\psi_0(r)\right]dr$$

Due to the viscosity the angular momentum is not a conserved quantity.

1.2.6 Circulation evolution

The circulation is the measure of the vorticity flux through a surface formed by a closed curve. Using Green's theorem the vorticity flux equates to the component of velocity tangent to the closed curve along the closed curve

$$C = \iint \omega dS = \oint \vec{u}\cdot\overrightarrow{dl}$$

For the no-slip boundary conditions the velocity at the wall is zero in all directions indicating the circulation is also zero. To fully investigate the circulation and its time evolution begin with the velocity-vorticity equation

$$\partial_t \omega = \nabla\times\left(\vec{u}\times\vec{\omega}\right) + \nu\nabla^2\omega + \tfrac{8\nu}{h^2}\left(\vec{\omega}^* - \vec{\omega}\right)$$

Integrating the vorticity equation over the unit circle immediately yields the circulation evolution

$$\tfrac{dC}{dt} = \iint \nabla\times\left(\vec{u}\times\vec{\omega}\right)\cdot\hat{e}_z dS + \nu\iint \nabla^2\omega dS + \tfrac{8\nu}{h^2}\iint\left(\vec{\omega}^* - \vec{\omega}\right)dS \qquad (1.51)$$

Employ Stokes' theorem

$$\iint\left(\nabla\times\vec{a}\right)\cdot\vec{n}dS = \oint \vec{a}\cdot\overrightarrow{ds}$$

with $\vec{a} = \vec{u}\times\vec{\omega}$ to rewrite the first term in (1.51) as

$$\iint \nabla\times(\vec{u}\times\vec{\omega})\cdot\hat{e}_z dS = \oint(\vec{u}\times\vec{\omega})\cdot\overrightarrow{dl}$$

This term vanishes for either the no-slip or free-slip boundary conditions since the fluid is contained in a rigid disk. With the no-slip boundary conditions, the velocity is identically zero implying the line integral is also zero. Since there is no flux through the boundary, the free-slip conditions give a boundary velocity that is tangent to the wall, $\vec{u}\big|_{r=1} = u_\theta\hat{e}_\theta$. Applying the curl between this velocity and the vorticity, $u_\theta\hat{e}_\theta\times\omega\hat{e}_z$, results in a vector directed along the r axis. Since $\overrightarrow{dl} = dl\hat{e}_\theta$, the dot product with the curl of the integrand and the differential length equals zero, $u_\theta\omega\hat{e}_r\cdot dl\hat{e}_\theta = 0$. Thus the term equates to zero for both sets of boundary conditions. Now apply the divergence theorem to the second term on the right hand side of (1.51) giving

$$\nu\iint\nabla^2\omega dS = \nu\iint\nabla\cdot\nabla\omega dS = \nu\oint\nabla\omega\cdot\vec{n}dl$$

Combining this new form with a rewrite of the last term on the right hand side of the circulation evolution results in the form

$$\tfrac{dC}{dt} = \nu\oint\nabla\omega\cdot\vec{n}dl + \tfrac{8\nu}{h^2}\iint\vec{\omega}^* dS - \tfrac{8\nu}{h^2}C \tag{1.52}$$

Similar to the enstrophy evolution, the time rate of change for circulation depends explicitly on the current value of the circulation. This effect results directly from the inclusion of Ekman friction. Before solving this ODE we consider a final transformation for the specific values of the integrals on the unit disk. For the first term on the right hand side of the circulation evolution

$$\nabla\omega\cdot\vec{n} = \left(\partial_r\omega\hat{e}_r + \tfrac{1}{r}\partial_\theta\omega\hat{e}_\theta\right)\cdot\left(-\hat{e}_r\right) = -\partial_r\,\omega\big|_{r=1}$$

For the second, the forcing, $\vec{\omega}^*$, is a function of r only and is independent of θ. Combining these ideas into (1.52) gives

$$\tfrac{dC}{dt} = -2\pi\nu\,\partial_r\omega_0\big|_{r=1} + \tfrac{16\pi\nu}{h^2}\int_0^1\vec{\omega}^* r dr - \tfrac{8\nu}{h^2}C \tag{1.53}$$

where ω_0 is the constant term from the Fourier series expansion of the vorticity. All the higher Fourier modes vanish as the integral for $\theta: 0\rightarrow 2\pi$ is evaluated. When Ekman friction is not considered with the Navier-Stokes equation, the circulation evolution is

zero. To maintain consistency the value of $\partial_r \omega_0|_{r=1}$ is set equal to zero in the numerical simulation. The ODE provided by (1.53) gives

$$C = e^{-\frac{8\nu}{h^2}t} + 2\pi\int_0^1 \bar{\omega}^* r dr$$

showing the circulation decays exponentially to a steady value consistent with the forcing.

1.2.7 Dimensional analysis and scaling

For ease of expanding the functions in terms of Chebyshev polynomials, the dimensionless radial variable is scaled to $[-1,1]$. The actual radial distance exists on the interval $0 \le r \le R$ so the dimensionless distance on $-1 \le \tilde{r} \le 1$ results from the scaling $\tilde{r} = \frac{r}{R}$. The angular variation is dimensionless and occurs on $[0, 2\pi]$. The full list of dimensionless parameters, shown with a ~, is given here

$$\tilde{r} = \frac{1}{R} r$$

$$\tilde{t} = \frac{\delta u \beta}{R^2} t$$

$$\tilde{\omega} = \frac{R^2}{\delta u \beta}\omega$$

$$\tilde{\psi} = \frac{1}{\delta u \beta}\psi$$

$$\tilde{e} = \frac{1}{R} e$$

$$\delta u \equiv a\delta\Omega$$

where δu is the differential tangential velocity, a is the radial distance to the shear layer, $\delta\Omega$ is the differential angular velocity, and β is the appropriate length scale for the Reynolds number. For consistency the Ekman forcing vorticity is made dimensionless via

(1.54) $$\tilde{\omega}^* = \frac{R^2}{\delta u \beta}\omega^*$$

to preserve the equality $\frac{8\nu}{e^2}\left(\omega^* - \omega\right) = \frac{\delta u \beta}{R^4}\frac{8\nu}{\tilde{e}^2}\left(\tilde{\omega}^* - \tilde{\omega}\right)$. After applying the dimensionless parameters to (1.28), the result

(1.55) $$\partial_{\tilde{t}}\tilde{\omega} + \tilde{J}(\tilde{\omega}, \tilde{\psi}) = \frac{\nu}{\delta u \beta}\left[\tilde{\nabla}^2\tilde{\omega} + \frac{8}{\tilde{e}^2}(\tilde{\omega}^* - \tilde{\omega})\right]$$

can be rewritten using the Reynolds number

(1.56) $$\partial_{\tilde{t}}\tilde{\omega} + \tilde{J}(\tilde{\omega},\tilde{\psi}) = \frac{1}{\text{Re}}\left[\tilde{\nabla}^2\tilde{\omega} + \frac{8}{\tilde{\varepsilon}^2}(\tilde{\omega}^* - \tilde{\omega})\right]$$

The Reynolds number takes on the standard form for fluid flow in a circular geometry where the Kelvin-Helmholtz instability is studied

(1.57) $$\text{Re} = \frac{a\delta\Omega\beta}{\nu}$$

Equation (1.30) maintains identical form after applying the dimensionless parameters

(1.58) $$\tilde{\nabla}^2\tilde{\psi} = -\tilde{\omega}$$

From this point on the ~ is dropped and all variables are understood to be dimensionless. The most important adjustment for future calculations occurs with the forcing, (1.54).

2 Numerics

2.1 Introduction

Spectral methods are employed for numerical simulation by expanding the variables of interest using complete sets of global, orthogonal functions. The global nature of spectral methods make them ideal for solving partial differential equations (PDEs) in simple geometries. Fornberg [13] discusses the advantages of expanding variables using global analytic functions: 1) errors typically decay at exponential rather than polynomial rates, 2) the dissipative and dispersive errors are virtually nonexistent, and 3) computational grids are typically courser allowing for faster computation and lower memory requirements. Some of these advantages are lost, however, when spectral methods are extended to complex domains, Gottlieb & Orzag [16].

Once an appropriate set of basis functions are selected, there are three main techniques used to determine the expansion coefficients: Galerkin methods, tau methods, and pseudospectral (collocation) methods. The Galerkin technique recombines the basis functions to form a new basis which automatically satisfies the boundary conditions. The tau technique selects the expansion coefficients that satisfy the boundary conditions while minimizing the residual. Our simulation uses the pseudospectral technique where the nonlinear terms are calculated at the grid points while spatial derivatives are computed in the spectral domain. Differential operators are transformed into well-conditioned integral operators with boundary conditions enforced as tau constraints on the expansion coefficients.

Here we solve the 2D Navier-Stokes equations in a circular geometry referred to as the "disk". The disk is modeled with a small height compared to its radius resulting in quasi 2-dimensional (Q2D) fluid motion. Equations describing the flow are given in section 1.2.1. The basis functions used for the disk are Fourier in the periodic, angular direction and Chebyshev in the bounded, radial direction. The Fourier and Chebyshev bases are selected due to the existence of fast transforms which are required to evaluate nonlinear terms in a collocation method. The computational grid for the domain is equally spaced in the azimuthal direction and uses Guass-Lobatto points in the radial direction. The spatial variables, vorticity and stream function, are represented by

Fourier-Chebyshev expansions, and the general expansion of these flow parameters has the form

(2.1) $$\xi(r,\theta)=\sum_{n=-\frac{N}{2}}^{\frac{N}{2}}\sum_{m=0}^{M}\xi_{nm}T_m(r)\mathrm{e}^{in\theta} \qquad -R\le r\le R \qquad 0\le\theta\le 2\pi$$

where ξ is either vorticity, ω, or stream function, ψ; (r,θ) is the radial and angular location in the disk, respectively; $T_m(r)$ is the m^{th} Chebyshev polynomial; ξ_{nm} is the Fourier-Chebyshev expansion coefficient; $\frac{N}{2}+1$ is the number of Fourier modes; and $M+1$ is the number of Chebyshev modes.

The Fourier modes of the flow parameters uncouple and the resulting system of uncoupled, time dependent ODEs is solved using a third order, stiffly-stable semi-implicit Backward Difference Formula (SBDF). This scheme uses an implicit formulation of the vorticity to solve the linear terms and an explicit formulation for the nonlinear terms

$$L\omega = J(\omega,\psi)+F$$

The SBDF scheme is implemented with the Chebyshev tau method producing a Helmholtz operator. Postconditioning of the solution provides a banded system, and when combined with the fast transforms, yields a numerical solution in $O(NM\log NM)$ operations, Torres & Coutsias [32].

Using polar coordinates on the disk produces a point singularity at the origin, and methods for treating the singularity have been investigated by several authors. For our implementation an r^2 multiplier is included with the vorticity building partial regularity into the flow field. A more elegant solution to the point singularity involves an orthogonal basis behaving as $O(r^m)$ as $r\to 0$. This method is treated by Matsushima & Marcus [22] but lacks the fast transform required for numerical simulation. Several boundary condition solutions are offered to treat the singularity, and these can be found in Torres & Coutsias [32] and the included references.

The code written in Fortran 90 is paralleled using the Message Passage Interface (MPI) parallel language. The computational limitations arise due to the Fast Fourier Transform (FFT). During the transposition of the matrices used in the calculations,

information is passed between paralleled machines limiting computational speed to the computer interface hardware. A table showing the computational efficiency of the code can be found in Torres & Coutsias [32].

2.2 Fourier-Chebyshev expansion

Using a spectral scheme within the disk geometry lends itself to the Fourier-Chebyshev expansion of the stream function and vorticity. The Fourier expansion in the azimuthal direction, θ, matches the natural periodicity resulting from polar coordinates. The Chebyshev expansion in the radial direction, r, allows for efficient postconditioning of the problem and fast transformations between point space and mode space. The resulting expansions for stream function and vorticity follow from (2.1) and are given here considering a trigonometric Fourier basis

$$\psi(r,\theta)=\sum_{n=0}^{\frac{N}{2}}\sum_{m=0}^{M}\psi_{nm}^{c}T_m(r)\cos n\theta+\psi_{nm}^{s}T_m(r)\sin n\theta \tag{2.2}$$

$$\omega(r,\theta)=\sum_{n=0}^{\frac{N}{2}}\sum_{m=0}^{M}\omega_{nm}^{c}T_m(r)\cos n\theta+\omega_{nm}^{s}T_m(r)\sin n\theta \tag{2.3}$$

where ψ_{nm}^{c}, ω_{nm}^{c}, ψ_{nm}^{s}, and ω_{nm}^{s} are the cosine and sine coefficients for the stream function and vorticity, respectively, $-R\le r\le R$, and $0\le\theta\le 2\pi$. Both Fourier and Chebyshev bases are orthogonal and possess the Fast Fourier Transform and Fast Cosine Transforms (FFT/FCT), respectively. The fast transforms offer $O(NM\log NM)$ operations to move between point space and mode space making them ideal for numerical simulation. Once the problem is transformed to mode space the nonlinear terms are represented by convolutions. The number of computations required to resolve the convolutions increases quadratically with the number of modes, $(NM)^2$, destroying the $NM\log NM$ pace of the computations. Therefore, the FFT/FCT are required for calculating the nonlinear terms by transforming them into point space where they are multiplied directly in NM computations.

The grid applied to the computational domain expands the 2π radians equally and the individual grid points are

$\theta_k=\frac{k2\pi}{N}$ for $0\le k\le N$

The radial Chebyshev polynomials are expanded on $-R \le r \le R$ instead of $0 \le R$ using the Gauss-Lobatto quadrature points

$$r_k = R\cos\left(\frac{k\pi}{M}\right) \text{ for } 0 \le k \le M$$

This choice of grid improves the condition numbers for the spectral matrices, Torres & Coutsias [32]. It must be noted that an expansion of $0 \le \theta \le 2\pi$ and $-R \le r \le R$ produces a grid that covers the disk twice. The solution on $0 \le \theta \le \pi$, $r: R \to -R$ matches exactly with the solution on $\pi \le \theta \le 2\pi$, $r: -R \to R$. Since the Fourier modes are uncoupled, an important result of this double coverage appears in the spectral matrices. Consider a function on the disk

$$A(r,\theta) = f(r)\cos n\theta$$

where $f(r)$ is expanded in Chebyshev polynomials. Since the gird on the disk overlaps itself exactly, the correlation of grid points gives the following equivalence

$$A(r,\theta) = f(r)\cos n\theta = f(-r)\cos(\theta+\pi)n = A(-r,\theta+\pi)$$

Continuing $f(-r)\cos(\theta+\pi)n = f(-r)\cos n\theta(-1)^n$ implies

$$f(r) = (-1)^n f(-r)$$

and the terms in the Chebyshev expansions have the same even/odd parity as the Fourier mode number, n. Furthermore, $f(r)\sin n\theta$ yields an identical parity. The vorticity and stream function are represented by a matrix containing the Fourier-Chebyshev coefficients. The Chebyshev polynomials are identified by the rows in order $0 \to M$, and the Fourier trigonometric functions appear as columns paired cosine/sine for modes $0 \to \frac{N}{2}$. The parity existing between the Chebyshev and Fourier mode numbers implies half of the coefficient matrix is always zero, and the form of the matrix is given here

$$\begin{bmatrix} * & 0 & 0 & 0 & * & * & \cdots & \cdots & * & * \\ 0 & 0 & * & * & 0 & 0 & \cdots & \cdots & 0 & 0 \\ * & 0 & 0 & 0 & * & * & \cdots & \cdots & * & * \\ 0 & 0 & * & * & 0 & 0 & \cdots & \cdots & 0 & 0 \\ * & 0 & 0 & 0 & * & * & \cdots & \cdots & * & * \\ 0 & 0 & * & * & 0 & 0 & \cdots & \cdots & 0 & 0 \\ \vdots & \vdots & \vdots & \vdots & \vdots & \vdots & & & \vdots & \vdots \\ * & 0 & 0 & 0 & * & * & \cdots & \cdots & * & * \end{bmatrix}$$

where * represents a nonzero coefficient. This guaranteed structure for the vorticity and stream function matrices allows a significant reduction in the number of computations since the nontrivial information can be packed into a matrix of only half size.

2.3 Spatial differentiation in the spectral scheme

Herein lies the power behind spectral methods. The system of equations to be solved is dominated by radial derivatives. The Chebyshev polynomials are differentiated exactly so that the differentiation error derives from truncation of the expansion. Due to the convergence of the Chebyshev expansion, the error inherent in the Chebyshev expansion decreases exponentially as more polynomials are retained. Since the same is true of the Fourier expansion, computation of spatial derivatives is exponentially accurate when integration conditioning is used. Two spectral matrices are constructed representing linear multiplication and differentiation operators within the Chebyshev basis, see appendix D. The linear multiplication matrix, $\mathbf{R}$, and differentiation matrix, $\mathbf{D}$, apply to a column vector consisting of Chebyshev coefficients.

To address the full problem, the coefficient matrix for vorticity is rewritten as a single column vector. Each column in the vorticity matrix contains the Chebyshev expansion coefficients for a specific Fourier mode. These columns are stacked on top of one another to form the following vectors for vorticity

$$\bar{\omega}(r,\theta)=\begin{bmatrix}\bar{\omega}_0^c(r)\\ \bar{\omega}_1^c(r)\\ \vdots\\ \bar{\omega}_{\frac{N}{2}}^c(r)\\ 0\\ \bar{\omega}_1^s(r)\\ \vdots\\ \bar{\omega}_{\frac{N}{2}}^s(r)\end{bmatrix} \quad \text{and for stream function: } \bar{\psi}(r,\theta)=\begin{bmatrix}\bar{\psi}_0^c(r)\\ \bar{\psi}_1^c(r)\\ \vdots\\ \bar{\psi}_{\frac{N}{2}}^c(r)\\ 0\\ \bar{\psi}_1^s(r)\\ \vdots\\ \bar{\psi}_{\frac{N}{2}}^s(r)\end{bmatrix}$$

where $\bar{\omega}_j^c(r)$ and $\bar{\omega}_j^s(r)$ are the vorticity Chebyshev coefficient vectors for the j^{th} Fourier mode cosine and sine, respectively, and similarly $\bar{\psi}_j^c(r)$ and $\bar{\psi}_j^s(r)$ are the stream function Chebyshev coefficient vectors. This formulation of the problem is hereafter referred to as the full vector form. Since multiplication and differentiation by r

impact only the Chebyshev coefficients, the matrices providing multiplication and differentiation by r for the full vector problem are

$$\hat{\mathbf{R}} = \mathbf{I}_{\frac{N}{2}+1} \otimes \mathbf{R}$$

$$\hat{\mathbf{D}} = \mathbf{I}_{\frac{N}{2}+1} \otimes \mathbf{D}$$

where $\mathbf{I}_{\frac{N}{2}+1}$ is the $\left(\frac{N}{2}+1\right)\times\left(\frac{N}{2}+1\right)$ identity matrix. In addition to these basic operations within the Fourier-Chebyshev expansion, $\hat{\mathbf{R}} \equiv r$ and $\hat{\mathbf{D}} \equiv \partial_r$, Fourier modes require differentiation by θ. In the full vector environment a new matrix is defined for this purpose, $\hat{\mathbf{Q}} \equiv \partial_\theta$. The $\hat{\mathbf{Q}}$ matrix is formed by considering the differentiation of sine and cosine functions. Here the impact is strictly upon the Fourier modes leaving the Chebyshev expansions unchanged. For differentiation by θ

$$\hat{\mathbf{Q}} = \begin{bmatrix} 0 & \mathbf{I}_{\frac{N}{2}+1} \otimes -n^2 \mathbf{I}_{M+1} \\ \mathbf{I}_{\frac{N}{2}+1} \otimes -n^2 \mathbf{I}_{M+1} & 0 \end{bmatrix}$$

where $n-1$ changes as the row of $\mathbf{I}_{\frac{N}{2}+1}$. The complete derivations of $\hat{\mathbf{R}}$, $\hat{\mathbf{D}}$, and $\hat{\mathbf{Q}}$ are presented in appendix D. For the numerical simulation, differentiation by θ only appears as a second partial, ∂_θ^2. The matrix form of this second partial derivative, $\hat{\mathbf{Q}}^2$. is given by

$$\hat{\mathbf{Q}}^2 = \mathbf{I}_{N+2} \otimes -n^2 \mathbf{I}_{M+1}$$

The block diagonal form of $\hat{\mathbf{R}}$, $\hat{\mathbf{D}}$, and $\hat{\mathbf{Q}}^2$ allows uncoupling of the Poisson and Helmholtz equations into the Chebyshev polynomials. Consider the Poisson equation

$$\left(\partial_r^2 + \tfrac{1}{r}\partial_r + \tfrac{1}{r^2}\partial_\theta^2\right)\psi = -\omega$$

and multiply by r^2 to remove the polar singularity. Rewriting in matrix representation gives

$$\text{(2.4)} \qquad \left(\hat{\mathbf{R}}^2\hat{\mathbf{D}}^2 + \hat{\mathbf{R}}\hat{\mathbf{D}} + \hat{\mathbf{Q}}^2\right)\varpi\!\!\!\!\psi = -\hat{\mathbf{R}}^2\varpi$$

Similarly the Helmholtz equation

$$\partial_t\omega - \nu\left(\partial_r^2 + \tfrac{1}{r}\partial_r + \tfrac{1}{r^2}\partial_\theta^2\right)\omega = -\tfrac{1}{r}\left(\partial_r\omega\partial_\theta\psi - \partial_r\psi\partial_\theta\omega\right) + \tfrac{8\nu}{e^2}\left(\omega^* - \omega\right)$$

multiplied by r^2 and writing in matrix form gives

$$\hat{\mathbf{R}}^2\partial_t\bar{\omega} - \nu\left(\hat{\mathbf{R}}^2\hat{\mathbf{D}}^2 + \hat{\mathbf{R}}\hat{\mathbf{D}} + \hat{\mathbf{Q}}^2 - \tfrac{8}{e^2}\hat{\mathbf{R}}^2\right)\bar{\omega} = \hat{\mathbf{R}}\left(\hat{\mathbf{R}}\bar{\psi} * \hat{\mathbf{Q}}\bar{\omega} - \hat{\mathbf{R}}\bar{\omega} * \hat{\mathbf{Q}}\bar{\psi}\right) - \tfrac{8\nu}{e^2}\hat{\mathbf{R}}^2\bar{\omega}^* \tag{2.5}$$

The nonlinear terms, $\hat{\mathbf{R}}\bar{\psi} * \hat{\mathbf{Q}}\bar{\omega}$ and $\hat{\mathbf{R}}\bar{\omega} * \hat{\mathbf{Q}}\bar{\psi}$, are determined in point space with the results transformed into a modal matrix via the FFT/FCT. Both (2.4) and (2.5) are uncoupled and for each Fourier mode n the system of equations has the form

$$\left(\mathbf{R}^2\mathbf{D}^2 + \mathbf{R}\mathbf{D} - n^2\mathbf{I}\right)\bar{\psi}_n = -\mathbf{R}^2\bar{\omega}_n \tag{2.6}$$

$$\mathbf{R}^2\partial_t\bar{\omega}_n - \nu\left(\mathbf{R}^2\mathbf{D}^2 + \mathbf{R}\mathbf{D} - n^2\mathbf{I} - \tfrac{8}{e^2}\mathbf{R}^2\right)\bar{\omega}_n = \mathbf{R}^2 J_n(\bar{\omega},\bar{\psi}) - \tfrac{8\nu}{e^2}\mathbf{R}^2\bar{\omega}_n^* \tag{2.7}$$

where $\bar{\psi}_n$ and $\bar{\omega}_n$ are vectors containing Chebyshev coefficients for Fourier mode n, $J_n(\bar{\omega},\bar{\psi})$ is the Jacobian previously computed in point space, and the forcing $\bar{\omega}_n^* = 0$ for $n > 0$. Fast computations are obtained for the Poisson equation, (2.6), since $\mathbf{R}$ is tridiagonal and $\mathbf{D}$ is postconditioned by $\mathbf{P}$ resulting in a banded system. The Helmholtz equation (2.7) is formed using the SBDF method described in section 2.5.5.

2.4 Postconditioning

The spectral matrices resulting from the Chebyshev basis provide a problem poorly conditioned for numerical computation. The entries in the $\mathbf{D}^2$ matrix grow with the Chebyshev mode number at the rate m^2. A postconditioner (or alternatively a preconditioner) not only improves the conditioning of the problem but produces a banded system of equations by transferring the differentiation operator into an equivalent integral operator, Torres & Coutsias [32]. The postconditioner, $\mathbf{P}$, is based upon the pseudo inverse of $\mathbf{D}$ such that the matrix product $\mathbf{DP}$ yields the identity matrix whose rows have been shifted up by one

$$\mathbf{DP} = \begin{bmatrix} 0 & 1 & 0 & \cdots & 0 \\ 0 & 0 & 1 & \ddots & \vdots \\ \vdots & \vdots & \ddots & \ddots & 0 \\ 0 & 0 & \cdots & 0 & 1 \\ 0 & 0 & \cdots & 0 & 0 \end{bmatrix}$$

Similarly $\mathbf{D}^2\mathbf{P}^2$ gives the identity with the rows shifted up by two. The stream function is modified with the postconditioner

$$\bar{\psi}_n = \mathbf{P}^2 \bar{\psi}_n^\circ$$

which is efficiently implemented in practice since $\mathbf{P}^2$ is pentadiagonal. Consider (2.6) with the postconditioner applied to the stream function

$$\left(\mathbf{R}^2\mathbf{I}_{[2]} + \mathbf{R}\mathbf{I}_{[1]}\mathbf{P} - n^2\mathbf{P}^2\right)\bar{\psi}_n^\circ = -\mathbf{R}^2\bar{\omega}_n \tag{2.8}$$

where $\mathbf{I}_{[j]}$ is the identity matrix shift up j rows. Boundary conditions are the final consideration required to solve (2.8). The τ conditions are implemented by shifting all of the matrix entries down two rows and inserting the boundary conditions as the first two rows. The equation augmented with boundary conditions produces $\bar{\psi}_n^\circ$ which is easily converted back to $\bar{\psi}_n$ through multiplication by the banded matrix, $\mathbf{P}^2$.

For the Helmholtz equation the spectral accuracy of the postconditioned method solution degrades as more Fourier modes are included. Alleviating the degradation is accomplished by smoothing the vorticity during postconditioning. Equation (2.7) is treated separately for $n=0$, $n=1$, and $n \geq 2$. Each case is treated with a different postconditioning of the vorticity aimed at smoothing the functions near the singularity. For the case $n=0$, transformation of the vorticity by a radial multiplier and postconditioner gives $\partial_r \bar{\omega}_0 = \mathbf{R}\mathbf{P}^2\bar{\omega}_0^\circ$. Similarly for the cases where $n=1$ and $n \geq 2$ the postconditioning comes in the forms $\bar{\omega}_1 = \mathbf{R}\mathbf{P}^2\bar{\omega}_1^\circ$ and $\bar{\omega}_n = \mathbf{R}^2\mathbf{P}^2\bar{\omega}_n^\circ$, respectively. Applying the radial multiplier, $\mathbf{R}$ or $\mathbf{R}^2$, builds partial regularity into the solution, but the multiplication is valid since each Fourier mode, n, decays like r^n as $r \to 0$. Smoothing the function successfully provides degradation abatement and is fully analyzed in Torres & Coutsias [32]. Applying the most frequent case, $n \geq 2$, of the postconditioning to the Helmholtz equation giving

$$\begin{aligned}&\mathbf{R}^4\mathbf{P}^2\partial_t\bar{\omega}_n^\circ - \nu\left(\mathbf{R}^2\mathbf{D}^2\mathbf{R}^2\mathbf{P}^2 + \mathbf{R}\mathbf{D}\mathbf{R}^2\mathbf{P}^2 - n^2\mathbf{R}^2\mathbf{P}^2 + \tfrac{8}{e^2}\mathbf{R}^4\mathbf{P}^2\right)\bar{\omega}_n^\circ = \\ &\quad \mathbf{R}^2 J_n(\bar{\omega},\bar{\psi}) - \tfrac{8\nu}{e^2}\mathbf{R}^2\bar{\omega}_n^*\end{aligned}$$

This equation simplifies through the relationship $\mathbf{D}\mathbf{R} = \mathbf{R}\mathbf{D} + \mathbf{I}$. After simplifying and removing the common terms we have

$$\mathbf{R}^2\mathbf{P}^2\partial_t\bar{\omega}_n^\circ - \nu\left[\mathbf{R}^2\mathbf{I}_{[2]} + 5\mathbf{R}\mathbf{I}_{[1]}\mathbf{P} + \left(4-n^2\right)\mathbf{P}^2 + \tfrac{8}{e^2}\mathbf{I}\right]\bar{\omega}_n^\circ = J_n(\bar{\omega},\bar{\psi}) - \tfrac{8\nu}{e^2}\bar{\omega}_n^* \tag{2.9}$$

The time differentiation is expanded via the SBDF giving an equation for the postconditioned vorticity at the next time level, $\vec{\omega}_n^{\circ,k+1}$. As with the Poisson equation, the entries in the matrices are shifted down two rows and the boundary conditions are inserted at the top. After calculating $\vec{\omega}_n^{\circ,k+1}$ the vorticity is quickly reclaimed through the multiplication by banded matrices, $\vec{\omega}_n^{k+1} = \mathbf{R}^2\mathbf{P}^2\vec{\omega}_n^{\circ,k+1}$. Fourier modes 0 and 1 follow a similar development but require special treatment. Fourier mode 1 takes the transformation $\vec{\omega}_1^{k+1} = \mathbf{R}\mathbf{P}^2\vec{\omega}_1^{\circ,k+1}$ while zero Fourier mode is $\partial_r\vec{\omega}_0^{k+1} = \mathbf{R}\mathbf{P}^2\vec{\omega}_0^{\circ,k+1}$.

2.5 Computational algorithm

This section outlines the primary steps taken in the code and the order in which they occur. As a summary tool, each step identifies subsections relating to that step.

1) The random noise is generated at the grid points see **2.5.1**
2) The forcing of the shear layer combines with the random noise to make the initial field see **2.5.2**
3) The initial field is projected onto the vorticity solvability constraints with a high order adjustment see **2.5.3**
4) The vorticity is transferred to the start-up subroutine
5) The equations are solved in the start-up routine as explained in steps 6) – 10). Vorticity and the Jacobian are transferred back to the main code see **2.5.4**
6) The current vorticity drives the Poisson equation which is solved for the stream function see **2.5.3** and **2.5.5**
7) The nonlinear terms appearing in the Jacobian are determined using the current stream function and vorticity
8) The forcing and Jacobian are combined to form the explicit portion of the SBDF see **2.5.2**
9) The Helmholtz equation is formed by applying the SBDF scheme to the vorticity and the explicit terms found in step 8) see **2.5.3** and **2.5.5**
10) The Helmholtz equation is solved for the new vorticity
11) The diagnostics are occasionally invoked and the relative errors of energy, enstrophy, and angular momentum evolution are calculated see **2.5.6**

12) steps 6) – 11) are repeated for a specified number of iterations

2.5.1 Initial conditions

The initial conditions used for these computations are double periodic without circulation. Due to the difficulty of producing a random field on a non uniform grid, the random initial conditions are established on a square where the grid points forming the square are equally spaced in both directions. The periodicity of the initial data is enforced in each direction on the grid by considering a random walk on the unit circle as

$$x_{j,\pi} \equiv 2\pi q$$

$$y_{j,\pi} \equiv 2\pi q$$

where q is a uniformly random number between 0 and 1 selected separately for each $x_{j,\pi}$ and $y_{j,\pi}$, respectively. The noise enters as perturbations to the Fourier modes. The square grid consists of four point clusters that ensure dual periodicity

$$\begin{matrix} \cos x_{i,\pi} \cos y_{j,\pi} & \sin x_{i,\pi} \cos y_{j+1,\pi} \\ \cos x_{i+1,\pi} \sin y_{j,\pi} & \sin x_{i+1,\pi} \sin y_{j+1,\pi} \end{matrix}$$

where the value at every point is weighted with a decaying Gaussian. The final form for the initial noise on the square grid is

$$\begin{matrix}
\Lambda_0^x\Lambda_0^y & \Upsilon_0^x\Lambda_1^y & \Lambda_0^x\Lambda_2^y & \Upsilon_0^x\Lambda_3^y & \cdots & \Lambda_0^x\Lambda_{P-1}^y & \Upsilon_0^x\Lambda_P^y \\
\Lambda_1^x\Upsilon_0^y & \Upsilon_1^x\Upsilon_1^y & \Lambda_1^x\Upsilon_2^y & \Upsilon_1^x\Upsilon_3^y & & \Lambda_1^x\Upsilon_{P-1}^y & \Upsilon_1^x\Upsilon_P^y \\
\Lambda_2^x\Lambda_0^y & \Upsilon_2^x\Lambda_1^y & \Lambda_2^x\Lambda_2^y & \Upsilon_2^x\Lambda_3^y & \cdots & \Lambda_2^x\Lambda_{P-1}^y & \Upsilon_2^x\Lambda_P^y \\
\Lambda_3^x\Upsilon_0^y & \Upsilon_3^x\Upsilon_1^y & \Lambda_3^x\Upsilon_2^y & \Upsilon_3^x\Upsilon_3^y & & \Lambda_3^x\Upsilon_{P-1}^y & \Upsilon_3^x\Upsilon_P^y \\
\vdots & & \vdots & & & \vdots & \\
\Lambda_{P-1}^x\Lambda_0^y & \Upsilon_{P-1}^x\Lambda_1^y & \Lambda_{P-1}^x\Lambda_2^y & \Upsilon_{P-1}^x\Lambda_3^y & \cdots & \Lambda_{P-1}^x\Lambda_{P-1}^y & \Upsilon_{P-1}^x\Lambda_P^y \\
\Lambda_P^x\Upsilon_0^y & \Upsilon_P^x\Upsilon_1^y & \Lambda_P^x\Upsilon_2^y & \Upsilon_P^x\Upsilon_3^y & & \Lambda_P^x\Upsilon_{P-1}^y & \Upsilon_P^x\Upsilon_P^y
\end{matrix}$$

where $\Lambda_j^x \equiv w_x^j \cos x_{j,\pi}$, $\Lambda_j^y \equiv w_y^j \cos y_{j,\pi}$, $\Upsilon_j^x \equiv w_x^j \sin x_{j,\pi}$, and $\Upsilon_j^y \equiv w_y^j \sin y_{j,\pi}$ with $w_x^j = \mathrm{e}^{-j^2}$ and $w_y^j = \mathrm{e}^{-j^2}$ being the appropriate Gaussian weighting at each location. After the random data are formed on the square, the data are interpolated onto the computational grid. The resulting interpolation provides an initial disturbance without bias from the non uniform grid spacing.

2.5.2 Forcing of the flow

The force transmitted to the fluid through the Ekman pumping acts as rigid body rotation near the center of the disk while vanishing at the outer wall. A tangent hyperbolic function models the radial velocity profile giving an infinitely differentiable flow near the shear layer. The forcing is uniform in the azimuthal direction. This forcing imparts a velocity only in the angular direction

$$\vec{u}^* = u_\theta = \tfrac{\Delta\Omega}{2a} r\left(1 + \tanh\tfrac{a-|r|}{\Delta r}\right)$$

A plot of the velocity versus radius for any angle shows the transition of the velocity at the shear layer, see figure 2.1. Since the code solves the Navier-Stokes equations in vorticity-stream function form, the forcing is entered as a vorticity

$$\vec{\omega}^* = \tfrac{\Delta\Omega}{a}\left[1 + \tanh\tfrac{a-|r|}{\Delta r} - \tfrac{|r|}{2\Delta r}\operatorname{sech}^2\tfrac{a-|r|}{\Delta r}\right]$$

A plot of the vorticity at the shear layer is shown in figure 2.2. With the no-slip boundary conditions, the initial vorticity is projected into the solution space. A random vorticity field does not necessarily conform to the solvability constraints imposed on the vorticity by the no-slip conditions. The projection is accomplished by adding a radial power function to each Fourier mode in the vorticity expansion

$$\omega_n^*(r) = \omega_n^*(r) + \eta_n r^p$$

where p matches the parity of the Fourier mode, n, and is selected as a large number. The coefficient is defined by

$$\eta_n = \frac{\vec{b}_n \cdot \mathbf{R}^2 \vec{\omega}_n}{\vec{b}_n \cdot \mathbf{R}^2 \overline{r^p}}$$

where $\overline{r^p}$ is the Chebyshev expansion vector for r^p. The typical order of magnitude adjustment for projecting the vorticity onto the solvability constraints is 10^{-12} which equals the noise resulting from the FFT/FCT.

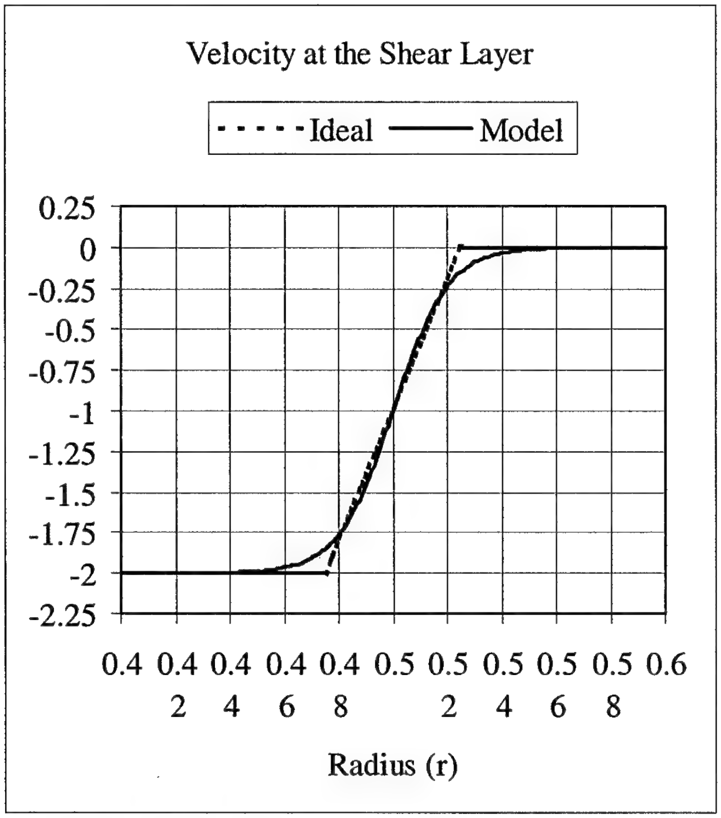

fig 2.1 Velocity profile at the shear layer, $\Delta\Omega = 1$, $a = 0.5$, *and* $\Delta r = 0.05$.

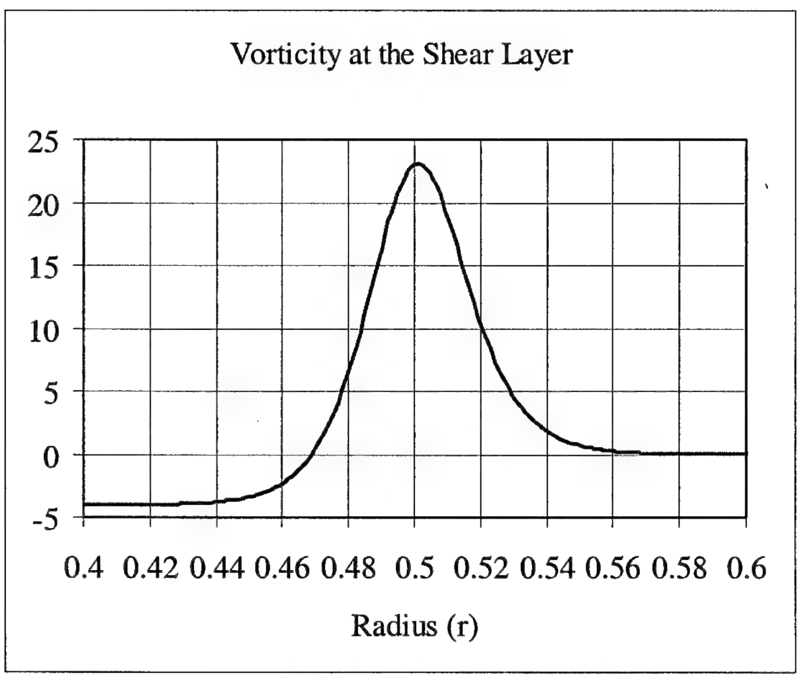

fig 2.2 Vorticity profile induced by the forcing with the radius shown at the shear layer, $\Delta\Omega = 1$, $a = 0.5$, *and* $\Delta r = 0.05$.

2.5.3 Boundary Conditions

While the code can implement free-slip and no-slip boundary conditions (BCs), only the no-slip conditions have been used here. The disk physically terminates in all directions creating a solid boundary enclosing the fluid. Recall the definition of velocity related to the stream function

$$\vec{u} = u_r\hat{e}_r + u_\theta\hat{e}_\theta = \tfrac{1}{r}\partial_\theta\psi\hat{e}_r - \partial_r\psi\hat{e}_\theta$$

Since the walls of the enclosure are solid, no fluid flux exists at the boundary implying the velocity normal to the wall is zero, $u_r\big|_{r=1} = 0$. Note: during implementation the outer radius of the disk boundary, R, is normalized to one, $R = 1$. The no-slip condition implies a fixed velocity tangent to the wall, $u_\theta\big|_{r=1} = U$. These condition produce Dirichlet and Neumann constraints on the stream function. The zero flux requirement gives

$$\partial_\theta\psi\big|_{r=1} = 0$$

while the Neumann conditions result from the no-slip condition

$$\begin{aligned} &\partial_r\psi_n\big|_{r=1} = 0 \text{ for } n > 0 \\ &\partial_r\psi_0\big|_{r=1} = U \end{aligned} \tag{2.10}$$

Combining the zero partials and the potential nature of the stream function gives the Dirichlet conditions

$$\psi_n\big|_{r=1} = 0 \text{ for } n > 0 \tag{2.11}$$

The combination of Dirichlet and Neumann conditions on the stream function means the Poisson equation is overdetermined and the Helmholtz equation underdetermined. Solving the entire system requires transferring one set of BCs onto the vorticity. For our implementation the Poisson equation is solved with the Dirichlet BCs, and the resulting solution is constrained by the Neumann BCs. The Neumann conditions (a.k.a. solvability constraints) are inserted into the Helmholtz problem as tau conditions. Starting with (2.8) where the Dirichlet BCs are implemented as tau conditions, the equation has the form

$$\nabla_\tau^2\vec{\psi}_n^\circ = -\mathbf{R}^2\vec{\omega}_n \tag{2.12}$$

where $\nabla_\tau^2 = \left[\mathbf{R}^2 + \mathbf{RP} - n^2\mathbf{P}^2\right]_\tau$ is the postconditioned Laplacian with the τ conditions included. Now the resulting stream function, $\vec{\psi}_n = \mathbf{P}^2\vec{\psi}_n^\circ$, is forced to meet the Neumann conditions. Since the Laplacian with Dirichlet BCs is well posed and invertible, applying the inverse Laplacian and the postconditioner to both sides of (2.12) yields

(2.13) $$\vec{\psi}_n = \mathbf{P}^2\vec{\psi}_n^\circ = \mathbf{P}^2\left(\nabla_\tau^2\right)^{-1}\left(-\mathbf{R}^2\vec{\omega}_n\right)$$

the Neumann equations are implemented by defining the function $\vec{\tau}_c \equiv \left\langle 0,1,4,9,...,i^2,...,M^2\right\rangle$. Note multiplication of a Chebyshev coefficient vector by $\vec{\tau}_c$ is identical to function evaluation of the derivative at the boundary $r=1$, i.e. $\vec{\tau}_c \cdot \vec{\mu}_n \equiv \partial_r \mu\big|_{r=1}$. Multiplying $\vec{\tau}_c$ into (2.13) and applying the constraint (2.10) yields

(2.14) $$\vec{\tau}_c \cdot \vec{\psi}_n = \vec{\tau}_c \cdot \mathbf{P}^2\left(\nabla_\tau^2\right)^{-1}\left(-\mathbf{R}^2\vec{\omega}_n\right) = 0$$

Define the row vector $\vec{b}_n \equiv \vec{\tau}_c \cdot \mathbf{P}^2\left(\nabla_\tau^2\right)^{-1}$, and $\vec{b}_n \cdot \mathbf{R}^2$ becomes the solvability constraint on vorticity seen by applying the definition to (2.14)

(2.15) $$\vec{b}_n \cdot \mathbf{R}^2\vec{\omega}_n = 0$$

To find the solvability constraint, $\vec{b}_n$, multiply its definition by the Laplacian and transpose the resulting equation for

(2.16) $$\left(\nabla_\tau^2\right)^{\mathrm{T}}\vec{b}_n^{\,\mathrm{T}} \equiv \left(\vec{\tau}_c \cdot \mathbf{P}^2\right)^{\mathrm{T}} \text{ for } n > 0$$

Once the $\vec{b}_n$'s are found (2.15) gives the exact form for the conditions to be included with the Helmholtz problem. These solvability constraints are written as τ conditions in equation (2.9). For the zero Fourier mode, $n=0$, the Poisson equation simplifies giving

$$\tfrac{d}{dr}\left(r\tfrac{d\psi_0}{dr}\right) = -r\omega_0$$

Integrating over the disk gives

(2.17) $$\int_0^{2\pi}\int_0^1 \tfrac{d}{dr}\left(r\tfrac{d\psi_0}{dr}\right)drd\theta = \int_0^{2\pi}\int_0^1 -r\omega_0 drd\theta$$

The left hand side simplifies via the fundamental theorem of calculus and matches condition (2.10) for $n=0$

(2.18) $$\int_0^{2\pi}\int_0^1 \tfrac{d}{dr}\left(r\tfrac{d\psi_0}{dr}\right) r dr d\theta = 2\pi \tfrac{d\psi_0}{dr}\Big|_{r=1} = 2\pi U$$

The right hand side of (2.17) matches the definition for the circulation

(2.19) $$-\int_0^{2\pi}\int_0^1 \omega_0 r dr d\theta = -\int_0^{2\pi}\int_0^1 \omega r dr d\theta = -C$$

Combining the results of (2.18) and (2.19) equates circulation to a constant value, $C = -2\pi U$. Furthermore, the constant circulation implies $\frac{dC}{dt} = 0$. Recall from section 1.2.6 the time evolution of circulation is given by

(2.20) $$\tfrac{dC}{dt} = -2\pi\nu\,\partial_r \omega_0\big|_{r=1} + \tfrac{16\pi\nu}{h^2}\int_0^1 \varpi^* r dr - \tfrac{8\nu}{h^2} C$$

and the resulting value for the circulation is

(2.21) $$C = e^{-\frac{8\nu}{h^2}t} + 2\pi\int_0^1 \varpi^* r dr$$

Rendering (2.21) while including the results in (2.19) and (2.18) shows the tangential velocity at the wall is a function of the initial forcing

$$C = 2\pi\int_0^1 \varpi^* r dr = -2\pi U$$

Incorporating both the representations for circulation into (2.20) gives

$$\tfrac{dC}{dt} = -2\pi\nu\,\partial_r \omega_0\big|_{r=1} + \tfrac{16\pi\nu}{h^2}\int_0^1 \varpi^* r dr - \tfrac{8\nu}{h^2} C = -2\pi\nu\,\partial_r \omega_0\big|_{r=1} \cancel{-\tfrac{16\pi\nu}{h^2}U + \tfrac{16\pi\nu}{h^2}U} = 0$$

This produces the vorticity constraint for Fourier mode zero. The condition has been transformed from the stream function and is applied to the vorticity as a τ condition in the Helmholtz equation

$$\partial_r \omega_0\big|_{r=1} = 0$$

2.5.4 Accurate initiation of the time integration scheme

The 3rd order SBDF has a nominal accuracy of the order $O\left[(\delta t)^3\right]$ where δt is the size of the time step. In order to keep the high accuracy during the initial time steps, the solutions are initially computed with a 1st order SBDF scheme using a time step of $(\delta t)^3$. Define the 1st order time step as

$$\delta_1 = (\delta t)^3$$

The 1st order scheme needs to be repeated for $\frac{1}{\delta t}$ time steps in order to find the initial values for the 2nd order scheme. To start the 2nd order SBDF requires the initial conditions and the flow parameters at time $(\delta t)^2$ because $\delta_2 \approx (\delta t)^2$. Note: the time step here is only approximate since $\frac{1}{\delta t}$ is not necessarily an integer. The actual number of δ_1 time steps is the natural number j such that $\frac{1}{\delta t} \leq j < \frac{1}{\delta t} + 1$. As a result the time step for the 2nd order SBDF is

$$\delta_2 = j(\delta t)^3$$

To find the initial values for the 3rd order SBDF, the 2nd order scheme runs for $2j$ iterations. The values required to start the 3rd order scheme are the initial value, the value at time $j\delta_2$, and the value at time $2j\delta_2$. Thus the final time step is

$$\delta_3 = j^2(\delta t)^3 \approx \delta t$$

The error between the actual time step and the desired time step will equal zero if δt is carefully selected so that $\frac{1}{\delta t}$ is a natural number. In cases where $\frac{1}{\delta t}$ is not a natural number , the maximum time step error with $j < \frac{1}{\delta t} + 1$ is given as

$$\delta_3 - \delta t < (1 + \delta t)^2 \delta t - \delta t = 2(\delta t)^2 + (\delta t)^3$$

Using the $O\left[(\delta t)^3\right]$ accurate start up routine adds a total of $3j - 2$ steps when compared to the $O(\delta t)$ start up.

2.5.5 Time integration scheme

An implicit-explicit time integration method is implemented since the equations contain both linear and nonlinear terms. Linear terms and time integration are included implicitly using a 3rd order BDF scheme while the nonlinear terms enter explicitly, Ascher *et al* [1]. The combination of implicit and explicit terms provides an accurate calculation with a large stability region. The 3rd order SBDF has the form

$$\frac{\frac{11}{6}\alpha^{k+1} - 3\alpha^k + \frac{3}{2}\alpha^{k-1} - \frac{1}{3}\alpha^{k-2}}{\delta t} = 3\beta^k - 3\beta^{k-1} + \beta^{k-2} \tag{2.22}$$

where α is calculated implicitly, β contains the nonlinear terms and is calculated explicitly, δt is the time step, and k is the time level. For our problem the Poisson

equation is solved explicitly at the current time level. The vorticity at a given time produces the stream function at the same time level

(2.23) $$\nabla^2\psi^k = -\omega^k$$

The inverse Laplacian as applied to the vorticity is resolved using the postconditioning method discussed later. Once the stream function and vorticity are on the same time level, the Jacobian is calculated and the Helmholtz equation produces the next vorticity via the SBDF method. The exact form for the calculation is

(2.24)

$$\left[1-\tfrac{6\nu\delta t}{11}\left(\nabla^2-\tfrac{8}{h^2}\right)\right]\omega^{k+1} = \tfrac{6}{11}\left[3\omega^k - \tfrac{3}{2}\omega^{k-1} + \tfrac{1}{3}\omega^{k-2} + \delta t\left(3f^k - 3f^{k-1} + f^{k-2}\right)\right]$$

where $f^k = \frac{8\nu}{h^2}\omega^* - J(\omega^k, \psi^k)$. At this point the vorticity is recast with the r^2 multiplier in order to smooth the flow near the origin singularity. In general the vorticity is represented as

$$\omega(r) = r^2\omega^\circ(r)$$

and the Helmholtz equation is solved for $\omega^\circ(r)$. Variations of this representation exist when solving Fourier modes 0 or 1, and a full description is provided later.

2.5.6 Diagnostics

The primary diagnostics for the code are completed using the energy evolution, enstrophy evolution, and angular momentum evolution. Recall from section 1 the energy evolution is given by

(2.25) $$\tfrac{dT}{dt} = \nu\int_0^{2\pi} u_\theta\omega\Big|_{r=1} d\theta - \nu W + \tfrac{8\nu}{h^2}\int_0^1\int_0^{2\pi} \vec{u}\cdot\vec{u}^* d\theta r dr - \tfrac{16\nu}{h^2}T$$

the enstrophy evolution by

(2.26) $$\begin{aligned}\tfrac{dW}{dt} &= \pi\nu\partial_r\left(\omega^2\right)_0 - 2\nu\int_0^{2\pi}\int_0^1\left(\left(\partial_r\omega\right)^2 + \left(\tfrac{1}{r}\partial_\theta\omega\right)^2\right) r dr d\theta + \\ &\tfrac{16\nu}{h^2}\int_0^1\omega^*\left(\int_0^{2\pi}\omega d\theta\right) r dr - \tfrac{16\nu}{h^2}W\end{aligned}$$

and the angular momentum evolution by

(2.27) $$\tfrac{dA}{dt} = -2\pi\nu\omega_0(1) + 4\pi\nu u_0(1) - \tfrac{16\pi\nu}{h^2}\int_0^1 r^2\left[u_\theta^*(r) - \partial_r\psi_0(r)\right] dr$$

To check the accuracy of the code the left hand sides of (2.25), (2.26), and (2.27) are computed over three time steps using a second order difference scheme. The numerically

computed derivatives are subtracted from their respective right hand sides, and the relative error is computed.

2.6 Forced Periodicity

Investigating secondary bifurcations from steady, inhomogeneous flow requires the classification of stable solutions for various values of the Reynolds number. As with the initial bifurcation from the steady homogeneous solution, the Reynolds number is the appropriate bifurcation parameter. To find the bifurcation, the steady solution is forced into an unstable regime. Artificial stability of a flow is realized by forcing the periodicity of the stable solution beyond the critical value of the Reynolds number. The periodicity of the solution is enforced by equating all other Fourier modes to zero e.g. a period 4 solution is forced by allowing only $4k$ Fourier modes where $0 \le k \le \frac{N+2}{8}$. Using the continuous evolution of eigenvalues through a change in Reynolds number, stable solutions can be tracked onto their associated instability regions.

2.7 Conditioning of the problem

The conditioning for the numerical simulation follows directly from the Helmholtz conditioning, Torres & Coutsias [32]. The Poisson equation is well posed and robust to small perturbation. The Helmholtz equation is derived by applying the SBDF scheme to equation (2.9). The resulting equation is

$$\mathbf{R}^2\mathbf{P}^2\vec{\omega}_n^\circ - \nu\delta t\left[\mathbf{R}^2\mathbf{I}_{[2]} + 5\mathbf{R}\mathbf{I}_{[1]}\mathbf{P} + \left(4-n^2\right)\mathbf{P}^2 + \tfrac{8}{e^2}\mathbf{I}\right]\vec{\omega}_n^\circ = \vec{g}_n \tag{2.28}$$

where $\vec{g}_n$ has the same form as the right hand side of (2.24). In general the linear Helmholtz equation has the form

$$\mathbf{A}\vec{\omega}^\circ = \vec{g} \tag{2.29}$$

where $\vec{\omega}^\circ$ is used to find the vorticity through the smoothing and postconditioning

$$\vec{\omega} = \mathbf{R}^j\mathbf{P}^2\vec{\omega}^\circ \text{ for } j = 1,2 \tag{2.30}$$

To estimate the condition of the problem consider a perturbed linear system (2.29) and a perturbed conversion (2.30)

$$(\mathbf{A} + \delta\mathbf{A})\left(\vec{\omega}^\circ + \delta\vec{\omega}^\circ\right) = \vec{g} + \delta\vec{g} \tag{2.31}$$

$$\vec{\omega} + \delta\vec{\omega} = \left(\mathbf{R}^j + \delta\mathbf{R}^j\right)(\mathbf{P} + \delta\mathbf{P})\left(\vec{\omega}^\circ + \delta\vec{\omega}^\circ\right) \tag{2.32}$$

The conditioning for the problem is measured through the magnitude of the relative error in vorticity. This error compares the norm of the vorticity error to the norm of the vorticity

$$\frac{\|\delta\bar{\omega}\|}{\|\bar{\omega}\|} \equiv \text{condition number}$$

The details for the formulation of the condition number are given in appendix B, but the result is stated here for convenience

$$(2.33) \qquad \frac{\|\delta\bar{\omega}\|}{\|\bar{\omega}\|} \leq \frac{\|\mathbf{A}\|}{\alpha}\left\|\mathbf{R}^{j}\mathbf{P}^{2}\mathbf{A}^{-1}\right\|\left(\chi(g)+2\chi(\mathbf{A})\right)$$

where $\mathbf{A} \equiv \mathbf{R}^2\mathbf{P}^2 - \nu\delta t\left[\mathbf{R}^2\mathbf{I}_{[2]} + 5\mathbf{R}\mathbf{I}_{[1]}\mathbf{P} + \left(4-n^2\right)\mathbf{P}^2 + \frac{8}{h^2}\mathbf{I}\right]$, $0 < \alpha \leq \frac{\|\bar{\omega}\|}{\|\bar{\omega}^{\circ}\|}$, and

$\chi(a) = \frac{\|\delta a\|}{\|a\|}$.

3 Stability Analysis

3.1 Introduction

The fundamental concept for stability analysis addresses how a physical system evolves in time when considering conditions near one of the system's equilibrium states. The flow is perturbed slightly about the state in question, and the evolution of the perturbation is studied. When only terms linear in the perturbation are considered (linearized analysis), results about the stability of the given state are obtainable, but in the case of instability no conclusion can be drawn about the eventual state that will be reached. From experimental work, Rabaud & Couder [25], Niino & Misawa [23], and Früh & Read [15], the bifurcation from the homogeneous flow is known to be a supercritical pitchfork. To derive the form of the bifurcation analytically one must extend the treatment to a weakly nonlinear analysis which includes terms that can produce saturation of the growing perturbation. Such analysis for 2D, rotating fluids has been carried out by Bergeron *et al* [3], Churilov & Shukhman [7], and Niino & Misawa [23] confirming the experimental findings for the first transition from rotational symmetry to small amplitude rotating waves. In this stage of the work we limit our analysis to the linearized problem.

Initially, a specific description of linear stability is provided. Beginning with an equilibrium state, a perturbation is introduced so that the robustness of the equilibrium solution can be investigated. With ε as the perturbation parameter, the perturbed solution resides within an $\varepsilon-$ball of the equilibrium solution, see figure 3.1. The steady system under investigation is autonomous implying that the temporal dependence for disturbances from the equilibrium is of the form $e^{\lambda t}$, where $\lambda \in C$. Evolution times associated with the unstable solutions are finite since perturbed solutions are only considered within the $\varepsilon-$ball. This technique addresses the initial stability of the solution for a given perturbation.

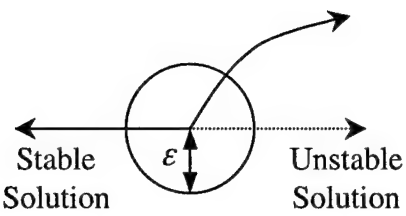

fig 3.1 Linearized solution and bifurcation.

The limitations of this method need to be addressed. As previously stated, unstable solutions cannot be considered for times beyond which the solution is no longer contained within the $\varepsilon-$ball. Saturation of the unstable solution may occur beyond the limits of this analysis. However, the nonlinear terms may drive the perturbed solution away from a solution found to be stable via the linear stability analysis. This second issue does not pose a problem in our case since the spectrum for this system is bounded away from the imaginary axis, and for such operators the linear analysis is sufficient, Trefethen [xx]. In addition, direct numerical simulation demonstrates that the linear behavior dominates the flow evolution near the bifurcation.

3.2 Homogeneous Flow

The homogeneous flow is characterized via the fact that the velocity has no variations in the θ direction. The flow is steady in time, and the perturbation is introduced into both the stream function and vorticity. The problem can be uncoupled in the Fourier expansion so as to consider only a single Fourier mode when applying a perturbation to the problem. To analyze this problem we consider the dimensionless vorticity-stream function equations

(3.1) $$\partial_t \omega + J(\omega,\psi) = \tfrac{1}{\mathrm{Re}}\left[\nabla^2\omega + \tfrac{8}{h^2}\left(\omega^* - \omega\right)\right]$$

(3.2) $$\nabla^2\psi = -\omega$$

where Re is the Reynolds number, $\mathrm{Re} \equiv \frac{a\delta\Omega\beta}{\nu}$; $\delta\Omega$ is the angular velocity of the rigidly rotating flow inside radius a; β is the characteristic length scale; and ω^* is the force applied as a vorticity field.

For the linear stability analysis solutions are perturbed from steady state. Our interest lies in time evolution of the instabilities in an autonomous system. Consider the

steady state problem and write the Laplacian operator for polar coordinates as $\nabla^2 \equiv \partial_r^2 + \frac{1}{r}\partial_r + \frac{1}{r^2}\partial_\theta^2$. The resulting system of equations from (3.1) and (3.2) is

(3.3) $$\tfrac{1}{r}\left(\partial_r\omega\partial_\theta\psi - \partial_r\psi\partial_\theta\omega\right) = \tfrac{1}{\mathrm{Re}}\left[\partial_r^2\omega + \tfrac{1}{r}\partial_r\omega + \tfrac{1}{r^2}\partial_\theta^2\omega + \tfrac{8}{h^2}\left(\omega^* - \omega\right)\right]$$

(3.4) $$\partial_r^2\psi + \tfrac{1}{r}\partial_r\psi + \tfrac{1}{r^2}\partial_\theta^2\psi = -\omega$$

Using the system (3.3)/(3.4), we consider the stability of the azimuthally symmetric flow. For the equilibrium state ω and ψ are only functions of r, and we write the vorticity and stream function as $\omega_0(r)$ and $\psi_0(r)$, respectively. Due to the simplicity of the base state, we consider perturbations of the form …

(3.5) $$\omega = \omega_0(r) + \varepsilon\omega_{n;1}(r)\mathrm{e}^{\lambda t + in\theta}$$

(3.6) $$\psi = \psi_0(r) + \varepsilon\psi_{n;1}(r)\mathrm{e}^{\lambda t + in\theta}$$

where ε is an amplitude parameter, n is the number of the Fourier mode, and λ is an eigenvalue of the n^{th} mode. We seek the form of the corrections $\omega_{n;1}(r)$ and $\psi_{n;1}(r)$ as well as the corresponding eigenvalues.

The θ independence of the base state allows uncoupling of the Fourier modes and provides for the independent consideration of each Fourier mode. After allowing the substitution of $\gamma = \lambda t + in\theta$, the asymptotic expansions, (3.5) and (3.6), are substituted into equations (3.3) and (3.4). The time dependency of the perturbation forces the inclusion of the time derivative term, $\partial_t\omega$. The resulting system is:

(3.7)
$$\varepsilon\omega_{n;1}\lambda\mathrm{e}^\gamma + \tfrac{1}{r}\left[\partial_r\omega_0\left(\varepsilon in\psi_{n;1}\mathrm{e}^\gamma\right) - \partial_r\psi_0\left(\varepsilon in\omega_{n;1}\mathrm{e}^\gamma\right)\right] = \tfrac{1}{\mathrm{Re}}\left(\partial_r^2\omega_0 + \varepsilon\partial_r^2\omega_{n;1}\mathrm{e}^\gamma\right) +$$
$$\tfrac{1}{\mathrm{Re}}\left[\tfrac{1}{r}\left(\partial_r\omega_0 + \varepsilon\partial_r\omega_{n;1}\mathrm{e}^\gamma\right) - \tfrac{1}{r^2}\varepsilon n^2\omega_{n;1}\mathrm{e}^\gamma + \tfrac{8}{h^2}\left(\omega^* - \omega_0 - \varepsilon\omega_{n;1}\mathrm{e}^\gamma\right)\right]$$

(3.8) $$\partial_r^2\psi_0 + \varepsilon\partial_r^2\psi_{n;1}\mathrm{e}^\gamma + \tfrac{1}{r}\left(\partial_r\psi_0 + \varepsilon\partial_r\psi_{n;1}\mathrm{e}^\gamma\right) - \tfrac{1}{r^2}\varepsilon n^2\psi_{n;1}\mathrm{e}^\gamma = -\omega_0 - \varepsilon\omega_{n;1}\mathrm{e}^\gamma$$

Analysis beyond this point considers the system as two separate pieces at distinct orders. The order one, $O(1)$, terms are grouped separately from the order epsilon, $O(\varepsilon)$, terms. The $O(1)$ system involves only the homogeneous flow without perturbations. For Reynolds numbers below the critical value, the $O(1)$ equations

(3.9) $$\partial_r^2\omega_0 + \tfrac{1}{r}\partial_r\omega_0 - \tfrac{8}{h^2}\omega_0 = -\tfrac{8}{h^2}\omega^*$$

(3.10) $$\partial_r^2\psi_0 + \tfrac{1}{r}\partial_r\psi_0 = -\omega_0$$

give the same stream function and vorticity information as the numerical simulation.

The $O(\varepsilon)$ equations pertain to the linear perturbation of the homogeneous problem. Since the system is linear, eigenvalue decomposition can be used to give the stability of the flow for various Reynolds numbers. A positive eigenvalue corresponds to an instability in the homogeneous flow, and during our investigation we search for a pair of eigenvalues that cross the imaginary axis. The $O(\varepsilon)$ systems

(3.11) $$\bar{\omega}_{n;1}\lambda + \tfrac{in}{r}\left(\bar{\psi}_{n;1}\partial_r\bar{\omega}_{n;0} - \bar{\omega}_{n;1}\partial_r\bar{\psi}_{n;0}\right) = \tfrac{1}{\mathrm{Re}}\left(\partial_r^2\bar{\omega}_{n;1} + \tfrac{1}{r}\partial_r\bar{\omega}_{n;1} - \tfrac{n^2}{r^2}\bar{\omega}_{n;1} - \tfrac{8}{h^2}\bar{\omega}_{n;1}\right)$$

(3.12) $$\partial_r^2\bar{\psi}_{n;1} + \tfrac{1}{r}\partial_r\bar{\psi}_{n;1} - \tfrac{n^2}{r^2}\bar{\psi}_{n;1} = -\bar{\omega}_{n;1}$$

are coupled through the vorticity and stream function perturbations. Using the homogeneous flow parameters found by solving (3.9) and (3.10), the system (3.11)/(3.12) is reconstituted as a generalized eigenvalue problem, $\mathbf{A}\vec{\xi} = \lambda\mathbf{C}\vec{\xi}$. For equation (3.11) the partial derivative, $\partial_r\bar{\omega}_{n;0}$ and $\partial_r\bar{\psi}_{n;0}$, are required once the homogeneous vorticity and stream function are known. In order to find these terms directly, (3.9) and (3.10) are differentiated with respect to r. Applying ∂_r to the homogeneous equations yields

(3.13) $$\left(\partial_r^2 + \tfrac{1}{r}\partial_r - \tfrac{1}{r^2} - \tfrac{8}{h^2}\right)\partial_r\bar{\omega}_{n;0} = -\tfrac{8}{h^2}\partial_r\bar{\omega}_n^*$$

(3.14) $$\left(\partial_r^2 + \tfrac{1}{r}\partial_r - \tfrac{1}{r^2}\right)\partial_r\bar{\psi}_{n;0} = -\partial_r\bar{\omega}_{n;0}$$

where the forcing is identically zero for all nonzero Fourier modes, $\bar{\omega}_n^* \equiv 0$ for $n > 0$. Thus the stability problem is resolved by solving (3.13) and (3.14) for $\partial_r\bar{\omega}_{n;0}$ and $\partial_r\bar{\psi}_{n;0}$, and formulating the generalized eigenvalue problem from (3.11) and (3.12).

To begin the singularities are removed through a multiplication by r^2. Recall the functions $\bar{\omega}_{n;0}$, $\bar{\psi}_{n;0}$, $\bar{\omega}_{n;1}$, and $\bar{\psi}_{n;1}$ are functions of r only, not θ, implying they have only Chebyshev expansions. Each of the functions above has an expansion via Chebyshev polynomials e.g. $\bar{\omega}_{n,0} \equiv \left[\omega_{n,0;0} \quad \omega_{n,1;0} \quad \cdots \quad \omega_{n,M;0}\right]^{\mathbf{T}}$,

$\bar{\psi}_{n,1} \equiv \begin{bmatrix} \psi_{n,0;1} & \psi_{n,1;1} & \cdots & \psi_{n,M;1} \end{bmatrix}^{\mathrm{T}}$, etc. The j^{th} entry in the vector is the coefficient for the j^{th} Chebyshev polynomial, namely $T_j(r)$. With the Chebyshev vector representation of vorticity and stream function, multiplication by r and differentiation by r are accomplished using matrix-vector multiplication as described in appendix D. Using the Chebyshev coefficient vectors in combination with $\mathbf{R}$ and $\mathbf{D}$ matrices the equations (3.13) and (3.14) are written in matrix-vector form. After applying the multiplication by r^2 the $O(1)$ equations are

(3.15) $$\left(\mathbf{R}^2\mathbf{D}^2 + \mathbf{RD} - \mathbf{I} - \tfrac{8}{h^2}\mathbf{R}^2\right)\partial_r\bar{\omega}_{n;0} = -\tfrac{8}{h^2}\mathbf{R}^2\partial_r\bar{\omega}_n^*$$

(3.16) $$\left(\mathbf{R}^2\mathbf{D}^2 + \mathbf{RD} - \mathbf{I}\right)\partial_r\bar{\psi}_{n;0} = -\mathbf{R}^2\partial_r\bar{\omega}_{n;0}$$

These equations are straight forward to solve since $\partial_r\bar{\omega}_n^*$ is a given function

$$\partial_r\bar{\omega}_0^* = \tfrac{\Delta\Omega}{ar\Delta r}\operatorname{sech}^2\left(\tfrac{a-|r|}{\Delta r}\right)\left[\tfrac{3}{2} + \tfrac{|r|}{\Delta r}\tanh\left(\tfrac{a-|r|}{\Delta r}\right)\right]$$

The resulting solutions to (3.15) and (3.16) are the vectors $\partial_r\bar{\omega}_{n,0}$ and $\partial_r\bar{\psi}_{n,0}$, and system (3.11)/(3.12) can now be written in matrix-vector form and solved.

To this end apply the multiplication by r^2 and change system (3.11)/(3.12) into matrix-vector representation

(3.17) $$\begin{aligned} &\mathbf{R}^2\bar{\omega}_{n;1}\lambda + in\mathbf{R}\left(\partial_r\bar{\omega}_{n;0} \underset{c}{*} \bar{\psi}_{n;1} - \partial_r\bar{\psi}_{n;0} \underset{c}{*} \bar{\omega}_{n;1}\right) = \\ &\quad \tfrac{1}{\mathrm{Re}}\left(\mathbf{R}^2\mathbf{D}^2 + \mathbf{RD} - n^2\mathbf{I} - \tfrac{8}{h^2}\mathbf{R}^2\right)\bar{\omega}_{n;1} \end{aligned}$$

(3.18) $$\left(\mathbf{R}^2\mathbf{D}^2 + \mathbf{RD} - n^2\mathbf{I}\right)\bar{\psi}_{n;1} = -\mathbf{R}^2\bar{\omega}_{n;1}$$

where $\underset{c}{*}$ represents the convolution of two vectors in Chebyshev mode space. The convolution terms, $\partial_r\bar{\omega}_{n;0} \underset{c}{*} \bar{\psi}_{n;1}$ and $\partial_r\bar{\psi}_{n;0} \underset{c}{*} \bar{\omega}_{n;1}$, are rewritten as a matrix-vector product where $\bar{\psi}_{n;1}$ and $\bar{\omega}_{n;1}$ are the unknowns and retain their vector form. As a result the $\partial_r\bar{\omega}_{n;0}$ and $\partial_r\bar{\psi}_{n;0}$ vectors are written as Chebyshev convolution matrices. The details for writing a vector as a Chebyshev convolution matrix are given in appendix E. Rewriting (3.17) and (3.18) while including the Chebyshev convolution matrices yields

$$\mathbf{R}^2\bar{\omega}_{n;1}\lambda + in\mathbf{R}\left(\overline{\partial_r\bar{\omega}_{n;0}}\bar{\psi}_{n;1} - \overline{\partial_r\bar{\psi}_{n;0}}\bar{\omega}_{n;1}\right) = \frac{1}{\mathrm{Re}}\left(\mathbf{R}^2\mathbf{D}^2 + \mathbf{RD} - n^2\mathbf{I} - \frac{8}{h^2}\mathbf{R}^2\right)\bar{\omega}_{n;1} \tag{3.19}$$

$$\left(\mathbf{R}^2\mathbf{D}^2 + \mathbf{RD} - n^2\mathbf{I}\right)\bar{\psi}_{n;1} = -\mathbf{R}^2\bar{\omega}_{n;1} \tag{3.20}$$

where each convolution matrix is denoted by $\overline{\bar{\zeta}}$ for any coefficient vector $\bar{\zeta}$. At this point the system (3.19)/(3.20) is properly formatted and ready to be rewritten as a generalized eigenvalue problem. When forming the generalized eigenvalue problem, we group the Ekman coefficient term with the eigenvalue giving a new eigenvalue

$$\mu = \lambda + \frac{8}{\mathrm{Re}\,h^2}$$

The form of the generalized eigenvalue problem is $\mathbf{A}\bar{\xi}_n = \mu\mathbf{C}\bar{\xi}_n$ where $\bar{\xi} = \begin{bmatrix} \bar{\omega}_{n;1} \\ \bar{\psi}_{n;1} \end{bmatrix}$ is a compound vector containing both vorticity and stream function. Rewriting the system gives

$$\begin{bmatrix} \frac{1}{\mathrm{Re}}\left(\mathbf{R}^2\mathbf{D}^2 + \mathbf{RD} - n^2\mathbf{I}\right) + in\mathbf{R}\overline{\partial_r\bar{\psi}_{n;0}} & -in\mathbf{R}\overline{\partial_r\bar{\omega}_{n;0}} \\ \mathbf{R}^2 & \mathbf{R}^2\mathbf{D}^2 + \mathbf{RD} - n^2\mathbf{I} \end{bmatrix}\bar{\xi}_n = \mu\begin{bmatrix} \mathbf{R}^2 & 0 \\ 0 & 0 \end{bmatrix}\bar{\xi}_n \tag{3.21}$$

Now to find a specific solution to the generalized eigenvalue system, boundary conditions (BCs) are required. The physical BCs for this flow problem are already satisfied through the $O(1)$ equations. The BCs for the $O(\varepsilon)$ equations are homogeneous since the perturbation has homogeneous end conditions. For the no-slip flow at the boundary, Dirichlet and Neumann conditions are applied to the stream function

$$\begin{aligned} \partial_r\psi_n\big|_{r=\pm1} &= 0 \quad \text{for } n > 0 \\ \partial_r\psi_0\big|_{r=\pm1} &= U \end{aligned} \tag{3.22}$$

$$\psi_n\big|_{r=\pm1} = 0 \tag{3.23}$$

The Neumann conditions are transferred to the vorticity as solvability constraints as explained in section 2.5.3. The Dirichlet conditions are enforced at both ends of the radial grid. We note that all Chebyshev polynomials evaluate to 1 at $r = 1$,

$\forall j \geq 0; T_j\big|_{r=1} = 1$, and the Chebyshev polynomials are equal to ± 1 at $r = -1$,

$\forall j \geq 0; T_j\big|_{r=-1} = (-1)^j$. The vector representations for the Dirichlet BCs are

$$0 = [1 \;\; 1 \;\; \cdots \;\; 1]^{\mathrm{T}} \;\; @\, r = 1$$

$$0 = [1 \;\; -1 \;\; 1 \;\; -1 \;\; \cdots \;\; 1]^{\mathrm{T}} \;\; @\, r = -1$$

These conditions replace the last two stream function equations on both sides of (3.21). The solvability constraints for the vorticity are the vectors, $\vec{b}_n$, found by solving

$$\left(\nabla_\tau^2\right)^{\mathrm{T}} \vec{b}_n^{\,\mathrm{T}} \equiv \left(\vec{\tau}_c \cdot \mathbf{P}^2\right)^{\mathrm{T}}$$

These constraints replace the final vorticity equations on both sides of (3.21).

3.3 Solving the generalized eigenvalue problem, $\mathbf{A}\vec{\xi}_n = \mu \mathbf{C}\vec{\xi}_n$

Several iterative methods are available to solve this problem. Due to the relatively small size of these computations, the generalized eigenvalue problem is solved using MATLAB's QZ implementation. The eigenvalue problem requires the $O(1)$ vorticity and stream function, and equations (3.15) and (3.16) are solved first for the vectors $\partial_r \vec{\omega}_{n;0}$ and $\partial_r \vec{\psi}_{n;0}$. With these initial flow parameters, system (3.21) is solved and the spectrum is recaptured by removing the Ekman coefficient term

$$\lambda = \mu - \tfrac{8}{\mathrm{Re}\,h^2}$$

Each Fourier mode is solved separately so the issue of resolution relates only to the Chebyshev modes. The generalized spectrum contains the dynamics of the physical flow as well as spurious eigenvalues associated with the numerical implementation of the operators. Consider the problem solved with a variety of Chebyshev modes, figure 3.2. In order to separate the physical spectrum from the pseudo-spectrum, a perturbation is introduced to the problem. To perturb the generalized eigenvalue problem, complete spectra are found for three distinct Chebyshev resolutions, and the eigenvalues are compared. The eigenvalues that differ only by the magnitude of the error resulting from the different truncations are kept as these represent the physical spectrum. The "moving" eigenvalues are part of the pseudo-spectra and are discarded.

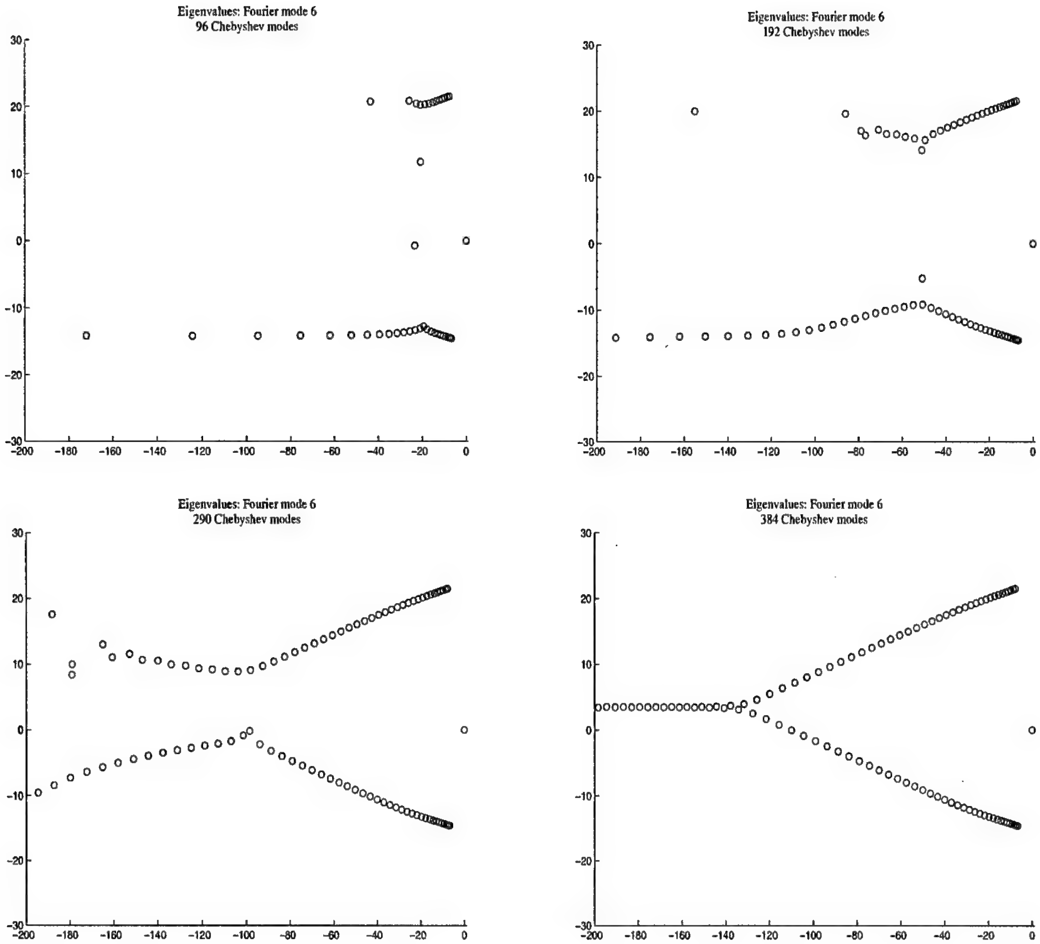

fig 3.2 Eigenvalue plots demonstrating increasing resolution of the physical spectrum corresponding to an increasing number of Chebyshev modes.

The number of computations required to solve the problem is quartered by noticing that equation (3.21) is even. The even nature of the problem implies only even products of Chebyshev and Fourier modes exist. The non zero elements of the $(M+1)\times(M+1)$ Chebyshev matrices appear in the following checkerboard pattern

$$\text{even modes}\rightarrow\begin{bmatrix} * & 0 & * & 0 & * & \cdots & * \\ 0 & * & 0 & * & 0 & \cdots & 0 \\ * & 0 & * & 0 & * & \cdots & * \\ 0 & * & 0 & * & 0 & \cdots & 0 \\ * & 0 & * & 0 & * & \cdots & * \\ \vdots & \vdots & \vdots & \vdots & \vdots & \ddots & \vdots \\ * & 0 & * & 0 & * & \cdots & * \end{bmatrix} \quad \text{odd modes}\rightarrow\begin{bmatrix} 0 & * & 0 & * & 0 & \cdots & 0 \\ * & 0 & * & 0 & * & \cdots & * \\ 0 & * & 0 & * & 0 & \cdots & 0 \\ * & 0 & * & 0 & * & \cdots & * \\ 0 & * & 0 & * & 0 & \cdots & 0 \\ \vdots & \vdots & \vdots & \vdots & \vdots & \ddots & \vdots \\ 0 & * & 0 & * & 0 & \cdots & 0 \end{bmatrix}$$

Due to this structure the boundary conditions are rewritten as linear combinations of one another thus matching the even or odd parity of the problem.

After the BCs have been placed in the generalized eigenvalue problem, the stability of each Fourier mode can be determined by the resulting eigenvalues. An unstable Fourier mode indicates the flow has bifurcated to a new solution.

3.4 Secondary bifurcations

Here we are looking for secondary bifurcations from a steady state, inhomogeneous solution. The steady solution differs from the homogeneous analysis since the solution varies in θ as well as r, and is characterized by a specific number of vortices. Since the flow is now dependent upon azimuthal variations, the analytical perturbations from steady flow are functions of r, θ, and t. As in the homogeneous problem, only terms linear in the perturbation are considered. The forms for the vorticity and stream function steady solutions with perturbations are

(3.24) $$\omega(r,\theta,t)=\omega_0(r,\theta)+\varepsilon\omega_1(r,\theta)e^{\lambda t}$$

(3.25) $$\psi(r,\theta,t)=\psi_0(r,\theta)+\varepsilon\psi_1(r,\theta)e^{\lambda t}$$

Unlike the homogeneous stability analysis, the steady flow characterized through ω_0 and ψ_0 is a function of θ and is obtained from the numerical simulation. Of interest for this perturbation study are the $O(\varepsilon)$ amplitudes ω_1 and ψ_1, and their time evolution given by λ. In the generalized eigenvalue framework λ is the eigenvalue and ω_1 and ψ_1 are the eigenfunctions for this problem. Unlike the homogeneous problem, the system of equations do not uncouple through the Fourier modes and must be solved as a system.

Our interest lies in time evolution of the instabilities in an autonomous system. The resulting system of equations from (3.1) and (3.2) is

(3.26) $$\tfrac{1}{r}\left(\partial_r\omega\partial_\theta\psi-\partial_r\psi\partial_\theta\omega\right)=\tfrac{1}{\mathrm{Re}}\left[\partial_r^2\omega+\tfrac{1}{r}\partial_r\omega+\tfrac{1}{r^2}\partial_\theta^2\omega+\tfrac{8}{h^2}\left(\omega^*-\omega\right)\right]$$

(3.27) $$\partial_r^2\psi+\tfrac{1}{r}\partial_r\psi+\tfrac{1}{r^2}\partial_\theta^2\psi=-\omega$$

Applying the perturbed solutions from (3.24) and (3.25) to the system (3.26)/(3.27) gives the following system of equations:

$$\begin{aligned}&\varepsilon\lambda\omega_1 e^{\lambda t}+\tfrac{1}{r}\left(\partial_r\omega_0\partial_\theta\psi_0-\partial_r\psi_0\partial_\theta\omega_0+\varepsilon\partial_r\omega_1\partial_\theta\psi_0 e^{\lambda t}\right)-\\ &\tfrac{1}{r}\left(\varepsilon\partial_r\psi_0\partial_\theta\omega_1 e^{\lambda t}+\varepsilon\partial_r\omega_0\partial_\theta\psi_1 e^{\lambda t}-\varepsilon\partial_r\psi_1\partial_\theta\omega_0 e^{\lambda t}\right)=\\ &\tfrac{1}{\mathrm{Re}}\left[\nabla^2\omega_0+\varepsilon\nabla^2\omega_1 e^{\lambda t}+\tfrac{8}{h^2}\left(\tilde{\omega}^*-\omega_0-\varepsilon\omega_1 e^{\lambda t}\right)\right]\end{aligned}\tag{3.28}$$

$$\nabla^2\psi_0+\varepsilon\nabla^2\psi_1 e^{\lambda t}=-\omega_0-\omega_1 e^{\lambda t}\tag{3.29}$$

This perturbed system is time independent and can be separated according to two distinct magnitudes, $O(1)$ and $O(\varepsilon)$. Here ω_0 and ψ_0 are already known via numerical simulation of the flow so the $O(1)$ equations are used only to find $\partial_r\vec{\omega}_0$ and $\partial_r\vec{\psi}_0$ directly instead of resorting to matrix vector multiplication, namely $\mathbf{D}\vec{\omega}_0$ and $\mathbf{D}\vec{\psi}_0$. From the system (3.28)/(3.29) the $O(1)$ equations are

$$\tfrac{1}{r}\left(\partial_r\omega_0\partial_\theta\psi_0-\partial_r\psi_0\partial_\theta\omega_0\right)=\tfrac{1}{\mathrm{Re}}\left[\nabla^2\omega_0+\tfrac{8}{h^2}\left(\omega^*-\omega_0\right)\right]\tag{3.30}$$

$$\nabla^2\psi_0=-\omega_0\tag{3.31}$$

The primary equations considered for stability analysis are the $O(\varepsilon)$ equations

$$\begin{aligned}&\lambda\omega_1 e^{\lambda t}+\tfrac{1}{r}\left(\partial_r\omega_1\partial_\theta\psi_0 e^{\lambda t}-\partial_r\psi_0\partial_\theta\omega_1 e^{\lambda t}+\partial_r\omega_0\partial_\theta\psi_1 e^{\lambda t}-\partial_r\psi_1\partial_\theta\omega_0 e^{\lambda t}\right)=\\ &\tfrac{1}{\mathrm{Re}}\left(\nabla^2\omega_1 e^{\lambda t}-\tfrac{8}{h^2}\omega_1 e^{\lambda t}\right)\end{aligned}\tag{3.32}$$

$$\nabla^2\psi_1 e^{\lambda t}=-\omega_1 e^{\lambda t}\tag{3.33}$$

which contain a variety of nonlinear terms resulting from the Jacobian. Using the matrix-vector technique again, system (3.32)/(3.33) is converted to vector form through the Chebyshev and Fourier modal coefficients. Here the form differs from the homogeneous problem since coupled Fourier modes are included in the steady flow, and the coupled modes negate the approached of separating the Fourier modes. A new matrix-vector form is required where the Chebyshev and Fourier modes are included in a single vector. The following expansion is generic and is used for both the stream function and vorticity

$$\zeta(r,\theta)=\sum_{n=0}^{\frac{N}{2}}\sum_{m=0}^{M}\left(\zeta_{nm}^{c}\cos n\theta+\zeta_{nm}^{s}\sin n\theta\right)T_m(r)\tag{3.34}$$

where ζ is either stream function or vorticity (ψ or ω), $T_m(r)$ is the m^{th} Chebyshev polynomial, ζ_{nm}^{c} and ζ_{nm}^{s} are the ζ cosine and sine coefficients, respectively, for the n^{th}

Fourier mode and the m^{th} Chebyshev mode, and the domain for (r,θ) is $-1 \le r \le 1$; $0 \le \theta \le 2\pi$. This expansion establishes the Chebyshev coefficients as the inner expansion i.e. for each Fourier mode the Chebyshev coefficients are together. An alternate characterization is used when only considering the outer, Fourier, expansion:

$$\zeta(r,\theta) = \sum_{n=0}^{\frac{N}{2}} \left(\zeta_n^c(r) \cos n\theta + \zeta_n^c(r) \sin n\theta \right) \tag{3.35}$$

where ζ is either stream function or vorticity (ψ or ω) and $\zeta_n^c(r)$ and $\zeta_n^s(r)$ are the Chebyshev expansion for the n^{th} Fourier cosine and sine modes. Translating the above expression into a vector of coefficients shows the Chebyshev expansion as the inner expansion and the Fourier expansion as the outer expansion. Considering (3.35) in full vector form produces the Fourier vector

$$\vec{\zeta}(r,\theta) = \left[\vec{\zeta}_0^c(r) \quad \vec{\zeta}_1^c(r) \quad \cdots \quad \vec{\zeta}_{\frac{N}{2}}^c(r) \quad 0 \quad \vec{\zeta}_1^s(r) \quad \vec{\zeta}_2^s(r) \quad \cdots \quad \vec{\zeta}_{\frac{N}{2}}^s(r) \right]^{\mathrm{T}}$$

Thus each element in the Fourier vector is a Chebyshev coefficient vector having the same form as the one described for the homogeneous problem, and the result is a single column vector containing $(M+1)(N+2)$ elements. Note the sine zero coefficients (all zeros) are kept to maintain symmetry in the Fourier vector.

With the matrix-vector form defined we consider solutions to the system (3.32) /(3.33). Once again elimination of the singularity occurring at $r=0$ is the first point of consideration. Multiplication by r^2 will remove the point singularity. To maneuver within the full vector space defined above, operations such as differentiation by r and differentiation by θ must be rendered in the appropriate matrices. As with the homogeneous problem, operations on the Chebyshev basis are independent of θ, and this implies the matrices for multiplication and differentiation by r are block diagonal

$$\hat{\mathbf{R}} = \mathbf{I}_{N+2} \otimes \mathbf{R}$$

$$\hat{\mathbf{D}} = \mathbf{I}_{N+2} \otimes \mathbf{D}$$

where $\mathbf{I}_{N+2}$ is the $N+2 \times N+2$ identity matrix. Within the trigonometric basis differentiation by θ corresponds to reassignment of the cosine and sine coefficients while scaling by the mode number

$$\hat{\mathbf{Q}} = \begin{bmatrix} 0 & \mathbf{I}_{\frac{N}{2}+1} \otimes -n\mathbf{I}_{M+1} \\ \mathbf{I}_{\frac{N}{2}+1} \otimes -n\mathbf{I}_{M+1} & 0 \end{bmatrix}$$

where $-n\mathbf{I}_{M+1}$ increments as the $n-1$ row of $\mathbf{I}_{\frac{N}{2}+1}$. Detailed derivations of these matrices can be found in appendix D.

Now that all the tools are in place, rewrite (3.32) and (3.33) in matrix-vector form. First consider the Laplacian operator for polar coordinates, $\nabla^2 \equiv \partial_r^2 + \frac{1}{r}\partial_r + \frac{1}{r^2}\partial_\theta^2$. The point singularity is removed via multiplication by r^2, and after applying the previous definitions, $r^2\nabla^2 = \hat{\mathbf{R}}^2\hat{\mathbf{D}}^2 + \hat{\mathbf{R}}\hat{\mathbf{D}} + \hat{\mathbf{Q}}^2$. Using this representation of the Laplacian and converting the remaining portions of the equations, gives the system in matrix-vector form

$$\begin{aligned} &\lambda\hat{\mathbf{R}}^2\vec{\omega}_1 + \hat{\mathbf{R}}\hat{\mathbf{Q}}\vec{\psi}_0 \underset{F}{*} \hat{\mathbf{D}}\vec{\omega}_1 - \hat{\mathbf{R}}\hat{\mathbf{D}}\vec{\psi}_0 \underset{F}{*} \hat{\mathbf{Q}}\vec{\omega}_1 + \hat{\mathbf{R}}\hat{\mathbf{D}}\vec{\omega}_0 \underset{F}{*} \hat{\mathbf{Q}}\vec{\psi}_1 - \hat{\mathbf{R}}\hat{\mathbf{Q}}\vec{\omega}_0 \underset{F}{*} \hat{\mathbf{D}}\vec{\psi}_1 = \\ &\quad \tfrac{1}{\mathrm{Re}}\left(\hat{\mathbf{R}}^2\hat{\mathbf{D}}^2\vec{\omega}_1 + \hat{\mathbf{R}}\hat{\mathbf{D}}\vec{\omega}_1 + \hat{\mathbf{Q}}^2\vec{\omega}_1 - \hat{\mathbf{R}}^2\tfrac{8}{h^2}\vec{\omega}_1\right) \end{aligned} \tag{3.36}$$

$$\hat{\mathbf{R}}^2\hat{\mathbf{D}}^2\vec{\psi}_1 + \hat{\mathbf{R}}\hat{\mathbf{D}}\vec{\psi}_1 + \hat{\mathbf{Q}}^2\vec{\psi}_1 = -\hat{\mathbf{R}}^2\vec{\omega}_1 \tag{3.37}$$

where $\underset{F}{*}$ is convolution in Fourier space. This system is similar to the homogeneous problem except for the addition of the $\hat{\mathbf{Q}}$ matrix. The existence of coupled Fourier modes increases the number of nonlinear terms resulting from the Jacobian. These nonlinear terms in point space translate to convolutions in Fourier mode space, $\hat{\mathbf{R}}\hat{\mathbf{Q}}\vec{\psi}_0 \underset{F}{*} \hat{\mathbf{D}}\vec{\omega}_1$, $-\hat{\mathbf{R}}\hat{\mathbf{D}}\vec{\psi}_0 \underset{F}{*} \hat{\mathbf{Q}}\vec{\omega}_1$, $\hat{\mathbf{R}}\hat{\mathbf{D}}\vec{\omega}_0 \underset{F}{*} \hat{\mathbf{Q}}\vec{\psi}_1$, and $-\hat{\mathbf{R}}\hat{\mathbf{Q}}\vec{\omega}_0 \underset{F}{*} \hat{\mathbf{D}}\vec{\psi}_1$. The convolutions are resolved by transforming the leading vector into its associated convolution matrix. Since the generalized eigenvalue calculation is not iterative with respect to the Fourier convolutions, the use of fast transforms such as the FFT is not required.

The Fourier convolution matrices, $\overline{\hat{\mathbf{R}}\hat{\mathbf{Q}}\vec{\psi}_0}\hat{\mathbf{D}}$, $-\overline{\hat{\mathbf{R}}\hat{\mathbf{D}}\vec{\psi}_0}\hat{\mathbf{Q}}$, $\overline{\hat{\mathbf{R}}\hat{\mathbf{D}}\vec{\omega}_0}\hat{\mathbf{Q}}$, and $-\overline{\hat{\mathbf{R}}\hat{\mathbf{Q}}\omega_0}\hat{\mathbf{D}}$, are formed following the detailed procedure in appendix F.

The formulation of the generalized eigenvalue problem, $\mathbf{A}\vec{\xi} = \mu\mathbf{C}\vec{\xi}$, can be accomplished in several ways. With both the vorticity and stream function as variables, system (3.36)/(3.37) is written as

$$(3.38)\qquad \begin{bmatrix} \frac{1}{\mathrm{Re}}\left(\hat{\mathbf{R}}^2\hat{\mathbf{D}}^2+\hat{\mathbf{R}}\hat{\mathbf{D}}+\hat{\mathbf{Q}}^2\right)-\overline{\hat{\mathbf{R}}\hat{\mathbf{Q}}\bar{\psi}_0}\hat{\mathbf{D}}+\overline{\hat{\mathbf{R}}\hat{\mathbf{D}}\bar{\psi}_0}\hat{\mathbf{Q}} & \overline{\hat{\mathbf{R}}\hat{\mathbf{Q}}\bar{\omega}_0}\hat{\mathbf{D}}-\overline{\hat{\mathbf{R}}\hat{\mathbf{D}}\bar{\omega}_0}\hat{\mathbf{Q}} \\ \hat{\mathbf{R}}^2 & \hat{\mathbf{R}}^2\hat{\mathbf{D}}^2+\hat{\mathbf{R}}\hat{\mathbf{D}}+\hat{\mathbf{Q}}^2 \end{bmatrix}\bar{\xi}= \mu\begin{bmatrix}\hat{\mathbf{R}}^2 & 0\\ 0 & 0\end{bmatrix}\bar{\xi}$$

where $\bar{\xi}=\begin{bmatrix}\bar{\omega}_1\\ \bar{\psi}_1\end{bmatrix}$ and $\mu=\lambda+\frac{8}{\mathrm{Re}h^2}$. The size of the matrices in (3.38) is $2(M+1)(N+2)\times 2(M+1)(N+2)$ and this size of matrix resolves a problem containing $0\rightarrow M$ Chebyshev modes and $0\rightarrow\frac{N}{2}$ Fourier modes. To reduce the size of the impending eigenvalue calculation, system (3.36)/(3.37) can be written in terms of only the vorticity. Instabilities in the flow are captured as accurately when considering only the vorticity since the onset of the instability is the only feature of interest. This analysis does not make any claims about the flow after an instability has occurred. To write the problem in terms of vorticity only begin by rewriting (3.37) as

$$(3.39)\qquad \bar{\psi}_1=-\left[\hat{\mathbf{R}}^2\hat{\mathbf{D}}^2+\hat{\mathbf{R}}\hat{\mathbf{D}}+\hat{\mathbf{Q}}^2\right]^{-1}\hat{\mathbf{R}}^2\bar{\omega}_1$$

The inverse Laplacian operator is defined when boundary conditions are applied, and this provides a well posed problem. For the no-slip flow Dirichlet boundary conditions are applied to the stream function. Once the stream function is written in terms of the vorticity, equation (3.39) is substituted into (3.36) resulting in a single vorticity equation

$$(3.40)\qquad \begin{aligned}&\overline{\hat{\mathbf{R}}\hat{\mathbf{Q}}\bar{\psi}_0}\hat{\mathbf{D}}\bar{\omega}_1+\left(\overline{\hat{\mathbf{R}}\hat{\mathbf{Q}}\bar{\omega}_0}\hat{\mathbf{D}}-\overline{\hat{\mathbf{R}}\hat{\mathbf{D}}\bar{\omega}_0}\hat{\mathbf{Q}}\right)\left[\hat{\mathbf{R}}^2\hat{\mathbf{D}}^2+\hat{\mathbf{R}}\hat{\mathbf{D}}+\hat{\mathbf{Q}}^2\right]^{-1}\hat{\mathbf{R}}^2\bar{\omega}_1-\\ &-\tfrac{1}{\mathrm{Re}}\left(\hat{\mathbf{R}}^2\hat{\mathbf{D}}^2+\hat{\mathbf{R}}\hat{\mathbf{D}}+\hat{\mathbf{Q}}^2\right)\bar{\omega}_1-\overline{\hat{\mathbf{R}}\hat{\mathbf{D}}\bar{\psi}_0}\hat{\mathbf{Q}}\bar{\omega}_1=-\mu\hat{\mathbf{R}}^2\bar{\omega}_1\end{aligned}$$

In the pure vorticity form only the convolution terms contain non trivial blocks off the main diagonal.

Boundary conditions (BCs) are the final requirement for solving this problem. As before with the homogeneous stability analysis, the BCs for the $\mathrm{O}(\varepsilon)$ equations are homogeneous. The stream function Dirichlet conditions are already included in the Laplacian of (3.39). These conditions are applied by removing the smallest magnitude equations prior to the inversion of the Laplacian. The operator is block diagonal, and the BCs are applied by replacing the last two rows in each $(M+1)\times(M+1)$ block. For the

pure vorticity equation, (3.40), the vorticity solvability constraints, $\vec{b}_n$, are enforced. The solvability constraints are determined as before

$$\left(\nabla_\tau^2\right)^{\mathrm{T}} \vec{b}_n^{\,\mathrm{T}} \equiv \left(\vec{\tau}_c \cdot \mathbf{P}^2\right)^{\mathrm{T}}$$

and enter as the final two rows in each $(M+1)\times(M+1)$ block along the diagonal. In addition elements in the off diagonal columns are required to be zero.

3.5 Solving the generalized eigenvalue problem, $\mathbf{A}\vec{\omega}_1 = \mu\mathbf{C}\vec{\omega}_1$

The generalized eigenvalue problem with the full vorticity vector can no longer be solved with the MATLAB QZ solver. The size of the problem is prohibitive and the LAPACK F77 solver (dggev.f) is used instead. The block structure inherent in $\mathbf{A}$ and $\mathbf{C}$ allows for a reduction in the size of the QZ computation. As with the homogeneous case, this problem is even. The blocks along the diagonal are even while the blocks off the diagonal match the parity of the associated Fourier mode. The matrix with boundary conditions has the form

$$\begin{bmatrix}
* & 0 & * & 0 & \cdots & * & 0 & * & 0 & * & \cdots & 0 & \cdots\cdots & 0 & * & 0 & * & \cdots & 0 \\
0 & * & 0 & * & \cdots & 0 & * & 0 & * & 0 & \cdots & * & \cdots\cdots & * & 0 & * & 0 & \cdots & * \\
* & 0 & * & 0 & \cdots & * & 0 & * & 0 & * & \cdots & 0 & \cdots\cdots & 0 & * & 0 & * & \cdots & 0 \\
\vdots & \vdots & \vdots & \vdots & & \vdots & \vdots & \vdots & \vdots & \vdots & & \vdots & \cdots\cdots & \vdots & \vdots & \vdots & \vdots & & \vdots \\
0 & b_{0;1} & 0 & b_{0;3} & \cdots & 0 & 0 & 0 & 0 & 0 & \cdots & 0 & \cdots\cdots & 0 & 0 & 0 & 0 & \cdots & 0 \\
b_{0;0} & 0 & b_{0;2} & 0 & \cdots & b_{0;M} & 0 & 0 & 0 & 0 & \cdots & 0 & \cdots\cdots & 0 & 0 & 0 & 0 & \cdots & 0 \\
0 & * & 0 & * & \cdots & 0 & * & 0 & * & 0 & \cdots & * & \cdots\cdots & * & 0 & * & 0 & \cdots & * \\
* & 0 & * & 0 & \cdots & * & 0 & * & 0 & * & \cdots & 0 & \cdots\cdots & 0 & * & 0 & * & \cdots & 0 \\
0 & * & 0 & * & \cdots & 0 & * & 0 & * & 0 & \cdots & * & \cdots\cdots & * & 0 & * & 0 & \cdots & * \\
\vdots & \vdots & \vdots & \vdots & & \vdots & \vdots & \vdots & \vdots & \vdots & & \vdots & \cdots\cdots & \vdots & \vdots & \vdots & \vdots & & \vdots \\
0 & 0 & 0 & 0 & \cdots & 0 & 0 & b_{1;1} & 0 & b_{1;3} & \cdots & 0 & \cdots\cdots & 0 & 0 & 0 & 0 & \cdots & 0 \\
0 & 0 & 0 & 0 & \cdots & 0 & b_{1;0} & 0 & b_{1;2} & 0 & \cdots & b_{1;M} & \cdots\cdots & 0 & 0 & 0 & 0 & \cdots & 0 \\
\vdots & \vdots & \vdots & \vdots & \vdots & \vdots & \vdots & \vdots & \vdots & \vdots & \vdots & \vdots & & \vdots & \vdots & \vdots & \vdots & \vdots & \vdots \\
0 & * & 0 & * & \cdots & 0 & * & 0 & * & 0 & \cdots & * & \cdots\cdots & * & 0 & * & 0 & \cdots & * \\
* & 0 & * & 0 & \cdots & * & 0 & * & 0 & * & \cdots & 0 & \cdots\cdots & 0 & * & 0 & * & \cdots & 0 \\
0 & * & 0 & * & \cdots & 0 & * & 0 & * & 0 & \cdots & * & \cdots\cdots & * & 0 & * & 0 & \cdots & * \\
\vdots & \vdots & \vdots & \vdots & & \vdots & \vdots & \vdots & \vdots & \vdots & & \vdots & \cdots\cdots & \vdots & \vdots & \vdots & \vdots & & \vdots \\
0 & 0 & 0 & 0 & \cdots & 0 & 0 & 0 & 0 & 0 & \cdots & 0 & \cdots\cdots & 0 & b_{\frac{N}{2};1} & 0 & b_{\frac{N}{2};3} & \cdots & 0 \\
0 & 0 & 0 & 0 & \cdots & 0 & 0 & 0 & 0 & 0 & \cdots & 0 & \cdots\cdots & b_{\frac{N}{2};0} & 0 & b_{\frac{N}{2};2} & 0 & \cdots & b_{\frac{N}{2};M}
\end{bmatrix}$$

The form of the vorticity vector also alternates parity as the Fourier mode

$$\vec{\omega}_1 = [* \;\; 0 \;\; * \;\; 0 \;\; * \;\; 0 \;\; \cdots \;\; 0 \;\; 0 \;\; 0 \;\; 0 \;\; 0 \;\; \cdots \;\; 0 \;\; 0 \;\; * \;\; 0 \;\; * \;\; 0 \;\; \cdots \;\; 0]^{\mathrm{T}}$$

The vector, $\mathbf{A}\vec{\omega}_1$, resulting from the checkerboard pattern in $\mathbf{A}$ contains only $\frac{(M+1)(N+2)}{2}$ non zero values. This effectively reduces the size of the generalized eigenvalue problem by a factor of four. The only relevant terms in $\mathbf{A}$ are

$$\mathbf{A}\left[1:2:(M+1)(N+2),1:2:(M+1)(N+2)\right]$$

and the actual size of the generalized eigenvalue problem is $\frac{(M+1)(N+2)}{2}\times\frac{(M+1)(N+2)}{2}$.

Even with the reduction in size, the primary concern for this problem is the fact that $\mathbf{A}$ and $\mathbf{C}$ are large. Investigation of 500 Chebyshev modes and 200 Fourier modes requires the solution of a $2{,}500{,}000{,}000$ element generalized eigenvalue problem. This severely limits the size of the Chebyshev-Fourier expansion that can be considered. However, two facts allow this generalized eigenvalue problem to be solved in an efficient manner. Recall the $(M+1)\times(M+1)$ Chebyshev convolution matrices are formed from vectors containing $2M+1$ modes. This allows for the consideration of 500 Chebyshev modes using a matrix of size 250×250. Next, the forced periodicity of the solution allows for the consideration of a greater number of Fourier modes. The flow field in the numerical simulation is forced into a specified symmetry. When an $n=6$ braid is forced only the $n=6k$ Fourier modes need to be considered. As a result 500 Chebyshev modes and 200 Fourier modes form a problem with only $18{,}000{,}000$ elements.

4 Results

4.1 Introduction

The stability of a two-dimensional, rotating fluid in a bounded geometry has been studied through experimentation and analysis using two basic geometries, thin annular regions or thin cylinders (disks). The disk and annular geometries exhibit similar dynamics for low Reynolds numbers as shown is section 4.2. The initial bifurcation is robust to several forms of forcing and varying aspect ratios[1]. For higher Reynolds numbers the post on the inside of the annulus interferes with the evolution of the asymmetric tripole which appears to be the high Reynolds number limit for the disk flow as shown in section 4.3. The Ekman pumping we have selected closely resembles the forcing implemented in the experiments by Früh & Read [15], and direct comparisons are made between their observations and our simulations. For transitions beyond the initial bifurcation, section 4.4 discusses symmetry breaking bifurcations leading to periodic and irregular states.

An adequate parameterization for the transition between states is provided by the Reynolds number, Hide & Titman [18]. In general, the Reynolds number is the ratio of inertial force to viscous force

$$\mathrm{Re} = \frac{UD}{\nu}$$

where U is the characteristic velocity scale, D is the characteristic length scale, and ν is the viscosity. Throughout the field of rotating shear layer stability, two methods are used to define the Reynolds number, Dolzhanskii *et al* [11]. The definitions differ in the choice of the characteristic length scale: one method uses the cell height while the other uses the shear layer thickness. Dolzhanskii [10] shows the quasi-two-dimensional problem is accurately represented by using the shear layer thickness as the characteristic length scale. Our definition for the Reynolds number is

$$\mathrm{Re} = \frac{\Delta\Omega a L}{\nu}$$

where $\Delta\Omega$ is the angular velocity, a is the distance to the shear layer, and L is the shear layer thickness.

[1] aspect ratio is defined as the cell height divided by the location of the shear layer

4.2 Homogeneous instability

The initial onset of flow instability in the disk mirrors the results found for the annular geometry, Bergeron *et al* [3]. Near the center of the disk, the flow is similar to rigid body rotation which produces little impact on the initial instability when compared to the annular geometry. To demonstrate this idea, we compare the disk initial instabilities to those of the annular region in Bergeron *et al* [3]. The annular region is forced such that the shear layer develops at a distance of $\frac{3}{4}R$ from the center where R is the outer radius of the annulus, see figure 4.1.

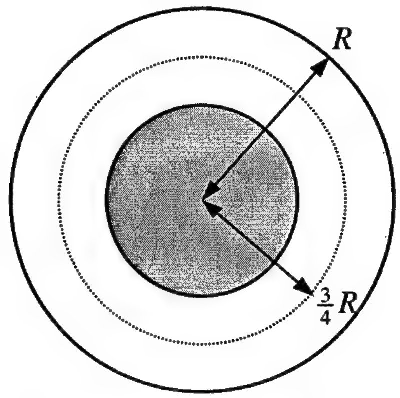

fig 4.1 In the annulus the shear layer is developed at $\frac{3}{4}R$.

Bergeron *et al* [3] define the Reynolds number using the cell height for the length scale instead of the shear layer thickness so our parameters are adapted to their definition. The cell aspect ratio is defined as

$$\Gamma = \frac{a}{h}$$

where a is the distance from the center of the disk to the shear layer and h is the height of the cell. We consider the two extreme cases from Bergeron *et al* [3] where the aspect ratios are $\Gamma = 6.5$ and $\Gamma = 10$, respectively. The Reynolds number defined in Bergeron *et al* [3] is

$$\mathrm{Re} = \frac{\Delta\Omega\alpha h}{\nu}$$

where α is the ratio $\alpha = \frac{R_o + R_i}{R_o - R_i}$ for an annulus with outer radius R_o and inner radius R_i. Regarding the disk geometry $\alpha = 1$ is the closest approximation. The normalization of the disk sets $R = 1$ and implies the shear layer develops at $a = 0.75$. Considering the

$\Gamma = 6.5$ case first, the resulting height is $h = 0.1154$. The viscosity is set, $\nu = 2 * 10^{-3}$, and now the Reynolds number is only a function of the angular velocity, $\Delta\Omega$. Applying forcing at the $\frac{3}{4}$ radius gives excellent correspondence between the disk and annulus regarding the onset of instability, see figure 4.2.

The agreement between these simulations begins to deteriorate at modes above and below the critical Fourier mode, $n = 5$. Modes less than the critical Fourier mode begin to exacerbate the differences between the disk and annular geometries. As shown in section 4.3, the disk and annulus dynamics differ considerably for lower Fourier modes especially $n \leq 2$. Variations in the modes above the critical Fourier mode are a function of increased angular velocity and the shear layer modeling. Bergeron *et al* [3] use a cubic spline to model the velocity transition while we use a hyperbolic tangent.

The second case with $\Gamma = 10$ provides even better agreement between the two stability analyses. For this second case the height is $h = 0.075$. The lower height increases the Ekman pumping coefficient and reduces the shear layer thickness. The marginal stability is shown in figure 4.3. The variation in the lower modes is consistent with the previous diagram. The consistency of the homogeneous instability demonstrates the closely related nature of these simulations at low Reynolds numbers

The experiments completed by Rabaud & Couder [25] and Chomaz *et al* [6] agree with the analysis of the initial instabilities as discussed in Bergeron *et al* [3]. The Landau equations, Bergeron *et al* [3], show that the bifurcation from steady flow is a supercritical pitchfork in the mean rotating reference frame. Früh & Read [15] confirm the initial instability as a Hopf bifurcation in the non-rotating frame. For the remainder of the results we consider the shear layer at the midpoint of the radius, $a = 0.5$. The height and Ekman pumping coefficient are also adjusted to maintain an aspect ratio of ten, $\Gamma = 10$. The complete list of parameters is given here

$$h = L = 0.05$$

$$\nu = 2 * 10^{-3}$$

$$a = 0.5$$

$$\frac{8\nu}{h^2} = 6.4$$

$$\Gamma = 10$$

The marginal stability of the Fourier modes is shown in figure 4.4.

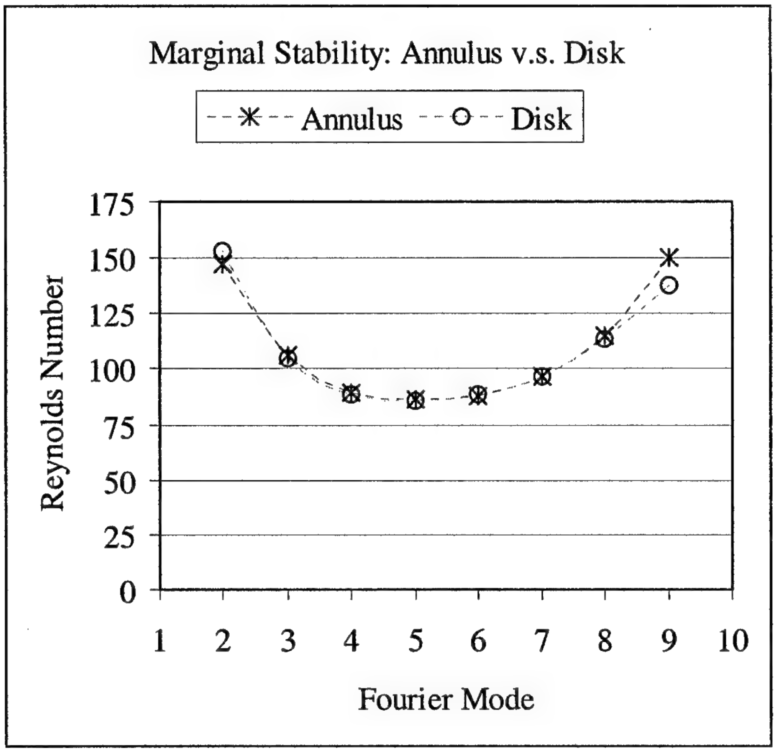

fig 4.2 Initial instability by Fourier mode $\Gamma = 6.5$ *and* $a = 0.75$.

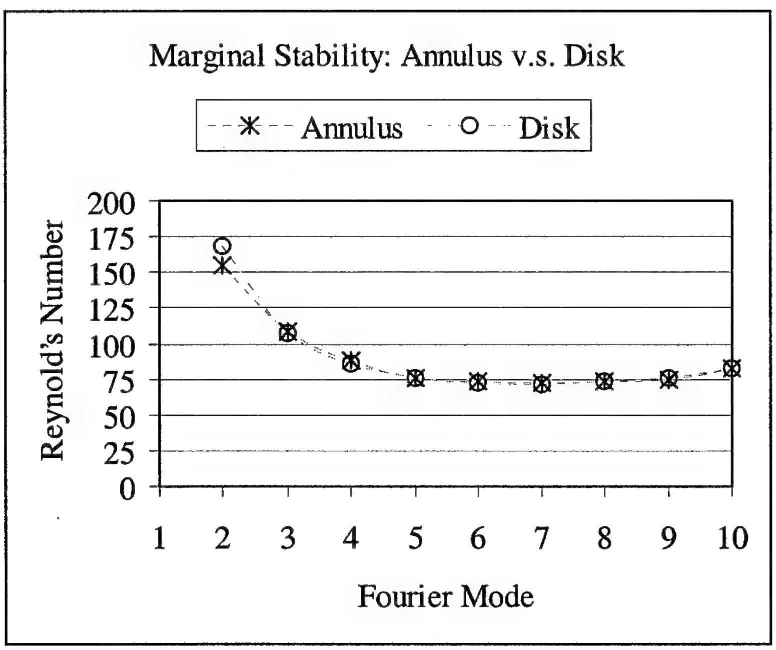

fig 4.3 Initial instability by Fourier mode $\Gamma = 10$ *and* $a = 0.75$.

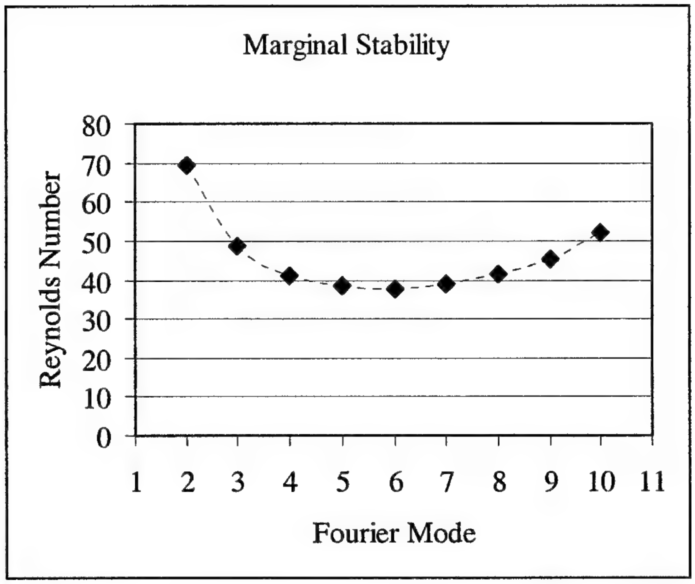

fig 4.4 Marginal stability for $a = 0.5$ *and* $h = 0.05$.

The Reynolds numbers used for these calculations differs from the ones used in Bergeron *et al* [3] per the difference in definitions. Recall we use the Reynolds number dependent on the shear layer thickness, L, as discussed in section 4.1

$$\mathrm{Re} = \frac{\Delta\Omega a L}{\nu}$$

While the actual values of the Reynolds number cannot be compared between figures 4.3 and 4.4, one notes the reduction in the critical Fourier mode number when the shear layer is located closer to the center of the disk, for a given aspect ratio. The same reduction in critical mode number also occurs when the aspect ratio is reduced, Niino & Misawa [23] and Bergeron *et al* [3]. The eigenvalue analysis described in section 3.3 demonstrates the systematic development of the pseudospectrum from right to left as additional Chebyshev modes are retained in the analysis. Comparison of three resolutions separates the spurious eigenvalues from those of physical spectrum. The resulting spectrum for the initial bifurcation at $n = 6$ is shown in figure 4.5. The spectrum is adjusted to the mean rotating frame, and the bifurcation appears as a supercritical pitchfork. The critical value of the Reynolds number for the onset of instability is $\mathrm{Re} = 37.8$.

At $\mathrm{Re} = 40$ just beyond the initial bifurcation, an $n = 6$ braid begins to form. A visualization of the flow is provided in figure 4.7. As the Reynolds number is increased, enstrophy is added to the system increasing the strength of the vortices in the braid, see figure 4.17. The method of increasing the Reynolds number is discussed in section 4.3.

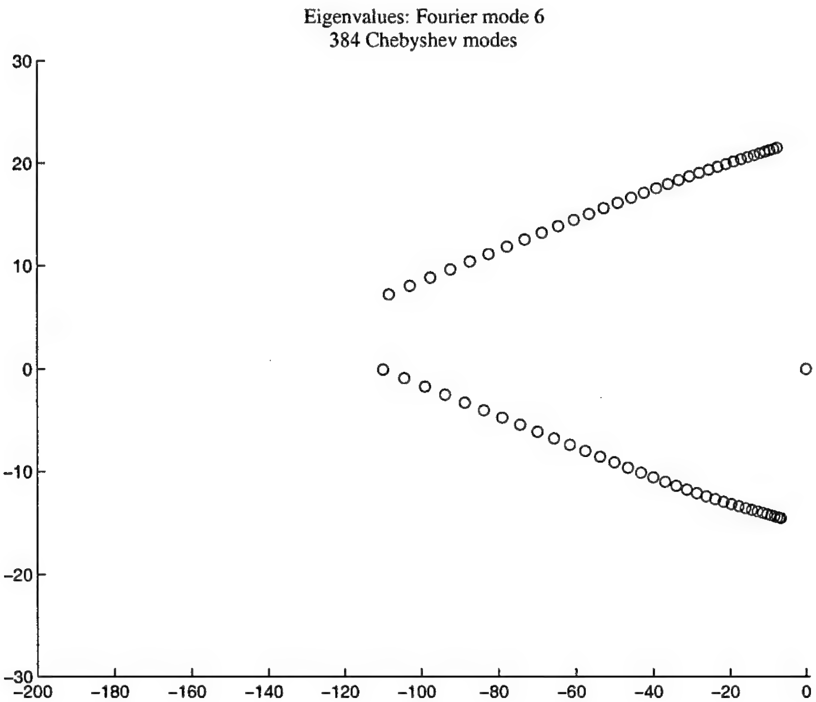

fig 4.5 The eigenvalues for Fourier mode 6 with the pseudospectra removed.

The Ekman pumping coefficient is a function of height and viscosity. When a shear layer remains constant and the height is reduced to $h = 0.02$, the marginal stability curve shifts due to the increase in aspect ratio see figure 4.6. These results are consistent with the experimental work of Rabaud & Couder [25] and the analysis of Bergeron *et al* [3]. For the increased aspect ratio, the critical mode moves from $n = 6$ to $n = 8$ while the critical Reynolds number increases by more than a factor of three. Numerical simulation of the thin 2D flow allows for investigation of cell heights unrealizable via an experimental apparatus. These investigations may lead to further analysis of the secondary transitions for $n \geq 8$ flows. Chomaz *et al* [6] and Früh & Read [15] report transitions at high mode number which they are unable to analyze.

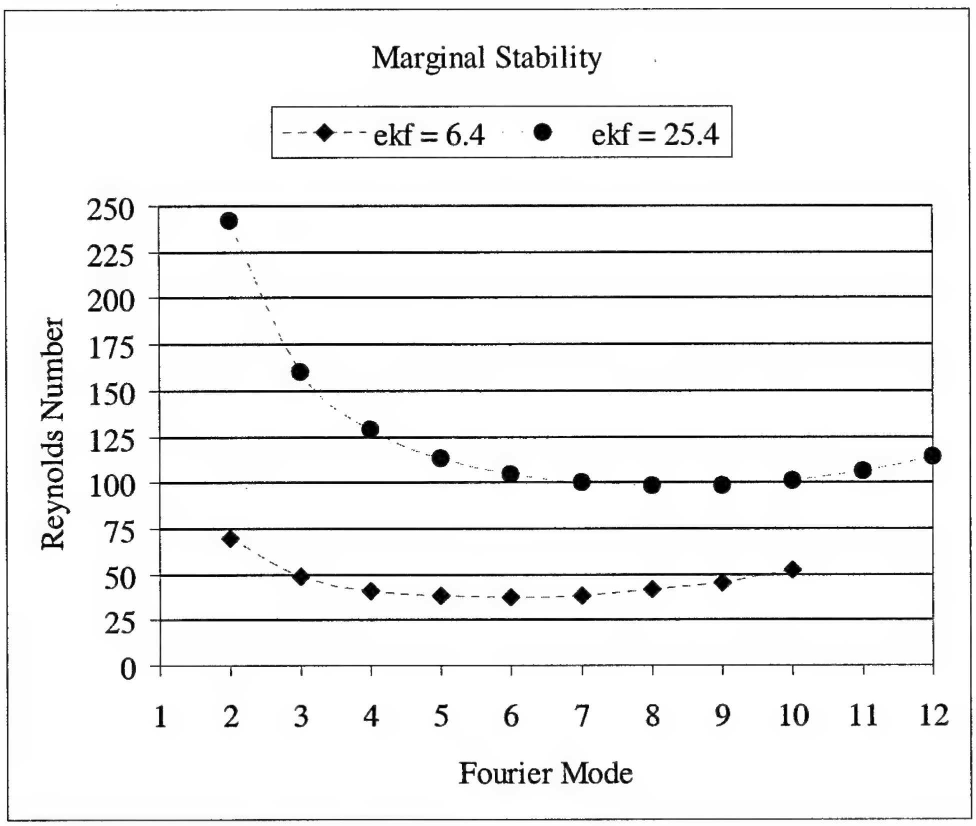

fig 4.6 The marginal stability of the rotating flow for $h = .05$ *which gives the Ekman coefficient of* $ekf = 6.4$ *and* $h = .02$ *which gives* $ekf = 25.4$.

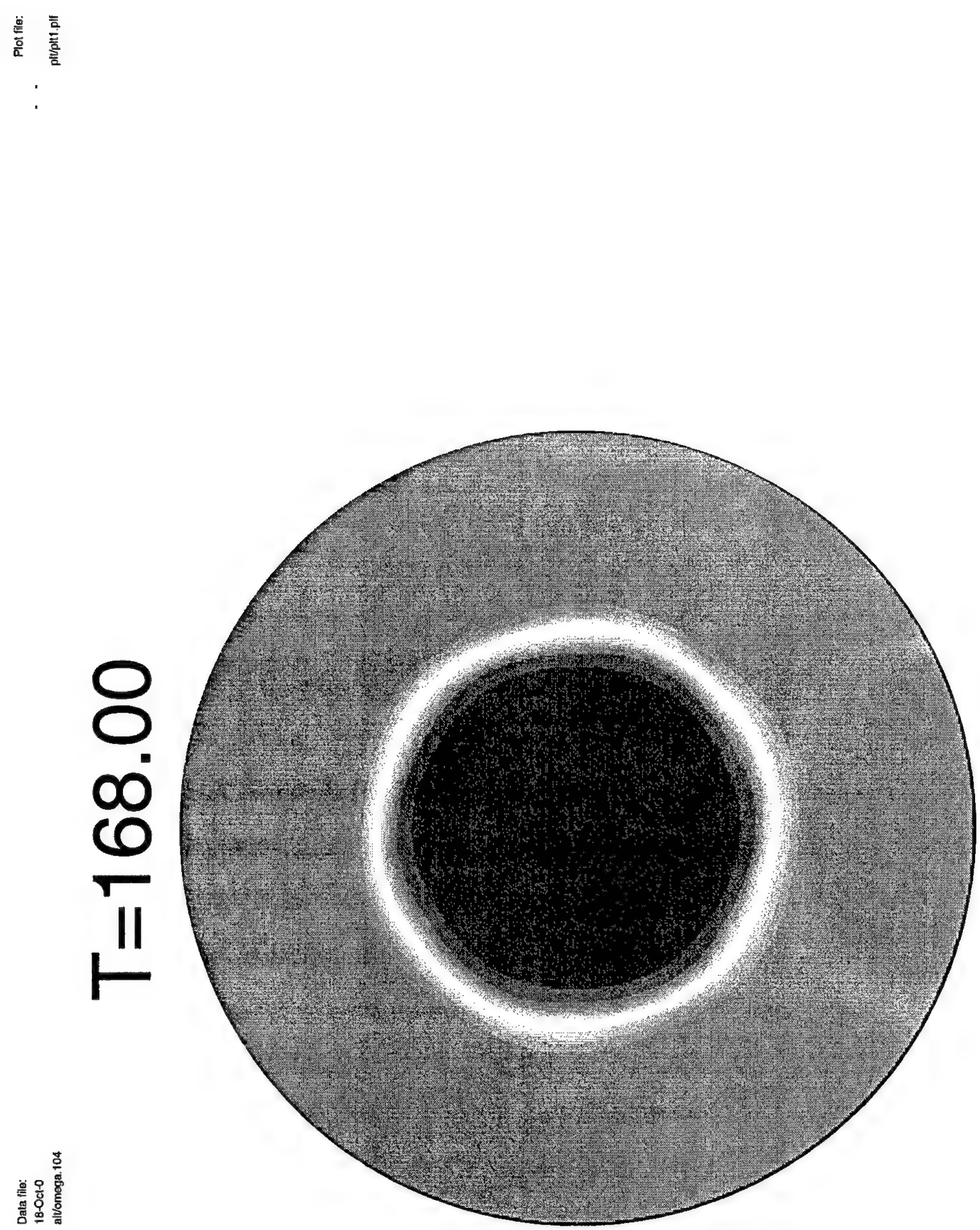

fig 4.7 Flow at Re = 40 *just after the initial Hopf bifurcation.*

4.3 Asymmetric tripole

Transitions of the flow beyond the initial bifurcation culminate in the asymmetric tripole. The similarity between the annulus and disk simulations breaks down as the flow is driven to higher Reynolds numbers and through the secondary bifurcations. The high Reynolds number flow leads to stability with $n \leq 2$ and forms an asymmetric tripole. The forms of the tripole are only accessible within the annular geometry by implementing artificial boundary conditions that de-emphasize the wall. Section 4.4 provides additional discussion on the secondary bifurcations occurring prior to the point vortex.

The flow in the disk geometry transitions to a single, coherent vortex, "point vortex", after the $n = 3$ braid becomes unstable. Experiments using annular regions have unsuccessfully attempted to develop the point vortex flow. A symmetric balance exists in the annular region, Niino & Misawa [23], for the $n = 2$ solution. This balance also exists for the disk geometry, Konijnenberg *et al* [20], but as the Reynolds number is increased, the symmetric $n = 2$ solution gives way to the asymmetric tripole, $n = 2 \oplus 1$. One of the outer vortices begins to collapse forming the point vortex, while the other expands and shears. The result is a steady point vortex paired with a steady or periodic sheet like vortex on the antipodal side. As the Reynolds number is increased the point vortex continues to increase in strength. Figures 4.8 and 4.9 show a typical point vortex solution at $\mathrm{Re} = 250$. Note the 3rd Fourier mode has more energy than the 4th.

The parameter space for the asymmetric tripole is filled with complex dynamics from the steady $n = 2$ flow to the periodic $n = 2 \oplus 1$. The rate of Reynolds number transition can move the flow into any one of several attractors. For the numerical simulation, the Reynolds number is typically incremented every 50 iterations by a factor of $6.25 * 10^{-5}$. This allows the flow 50 iterations to relax between adjustments while still providing a steady rate of change. A different form of the asymmetric tripole is seen in figure 4.10. This state is found after a period doubling bifurcation from the $n = 4 \oplus 2$ steady state to an $n = 2 \oplus 1$ steady state, figure 4.11. Here the 4th Fourier mode has more energy than the 3rd, and one can see the impact on the form of the tripole. Although beyond the scope of this thesis, our spectral simulation provides a tool for the complete exploration of the parameter space associated with the asymmetric tripole.

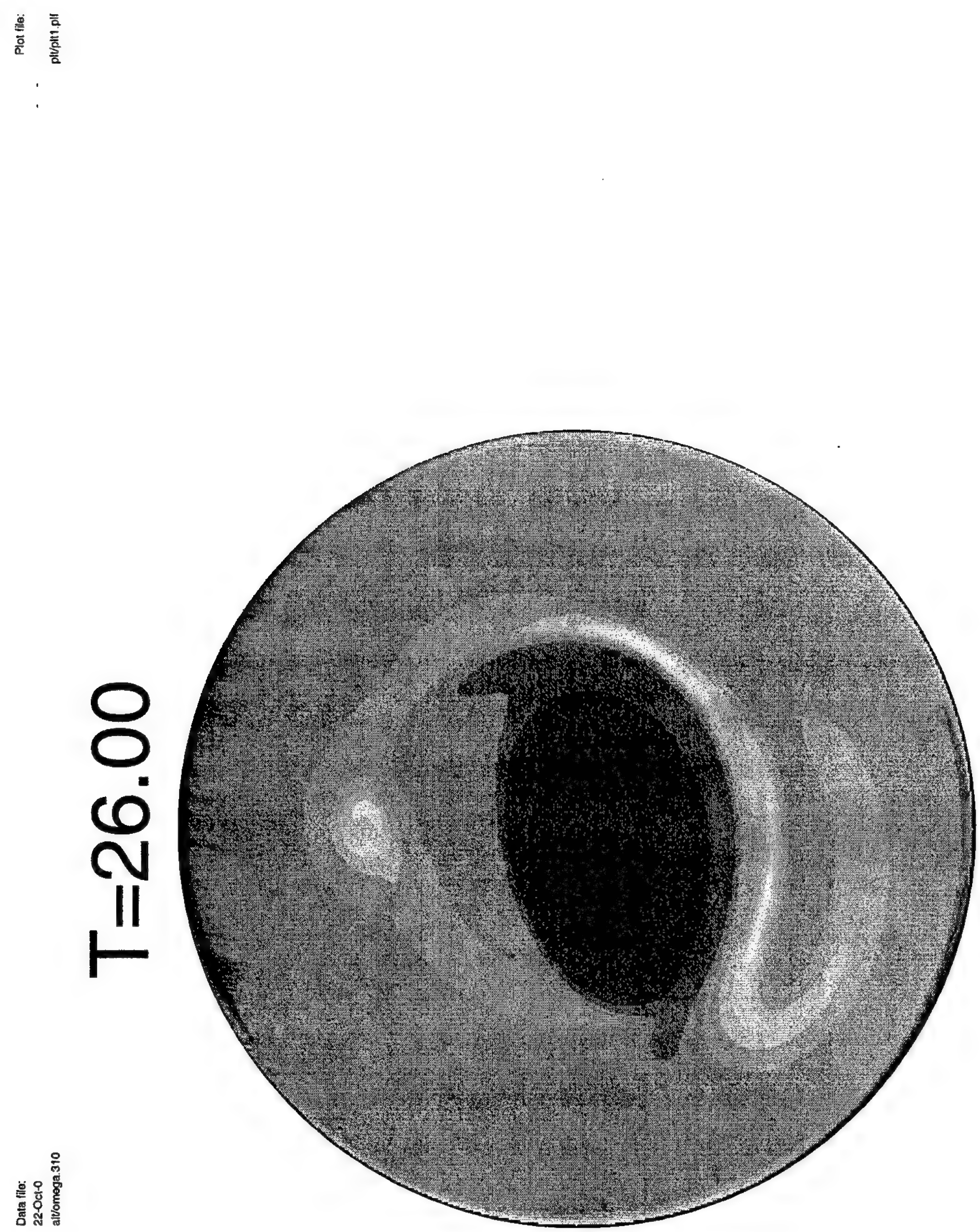

fig 4.8 Point vortex flow at Re = 250.

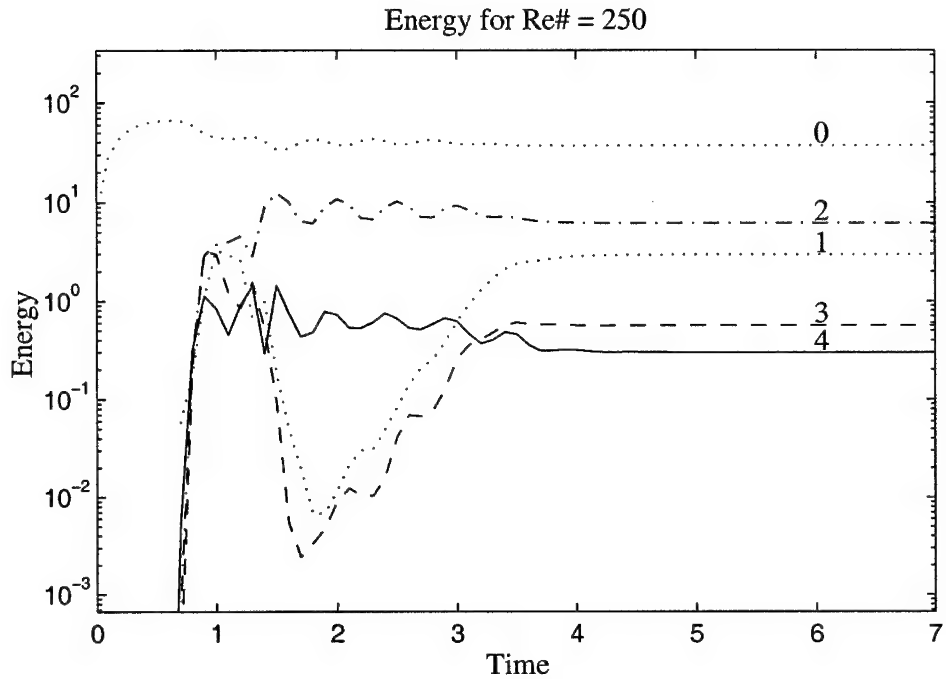

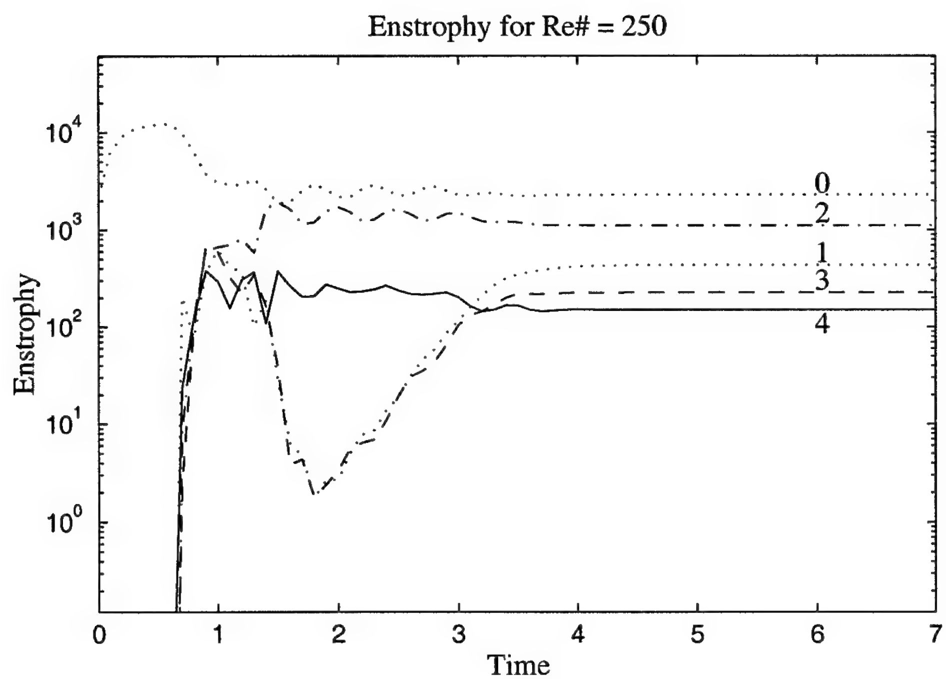

fig 4.9 Energy and enstrophy for the $2 \oplus 1$ *point vortex.*
The numbers correspond to Fourier modes.

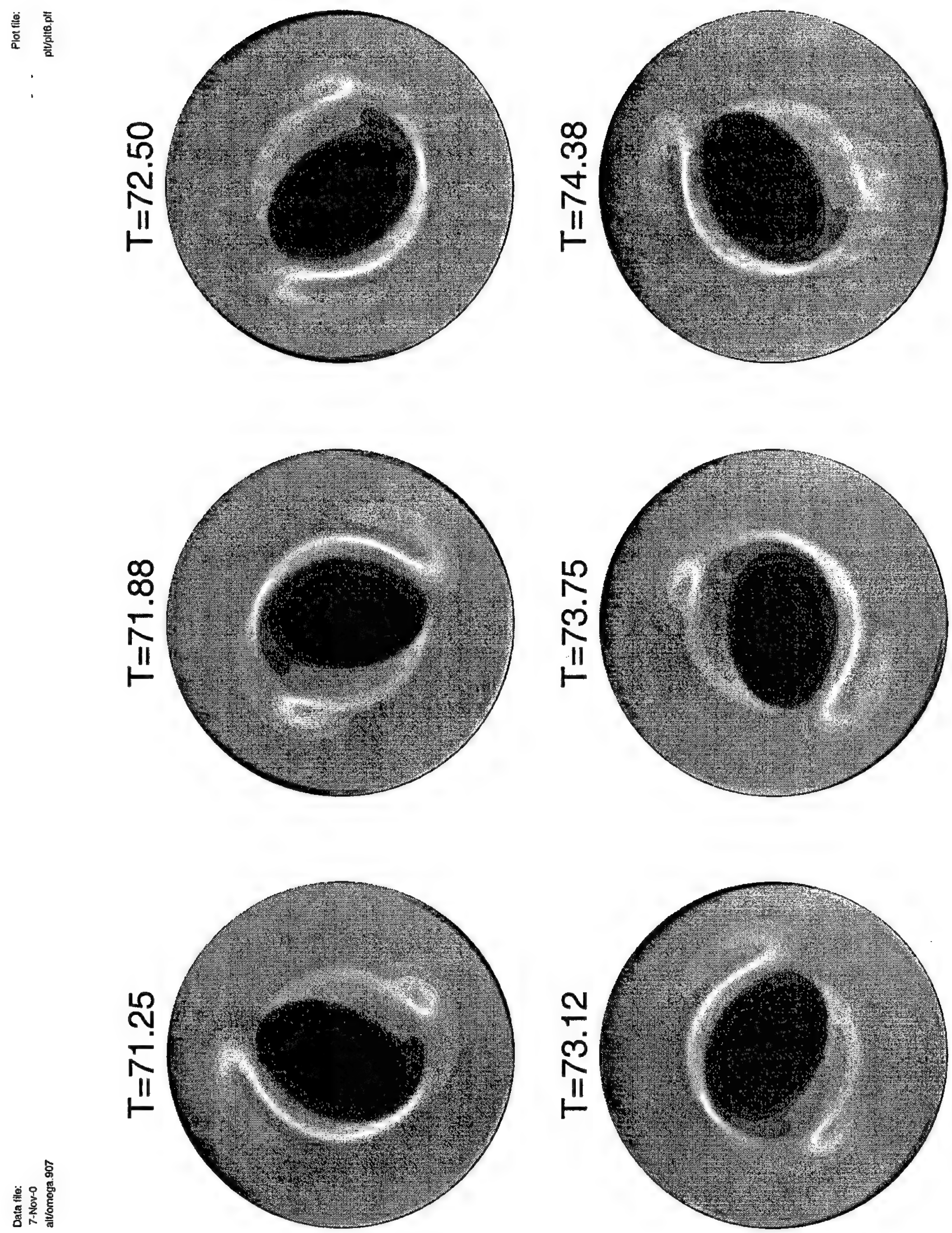

fig 4.10 The asymmetric tripole with more energy in mode $n = 4$ *than in mode* $n = 3$.

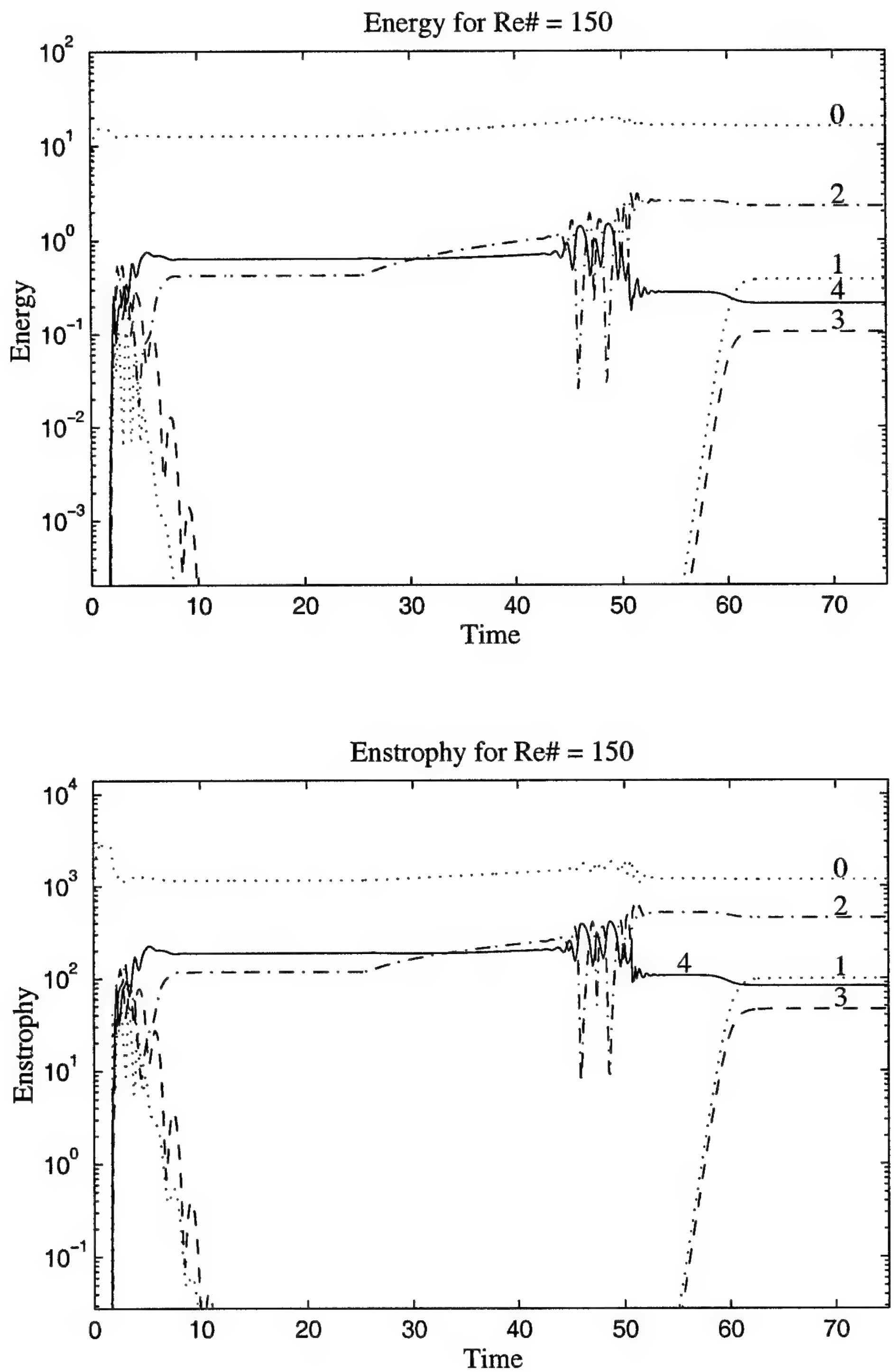

fig 4.11 Energy and enstrophy for the transition from $4 \oplus 2$ *steady to a* $2 \oplus 1$ *point vortex. The numbers correspond to Fourier modes.*

4.4 Secondary bifurcation

Transitions occurring after the initial bifurcation offer a breadth of rich dynamics. The equilibrium solution found beyond the initial bifurcation is a braid of n vortices. As the Reynolds number is increased beyond the critical value, stability of the initial vortex braid is lost, and a transition to a subsequent vortex braid occurs. With a smooth, slow increase of the Reynolds number the new stable braid consists of $n-1$ vortices. Rapid transitions can bypass the $n-1$ attractor and lead to other bifurcations such as period doubling. As the Reynolds number increases, the $n-1$ transition is often preceded by a transition to quasi-periodic states, and Chomaz *et al* [6] investigate the $n=4 \rightarrow n=3$ transition through two symmetry breaking bifurcations and a temporal bifurcation. Früh & Read [15] perform a careful experimental study over a wide range of Reynolds numbers. Their detailed search of the parameter space provides characterization of the initial supercritical pitchfork bifurcation, period doubling bifurcations, irregular flow regions, and modal transitions. Vortices with unusually high levels of white noise are reported for specific profiles. Rand [26] analyzes the transitions from periodic flows to modulated (quasi-periodic) flows. For our purposes a periodic flow is defined as a flow which is periodic in time with respect to the mean rotating coordinate system. A quasi-periodic flow exhibits multiple, spatial or temporal frequencies.

4.4.1 Period doubling

Once the flow is stable with an even number of vortices, the period doubling bifurcation results from the first spatial symmetry breaking, Rand [26], and exhibits a direct exchange of energy between the mode n and the mode $\frac{n}{2}$. When the rate of change of Reynolds number is fast enough, period doubling bifurcations can be found. Früh & Read [15] experimentally analyze period doubling bifurcations and report smooth transitions during these bifurcations. Our simulations confirm the smooth transitions for $n=6 \rightarrow n=3$ period doubling and reveal the sensitive nature of the dynamics

Flow initially forced to $\mathrm{Re}=75$ stabilizes as an $n=5$ braid and flow initially forced to $\mathrm{Re}=60$ stabilizes as an $n=6$ braid. If the fluid velocity is ramped from $\mathrm{Re}=60$ to $\mathrm{Re}=75$ at a rate of $1.25/\text{unit time}$, the flow experiences a period doubling bifurcation. This transition is shown in figures 4.13 and 4.14. However, if the flow is

ramped from $\mathrm{Re}=60$ to $\mathrm{Re}=67.5$ and allowed to stabilize and then ramped from $\mathrm{Re}=67.5$ to $\mathrm{Re}=75$, the period doubling does not occur and the final state is the $n=5$ braid.

In order to analyze the period doubling bifurcations, periodicity is enforced on the flow. As an example the flow at $\mathrm{Re}=75$ is naturally $n=5$ braid, figures 4.15 and 4.16, but can be forced to maintain an $n=6$ braid by allowing only the $n=6k$ Fourier modes to exist, see figure 4.17. The $n=6$ flow is unstable when additional Fourier modes are considered in the eigenvalue analysis. To introduce the spectral analysis, we consider stabilized flow shortly after the initial bifurcation, $\mathrm{Re}=40$, figure 4.7. Here the periodicity is not enforced since the flow naturally consists of only $n=6k$ Fourier modes. The eigenvalue analysis for this flow results in figure 4.12. The flow is a stable $n=6$ with the leading order eigenvalues having $Re[\lambda]=-5.96$. To find bifurcations to quasi-periodic or period doubling solutions, we consider the flow in an unstable region with forced periodicity.

Accurate determination of the instability requires inclusion of all the Fourier modes. This increases the size of the eigenvalue calculation from □ 20,000,000 elements to ~ 200,000,000 elements. The computational horsepower required to solve these problems in not currently available. Therefore, this analysis is reserved for future investigation as some additional shortcuts may be found to reduce the size of the eigenvalue problem and computational capability is always increasing.

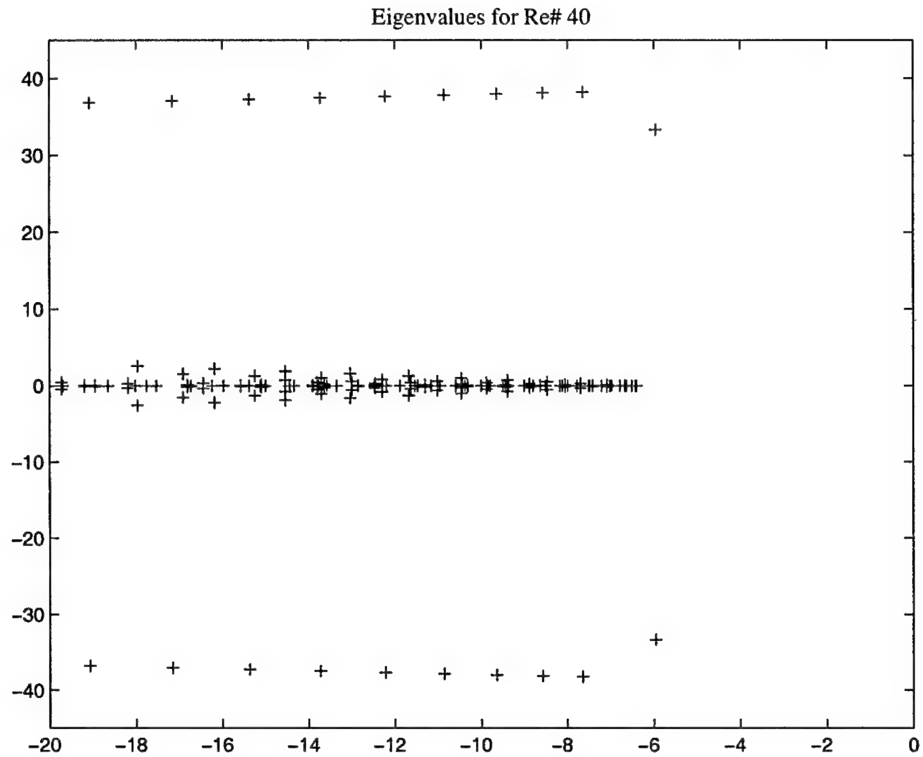

fig 4.12 Spectrum for the stable $n = 6$ *braid at* $\mathrm{Re} = 40$.

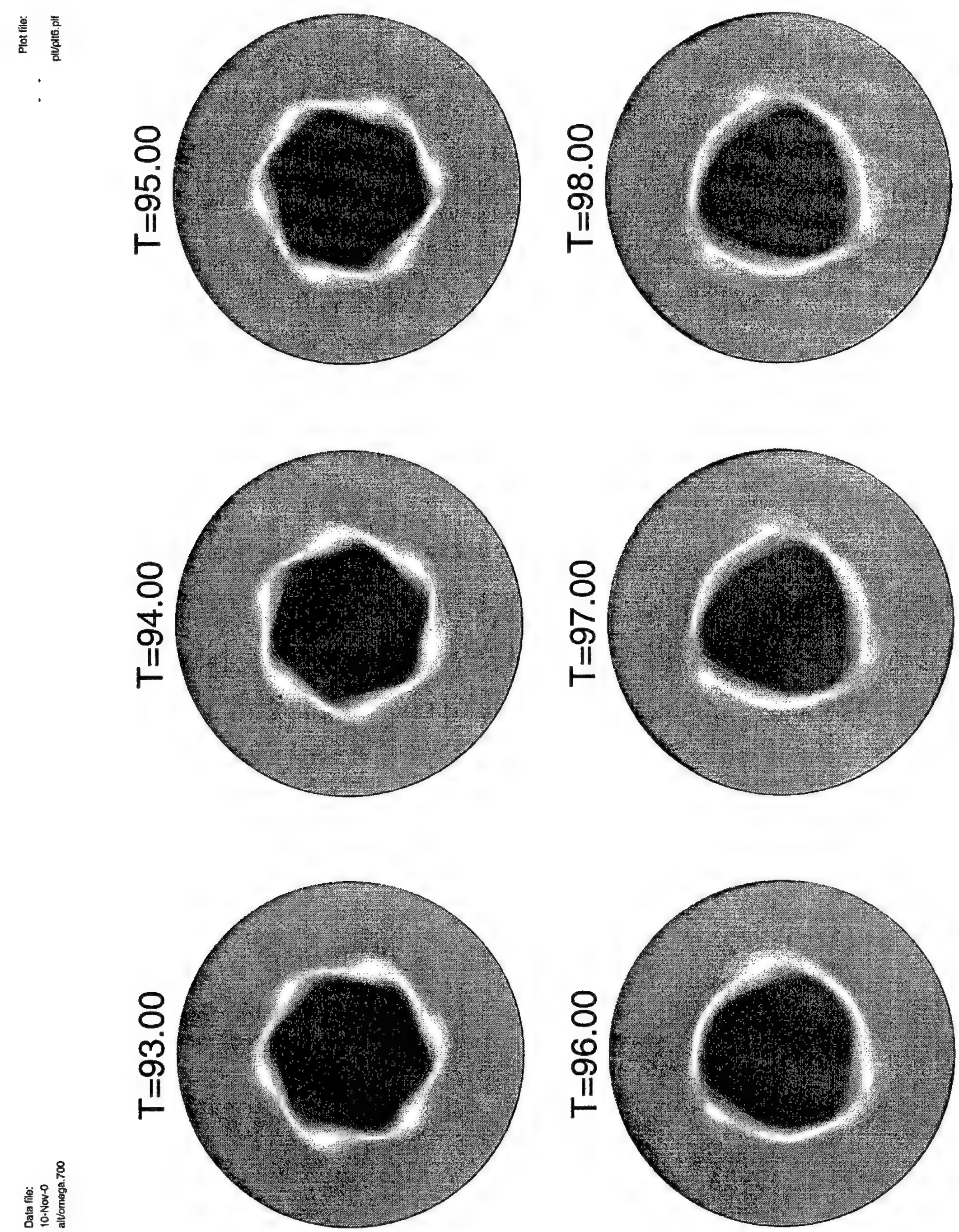

fig 4.13 Flow before and after a period doubling bifurcation, $n = 6 \rightarrow n = 3$. *The Reynolds number is ramped up from 60 to 75, and all the Fourier modes are allowed to interact.*

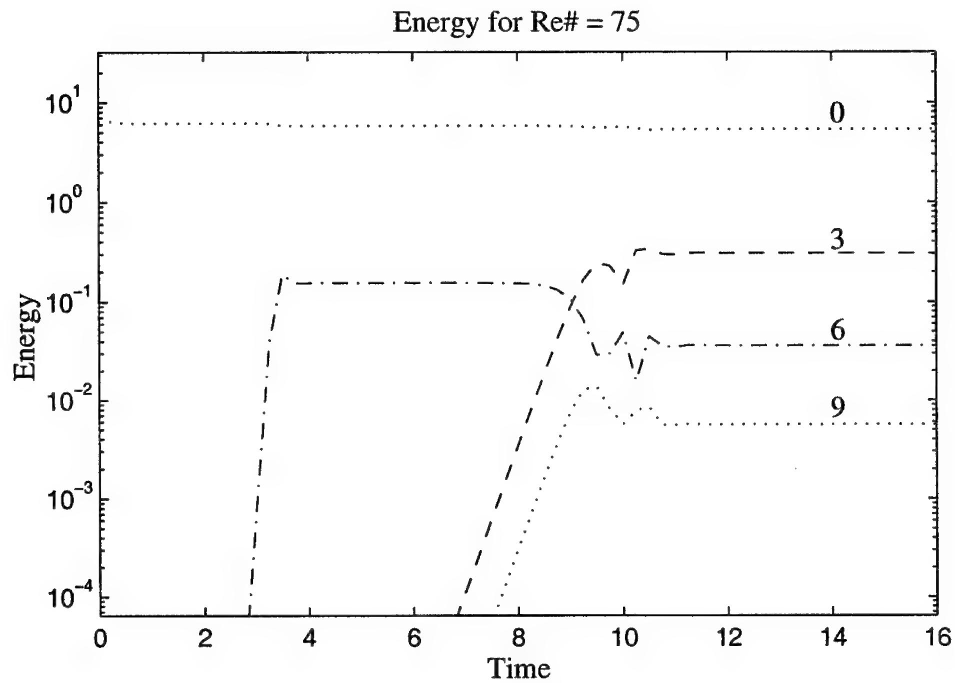

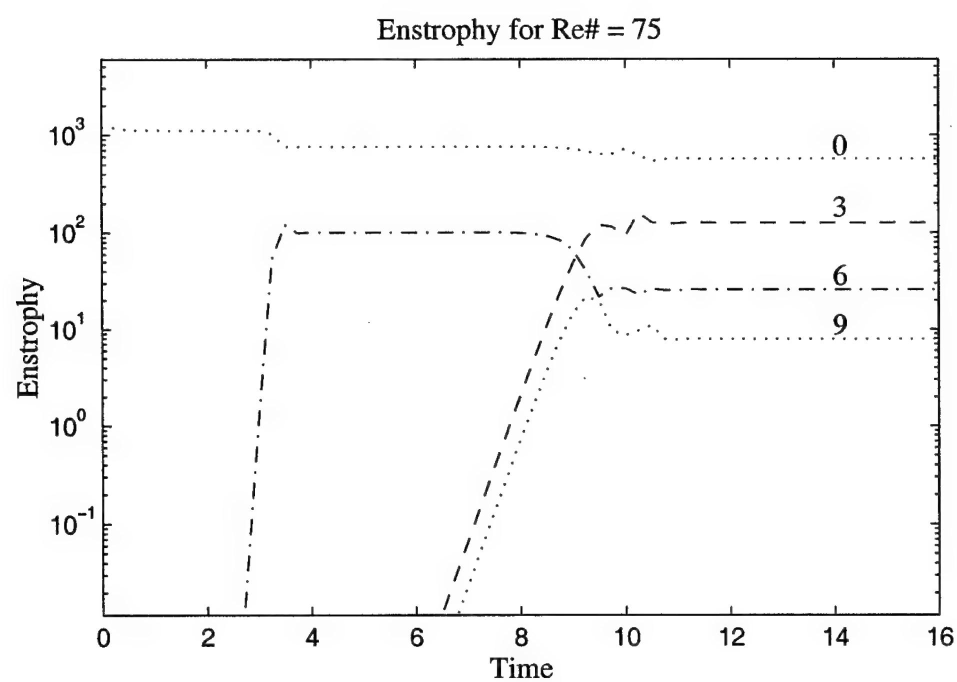

fig 4.14 Energy and enstrophy for the $n = 6 \rightarrow n = 3$ period doubling bifurcation. The numbers correspond to Fourier modes.

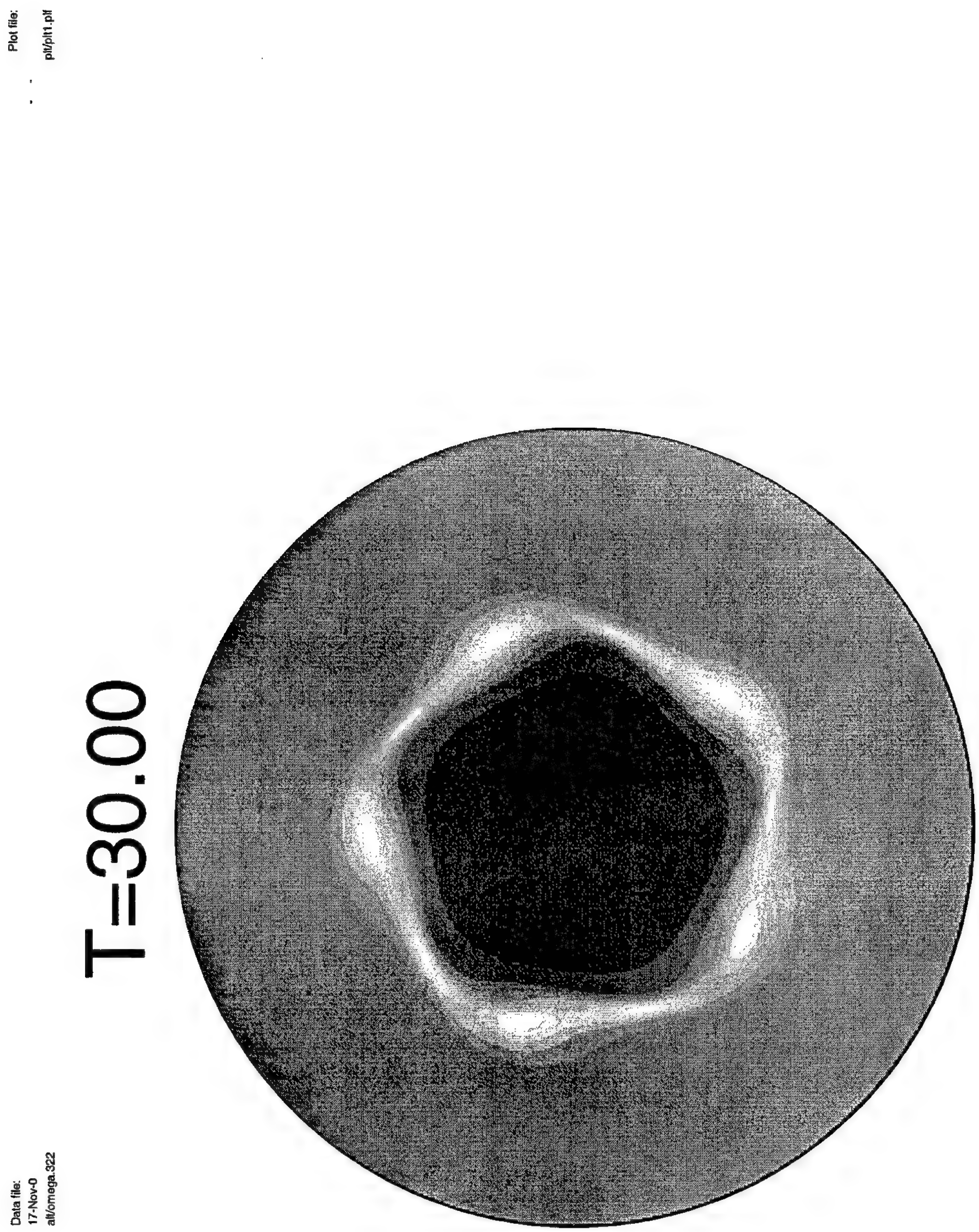

fig 4.15 Flow at Re = 75 *without forced periodicity.*

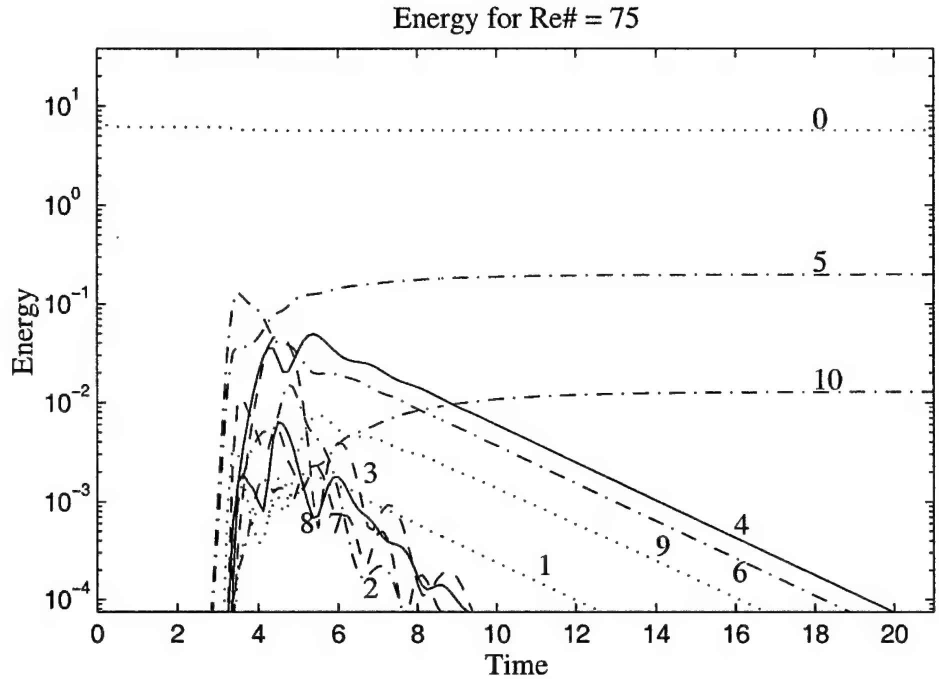

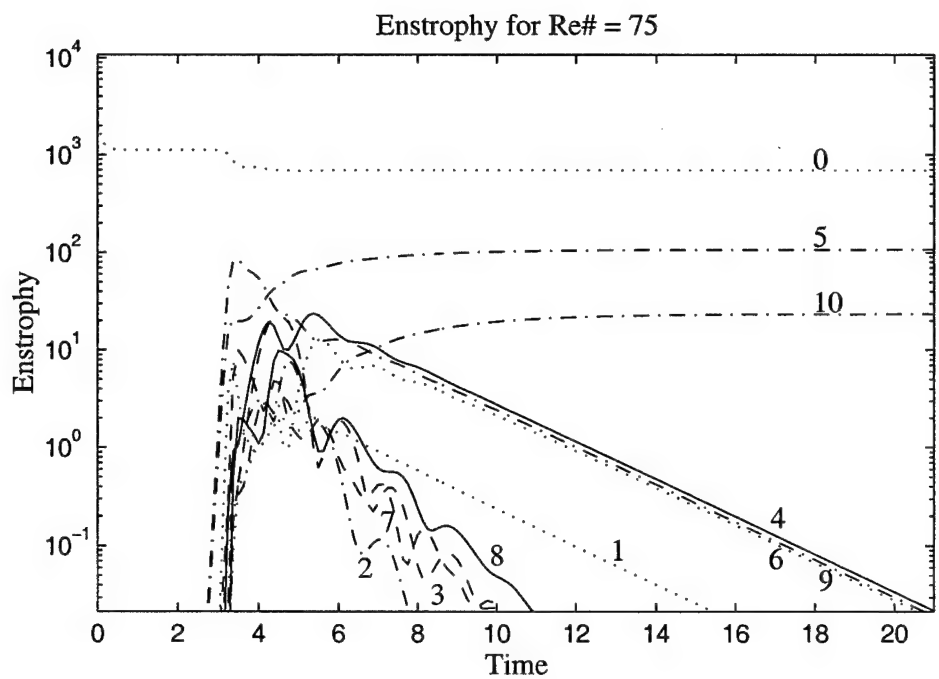

Fig 4.16 Energy and enstrophy for the $n = 5$ braid.
The numbers correspond to Fourier modes.

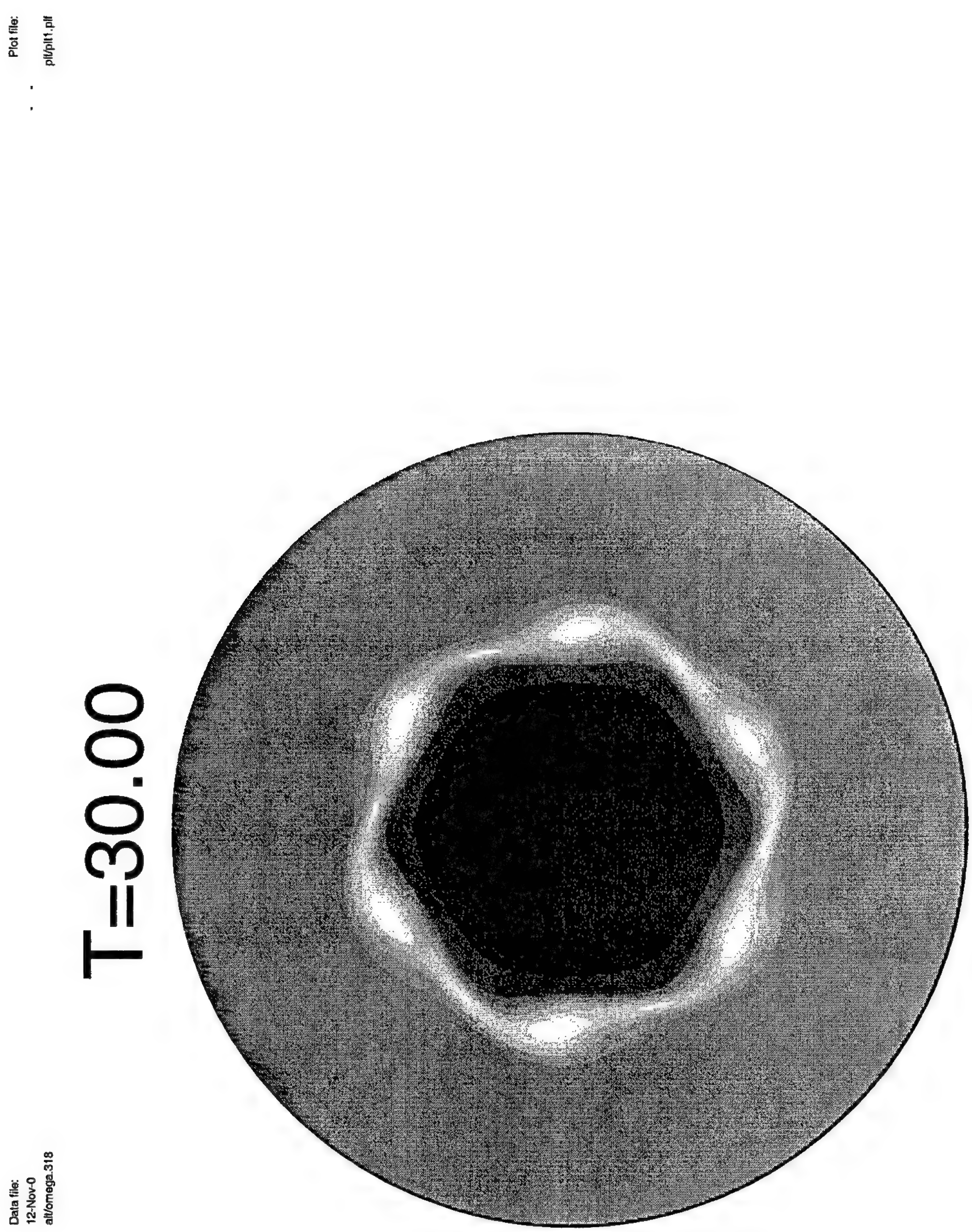

fig 4.17 Flow at $\mathrm{Re} = 75$ *with periodicity* $n = 6k$ *enforced.*

4.4.2 Oscillatory states

Transitions to periodic states has been observed in various experiments, Chomaz *et al* [6], Yao & Zabusky [35], Früh & Read [15], and Konijnenberg *et al* [20]. Konijnenberg *et al* [20] and Yao & Zabusky [35] report a periodic $n = 3$ solution while Chomaz *et al* [6] find the $n = 4 \oplus 2$ and $n = 4 \oplus 2 \oplus 3$ modulated waves. In the wide parameter search by Früh & Read [15], both the periodic $n = 3$ and $n = 4 \oplus 2$ states are reported. In addition, irregular flows are revealed for specific combinations of Rossby number and Ekman number. Near the irregular flow regimes, Früh & Read [15] observe "noisy" vortices where "... the 'noisy' flows not only exhibited an increased level of relatively uniform fluctuations, but also frequent spikes in the signal of the same order of magnitude as the vortex signal itself." They investigated the noisy vortices by using singular systems analysis (SSA) to reconstruct the flow phase space. After performing the SSA analysis, they conclude, "that the noisy vortices do not contain any more information or further deterministic dynamics (as could have been indicated by the enhanced eigenvalues of the second pair of eigenvectors), but that the noisy vortex state contains the same deterministic dynamics as the periodic vortices only with added white noise." It is our conjecture that Früh & Read [15] were near the $n = 4 \oplus 2 \oplus 3$ periodic state, but were not close enough to isolate the mode 3 contribution.

The $n = 4 \oplus 2 \oplus 3$ is seen by Chomaz *et* al [6] as the second symmetry breaking bifurcation when the flow transitions from $n = 4 \rightarrow n = 3$. We have found the state to exist as a periodic solution for a small range of Reynolds numbers. The time evolution of the $n = 4 \oplus 2$ and $n = 4 \oplus 2 \oplus 3$ periodic states is shown in figures 4.19 and 4.21, respectively. The associated energy and enstrophy evolutions are included in figures 4.20 and 4.21. All transitions are assumed to be complete since the vortex structures have not changed for over 250 cycles of their respective turn around times. In addition to the reports by Chomaz *et al* [6] and Früh & Read [15] we find two distinct $n = 4 \oplus 2$ periodic states. One occurs before the first symmetry breaking bifurcation where the mode 2 appears, while the other occurs after the first symmetry breaking bifurcation and prior to the second. Chomaz *et al* [6] also reports a transient "chaotic" state analogous to the irregular flows seen by Früh & Read [15]. We have observed the irregular flow at a Reynolds number slightly higher than the $n = 4 \oplus 2 \oplus 3$ state, figures 4.25 and 4.26.

These irregular flows may be either quasi-periodic in the rotating frame or chaotic. Time series analysis of the data is required to determine and dimensionality of the dynamics and is beyond the scope of this thesis.

Thus, we provide numerical simulation for the full series of bifurcations between the $n = 4$ steady state and the $n = 3$ steady state. Figure 4.18 is a cartoon of the transitions between the steady, periodic, and irregular states.

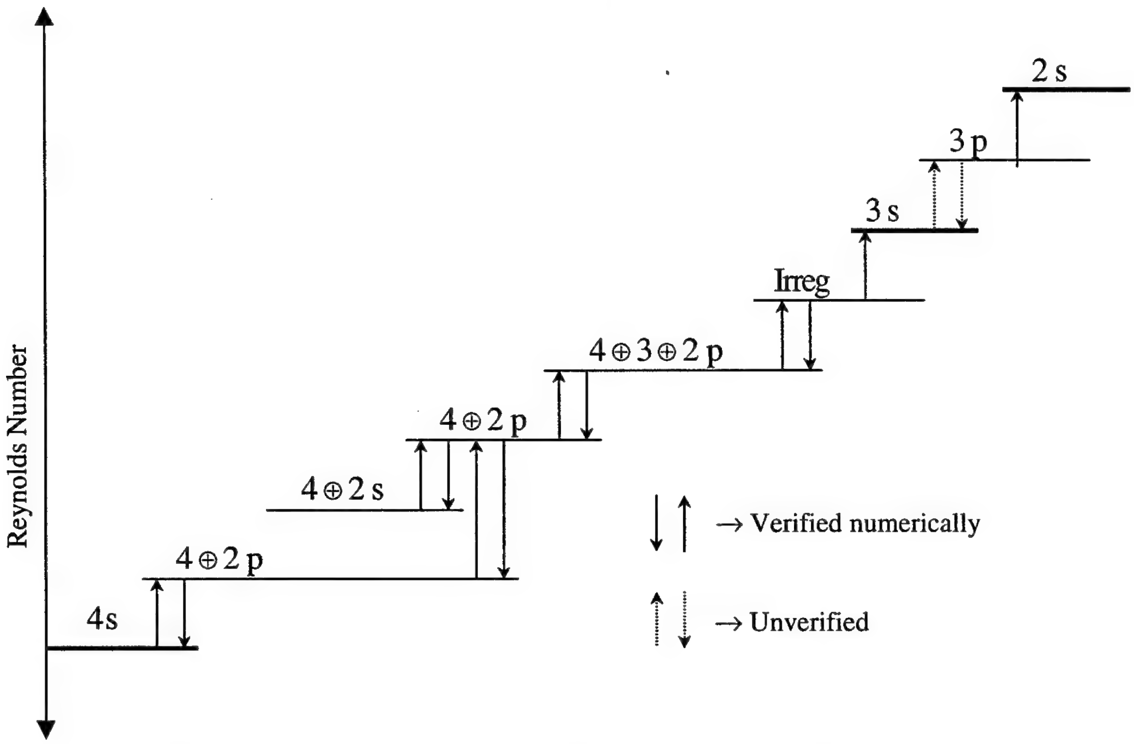

fig 4.18 These are the states surrounding the $4 \oplus 3 \oplus 2$ *periodic solution. The periodicity is time dependent with* s ⇒ steady *and* p ⇒ periodic.
Unverified results have been reported in other experiments and simulations.

The bold lines indicate levels at which hysteresis is observed e.g. once a steady or periodic $n = 3$ flow is established the symmetry breaking bifurcations between the $n = 4$ and $n = 3$ braids cannot be reversed by lowering the Reynolds number. The transitions consist of spatial and/or temporal symmetry breaking.

With the highly accurate spectral simulation additional investigations can be made into the bifurcations between the $n = 3$ and $n = 2 \oplus 1$ states. In order to isolate the bifurcations and associated states, the flow must be allowed to relax. All intermediate periodic states are bypassed if the flow does not relax for at least 20 cycles of the turn around time and some bifurcations require more than 200 cycles.

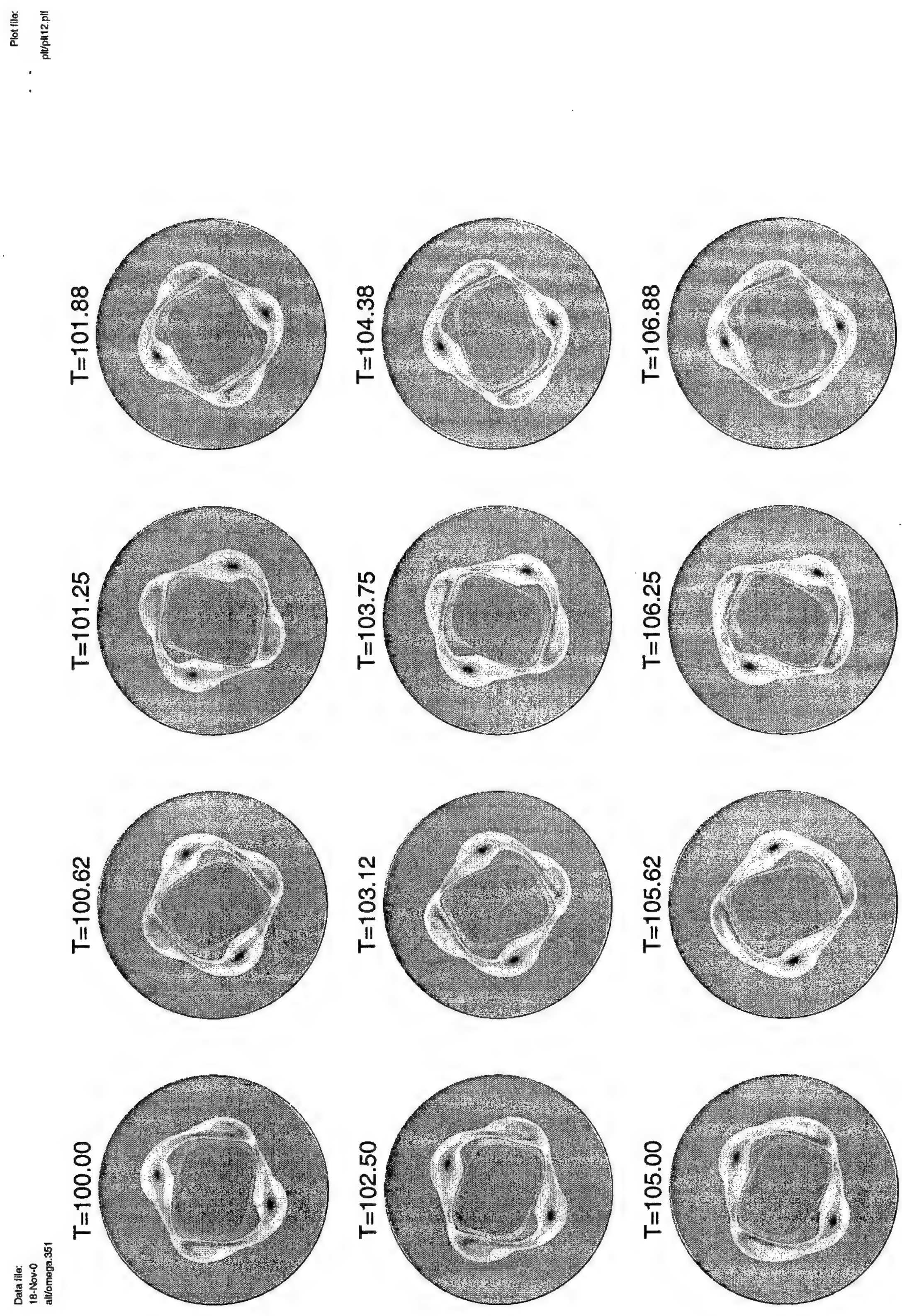

fig 4.19 $4 \oplus 2$ *periodic flow.*

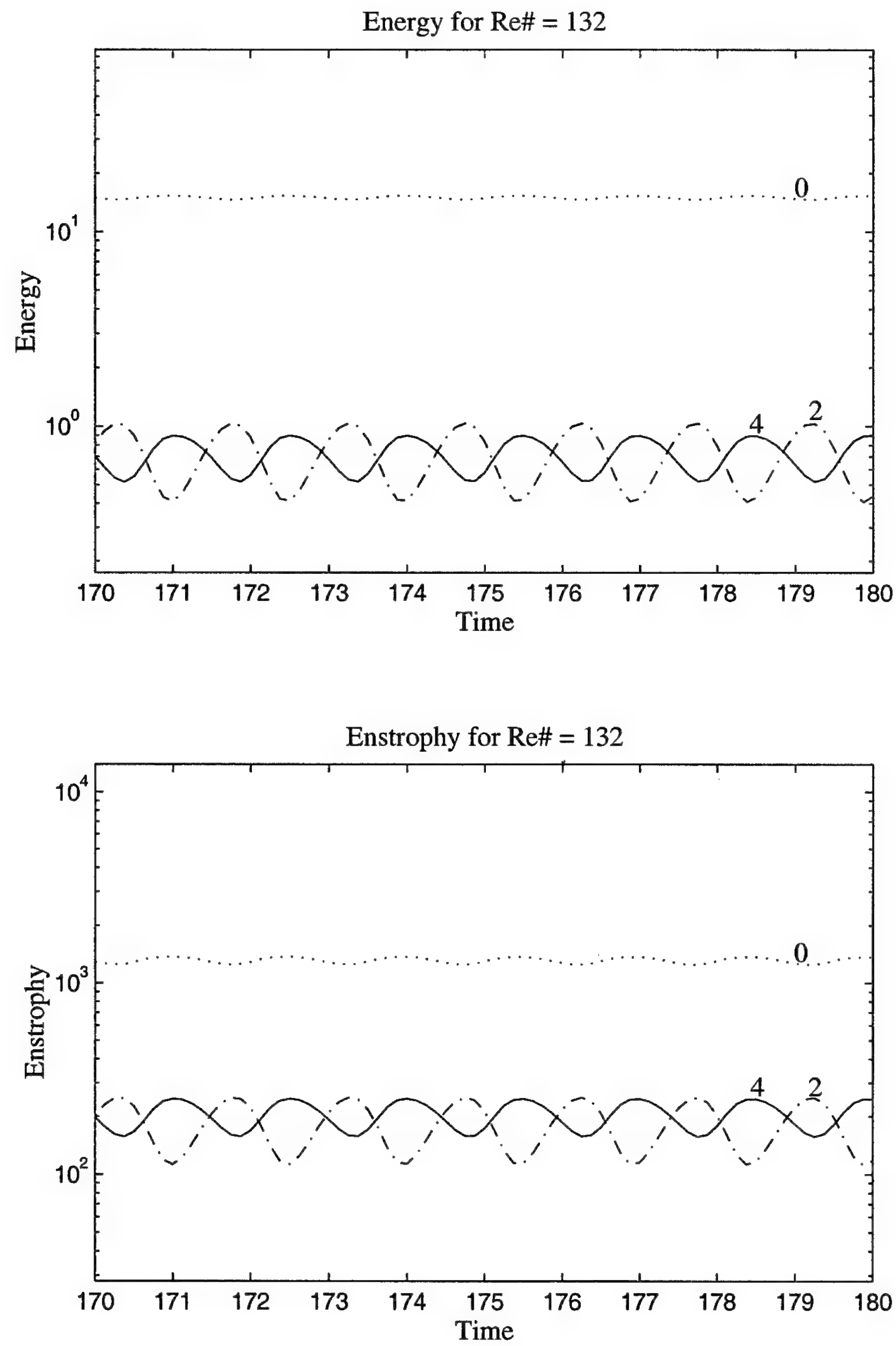

fig 4.20 Energy and enstrophy for the $4 \oplus 2$ *periodic state.*
The numbers correspond to Fourier modes.

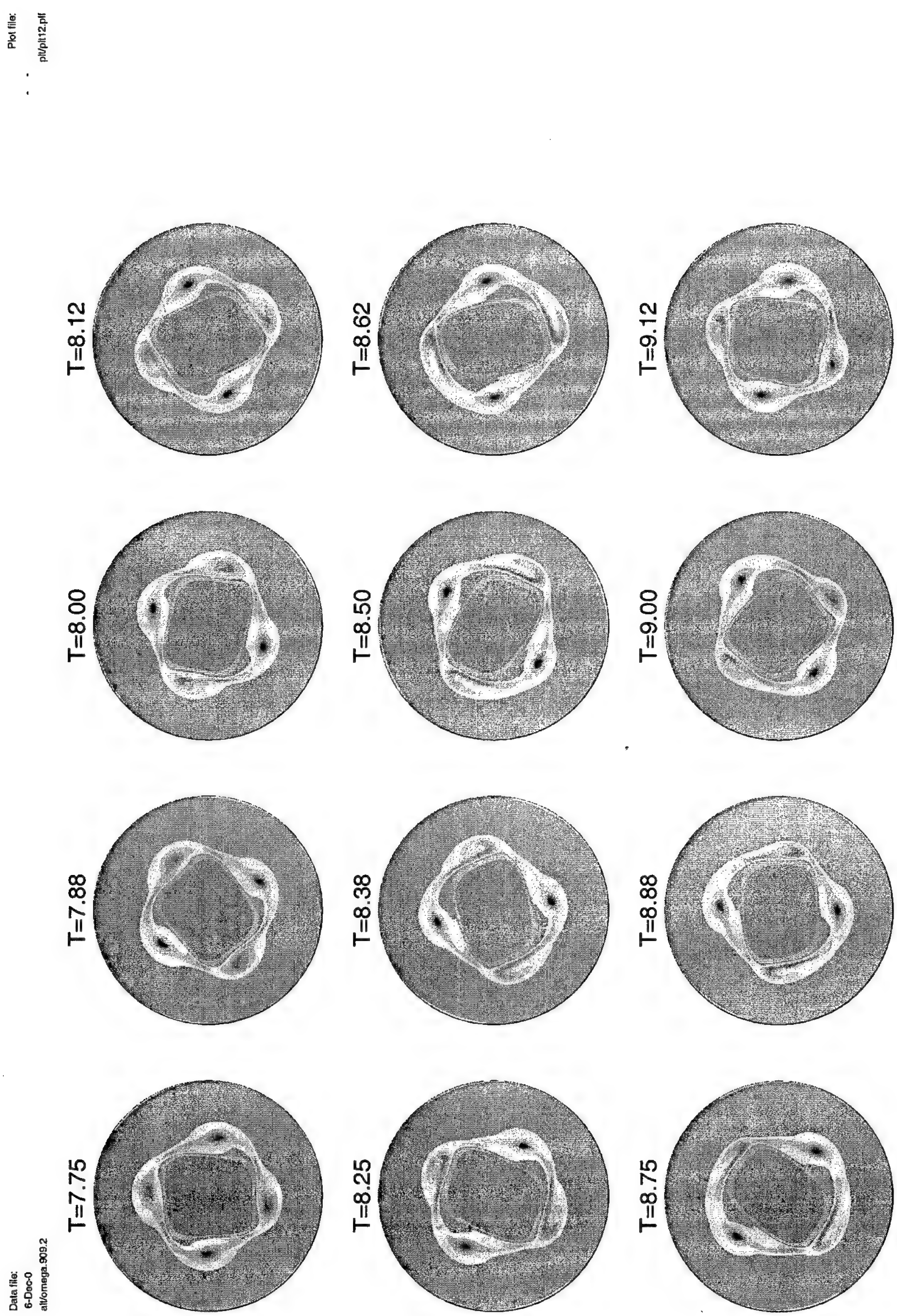

fig 4.21 $4 \oplus 3 \oplus 2$ *periodic flow.*

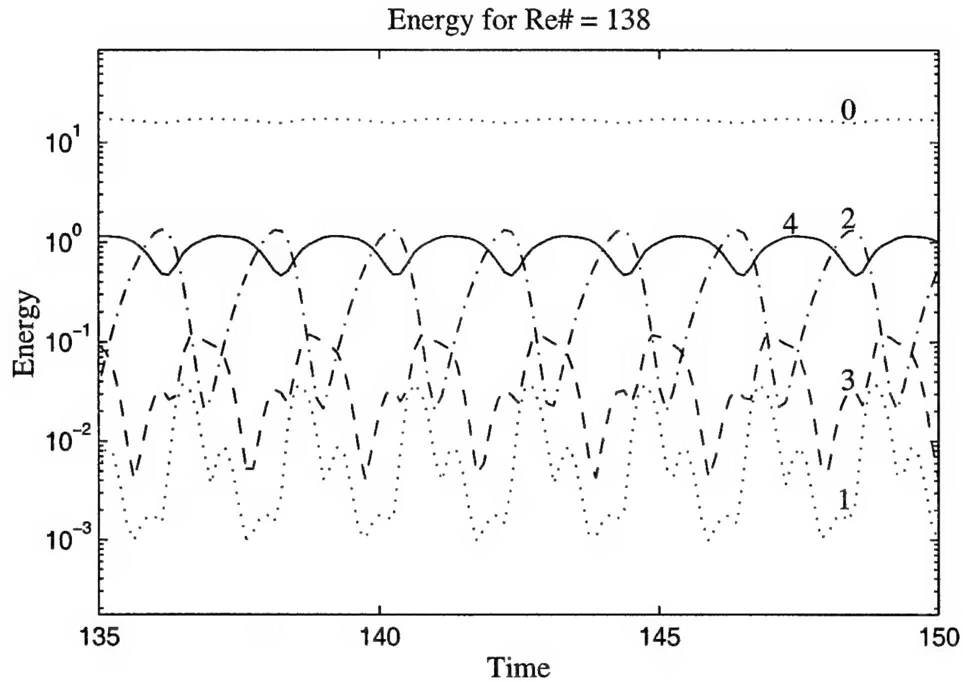

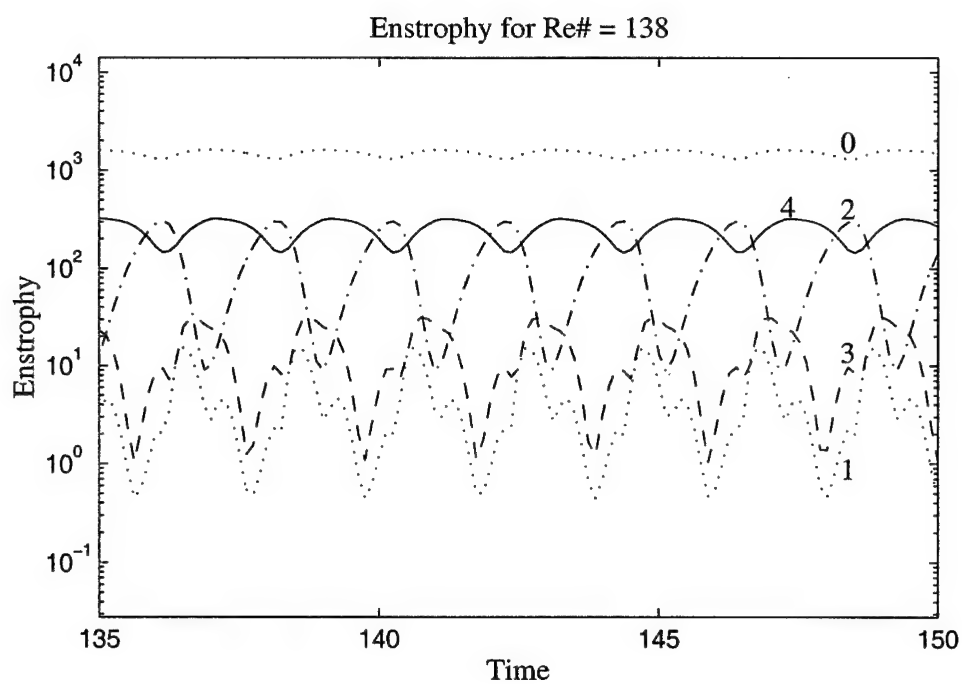

fig 4.22 Energy and enstrophy of the periodic $4 \oplus 3 \oplus 2$ state.
The numbers correspond to the Fourier modes.

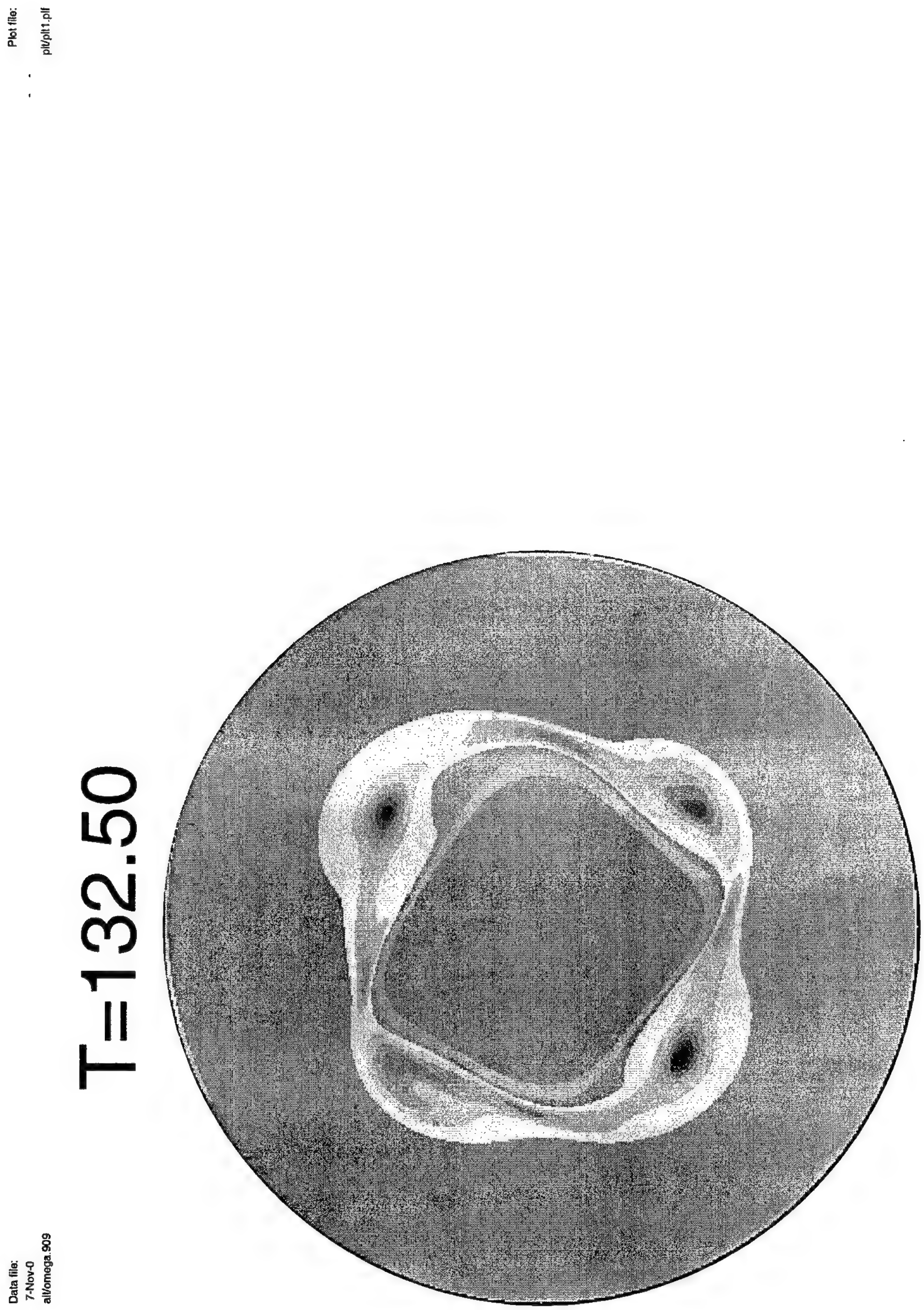

fig 4.23 Asymmetric flow resulting from the $4 \oplus 3 \oplus 2$ *periodic state.*

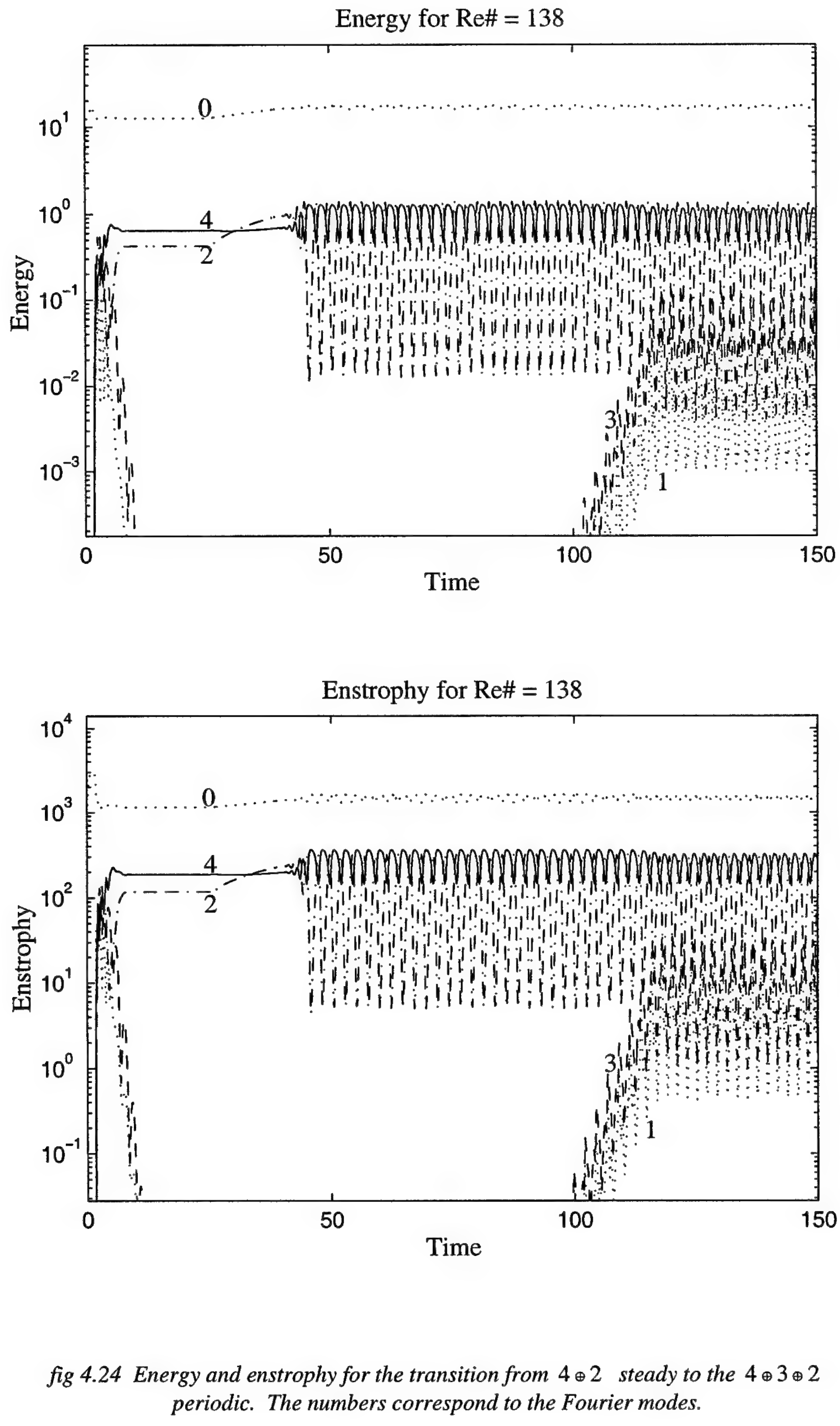

fig 4.24 Energy and enstrophy for the transition from $4 \oplus 2$ *steady to the* $4 \oplus 3 \oplus 2$ *periodic. The numbers correspond to the Fourier modes.*

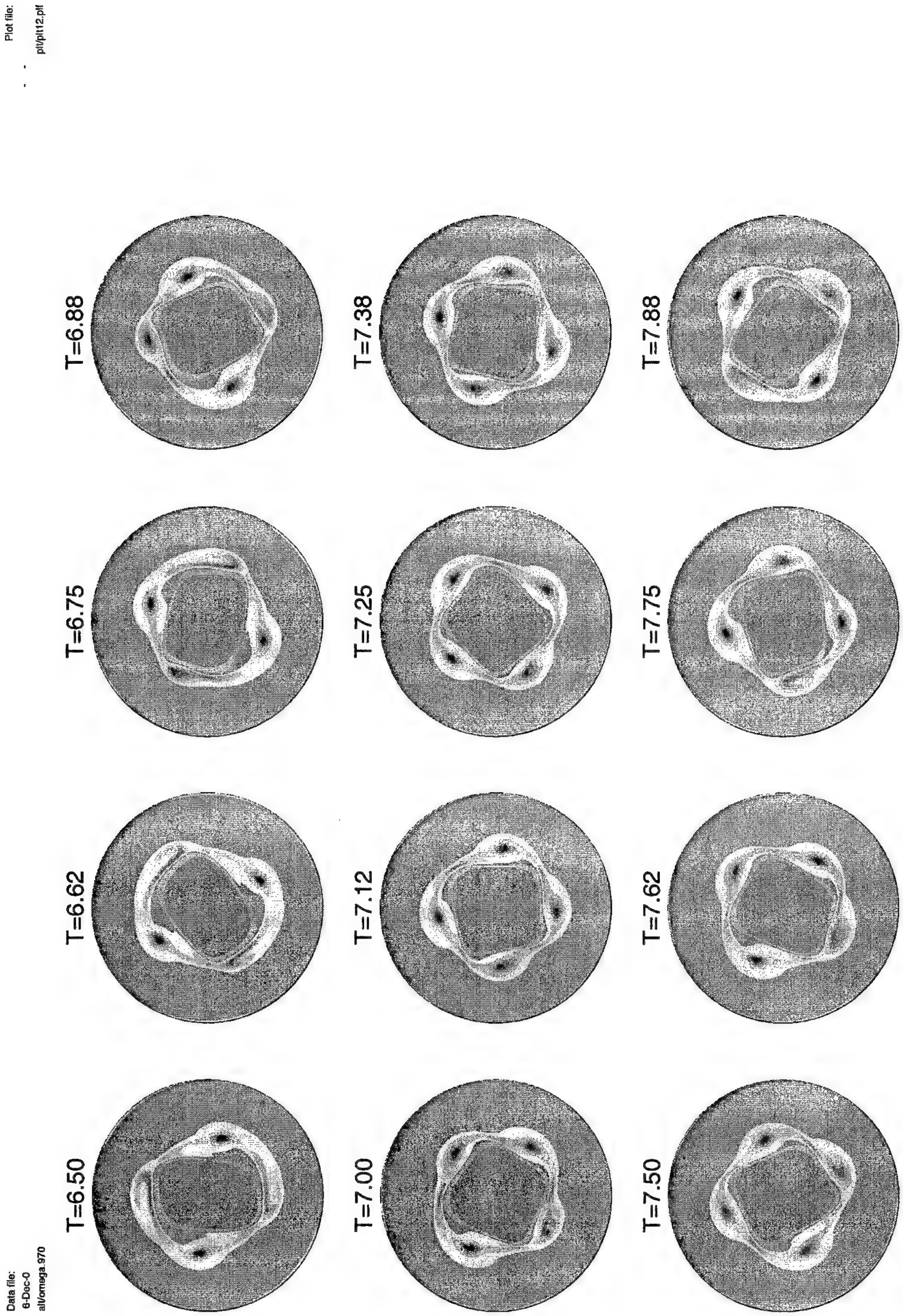

fig 4.25 Irregular flow after the $4 \oplus 3 \oplus 2$ *periodic state.*

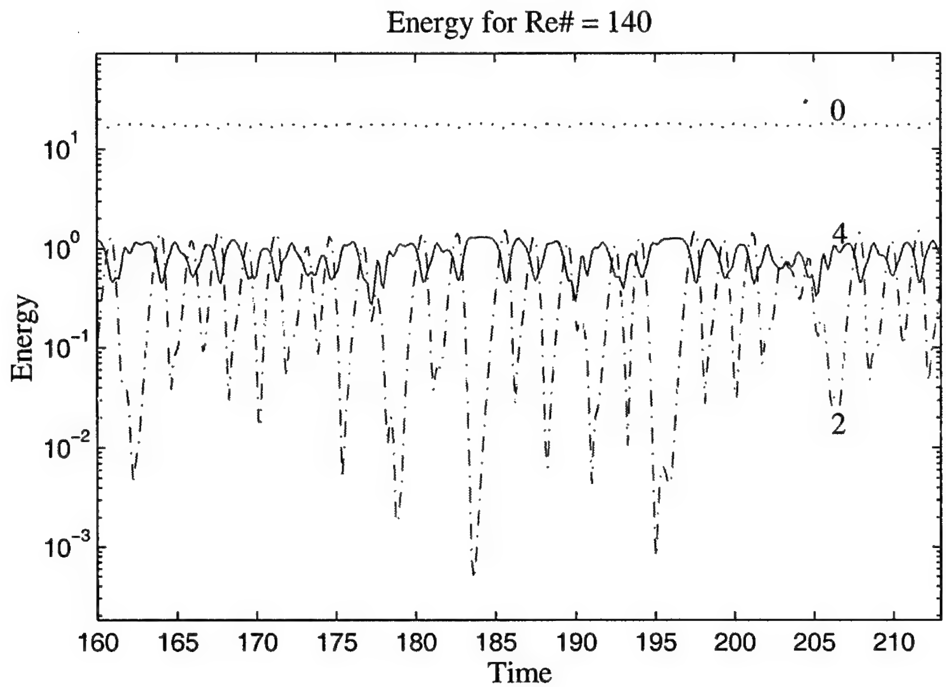

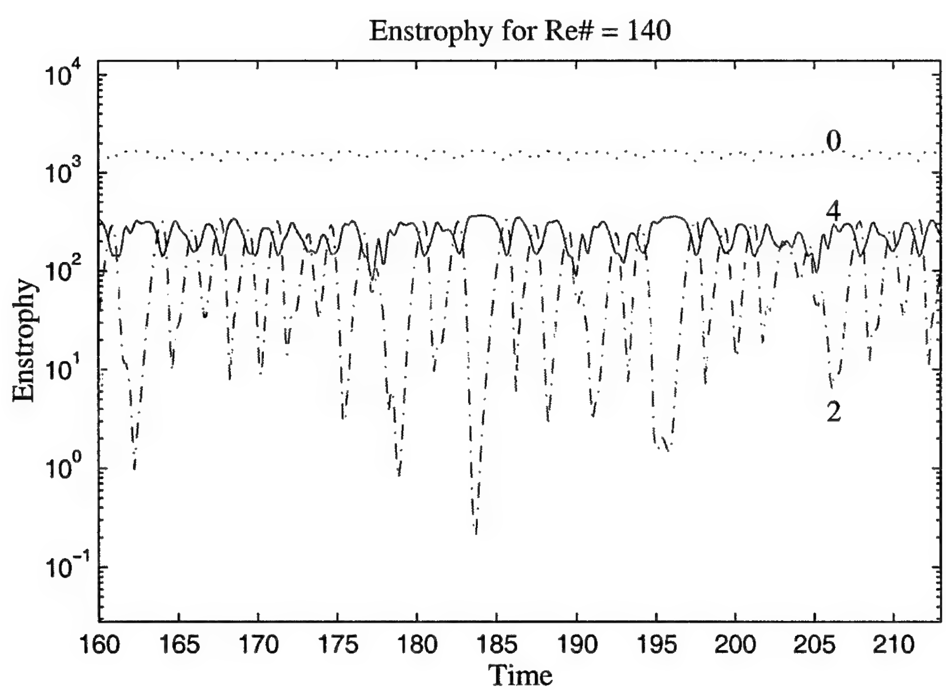

fig 4.26 Energy and enstrophy for the 2nd and 4th Fourier modes of the irregular flow.

APPENDIX A

Vector identities

A.1 $$\vec{a}\times\left(\vec{b}\times\vec{c}\right)=\left(\vec{a}\cdot\vec{c}\right)\vec{b}-\left(\vec{a}\cdot\vec{b}\right)\vec{c}$$

A.2 $$\nabla\left(\vec{a}\cdot\vec{b}\right)=\vec{a}\cdot\nabla\vec{b}+\vec{b}\cdot\nabla\vec{a}+\vec{a}\times\left(\nabla\times\vec{b}\right)+\vec{b}\times\left(\nabla\times\vec{a}\right)$$

A.3 $$\nabla^2\vec{a}=\nabla\left(\nabla\cdot\vec{a}\right)-\nabla\times\left(\nabla\times\vec{a}\right)$$

A.4 $$\nabla\times\left(a\vec{b}\right)=\nabla a\times\vec{b}+a\left(\nabla\times\vec{b}\right)$$

A.5 $$\nabla\cdot\left(a\vec{b}\right)=a\nabla\cdot\vec{b}+\vec{b}\cdot\nabla a$$

A.6 $$\nabla\times\left(\vec{a}\times\vec{b}\right)=\vec{b}\cdot\nabla\vec{a}-\vec{b}\left(\nabla\cdot\vec{a}\right)-\vec{a}\cdot\nabla\vec{b}+\vec{a}\left(\nabla\cdot\vec{b}\right)$$

A.7 $$\nabla\cdot\left(\vec{a}\times\vec{b}\right)=\vec{b}\cdot\left(\nabla\times\vec{a}\right)-\vec{a}\cdot\left(\nabla\times\vec{b}\right)$$

APPENDIX B

Conditioning of the problem

In general the linear Helmholtz equation has the form

B.1 $$\mathbf{A}\vec{\omega}^\circ = \vec{g}$$

where $\vec{\omega}^\circ$ is used to find the vorticity through the smoothing and postconditioning

B.2 $$\vec{\omega} = \mathbf{R}^j\mathbf{P}^2\vec{\omega}^\circ \text{ for } j = 1,2$$

To estimate the condition of the problem consider a perturbed linear system B.1 and a perturbed conversion B.2 giving

B.3 $$(\mathbf{A}+\delta\mathbf{A})\left(\vec{\omega}^\circ + \delta\vec{\omega}^\circ\right) = \vec{g} + \delta\vec{g}$$

B.4 $$\vec{\omega} + \delta\vec{\omega} = \left(\mathbf{R}^j + \delta\mathbf{R}^j\right)(\mathbf{P}+\delta\mathbf{P})\left(\vec{\omega}^\circ + \delta\vec{\omega}^\circ\right)$$

The conditioning for the problem is measured through the magnitude of the relative error in vorticity. This error compares the norm of the vorticity error to the norm of the vorticity.

For the first order approximation all quadratic error terms are eliminated. To obtain the condition number for the Helmholtz operator, start by solving B.3 for $\delta\vec{\omega}^\circ$ and $\vec{\omega}^\circ$, respectively

B.5 $$\delta\vec{\omega}^\circ = \mathbf{A}^{-1}\vec{g} + \mathbf{A}^{-1}\delta\vec{g} - \vec{\omega}^\circ - \mathbf{A}^{-1}\delta\mathbf{A}\vec{\omega}^\circ = \mathbf{A}^{-1}\delta\vec{g} - \mathbf{A}^{-1}\delta\mathbf{A}\vec{\omega}^\circ$$

B.6 $$\vec{\omega}^\circ = \mathbf{A}^{-1}(\vec{g} + \delta\vec{g}) - \delta\vec{\omega}^\circ$$

Assuming $\left\|\mathbf{A}^{-1}\right\|\left\|\delta\mathbf{A}\right\| < 1$, recursive application of B.6 into B.5 while eliminating higher order terms gives

B.7 $$\delta\vec{\omega}^\circ = \mathbf{A}^{-1}\delta\vec{g} + \left[\sum_{k=1}^{\infty}(-1)^k\left(\mathbf{A}^{-1}\delta\mathbf{A}\right)^k\right]\mathbf{A}^{-1}(\vec{g}+\delta\vec{g})$$

Now expand B.4 while subtracting the representation for vorticity, $\vec{\omega} = \mathbf{R}^j\mathbf{P}^2\vec{\omega}^\circ$, giving

$$\delta\vec{\omega} = \left(\mathbf{R}^j\delta\mathbf{P}^2 + \delta\mathbf{R}^j\mathbf{P}^2\right)\vec{\omega}^\circ + \left(\mathbf{R}^j\mathbf{P}^2 + \mathbf{R}^j\delta\mathbf{P}^2 + \delta\mathbf{R}^j\mathbf{P}^2\right)\delta\vec{\omega}^\circ$$

Substituting B.7 into this equation gives

B.8
$$\delta\vec{\varpi} = \left(\mathbf{R}^j\delta\mathbf{P}^2 + \delta\mathbf{R}^j\mathbf{P}^2\right)\vec{\varpi}^\circ + \left(\mathbf{R}^j\mathbf{P}^2 + \mathbf{R}^j\delta\mathbf{P}^2 + \delta\mathbf{R}^j\mathbf{P}^2\right)\mathbf{A}^{-1}\delta\vec{g} +$$
$$\left(\mathbf{R}^j\mathbf{P}^2 + \mathbf{R}^j\delta\mathbf{P}^2 + \delta\mathbf{R}^j\mathbf{P}^2\right)\left[\sum_{k=1}^{\infty}(-1)^k\left(\mathbf{A}^{-1}\delta\mathbf{A}\right)^k\right]\mathbf{A}^{-1}\left(\vec{g}+\delta\vec{g}\right)$$

The summation is transformed in two steps enabling an efficient norm. Note all elements in the sum have a $\mathbf{A}^{-1}$ product on the left and a $\delta\mathbf{A}$ product on the right. Factoring out these common terms gives

B.9
$$\sum_{k=1}^{\infty}(-1)^k\left(\mathbf{A}^{-1}\delta\mathbf{A}\right)^k = \mathbf{A}^{-1}\left[\sum_{k=1}^{\infty}(-1)^k\left(\delta\mathbf{A}\mathbf{A}^{-1}\right)^{k-1}\right]\delta\mathbf{A}$$

The sum on the right hand side is now in geometric form. When a norm is applied to the geometric sum an inequality follows

$$\left\|\sum_{k=1}^{\infty}(-1)^k\left(\delta\mathbf{A}\mathbf{A}^{-1}\right)^{k-1}\right\| = \left\|\frac{1}{1-\delta\mathbf{A}\mathbf{A}^{-1}}\right\| \le \frac{1}{1-\|\delta\mathbf{A}\|\|\mathbf{A}^{-1}\|}$$

When B.9 replaces the sum in B.8 and a norm is taken from both sides, the result is an inequality of the form

B.10
$$\begin{aligned}\|\delta\vec{\varpi}\| \le{}& \|\mathbf{R}^j\|\|\delta\mathbf{P}^2\|\|\vec{\varpi}^\circ\| + \|\delta\mathbf{R}^j\|\|\mathbf{P}^2\|\|\vec{\varpi}^\circ\| + \|\mathbf{R}^j\mathbf{P}^2\mathbf{A}^{-1}\|\|\delta\vec{g}\| + \\ & \|\mathbf{R}^j\|\|\delta\mathbf{P}^2\|\|\mathbf{A}^{-1}\|\|\delta\vec{g}\| + \|\delta\mathbf{R}\|^j\|\mathbf{P}^2\|\|\mathbf{A}^{-1}\|\|\delta\vec{g}\| + \\ & \left(\|\mathbf{R}^j\mathbf{P}^2\mathbf{A}^{-1}\| + \|\mathbf{R}^j\|\|\delta\mathbf{P}^2\|\|\mathbf{A}^{-1}\| + \|\delta\mathbf{R}^j\|\|\mathbf{P}^2\|\|\mathbf{A}^{-1}\|\right)* \\ & \|\Sigma\|\|\delta\mathbf{A}\|\left(\|\vec{\varpi}^\circ\| + \|\mathbf{A}^{-1}\|\|\delta\vec{g}\|\right)\end{aligned}$$

where $\|\Sigma\| \equiv \frac{1}{1-\|\delta\mathbf{A}\|\|\mathbf{A}^{-1}\|}$. At this point we introduce a notation to simplify the above estimate. The Chi function is the ratio of the norm of the error to the norm of the operator e.g. for an operator ξ the Chi function is defined as

$$\chi(\xi) = \frac{\|\delta\xi\|}{\|\xi\|}$$

Applying the Chi function while dividing by $\|\vec{\varpi}^\circ\|$ transforms B.10 into

$$\frac{\|\delta\vec{\omega}\|}{\|\vec{\omega}^{\circ}\|} \le \|\mathbf{R}^{j}\|\|\mathbf{P}^{2}\|\left[\chi(\mathbf{P}^{2})+\chi(\mathbf{R}^{j})\right]+\frac{\|\delta\vec{g}\|}{\|\vec{\omega}^{\circ}\|}\|\mathbf{R}^{j}\mathbf{P}^{2}\mathbf{A}^{-1}\|+$$

B.11

$$\frac{\|\delta\vec{g}\|}{\|\vec{\omega}^{\circ}\|}\|\mathbf{A}^{-1}\|\|\mathbf{R}^{j}\|\|\mathbf{P}^{2}\|\left[\chi(\mathbf{P}^{2})+\chi(\mathbf{R}^{j})\right]+$$

$$\|\Sigma\|\|\delta\mathbf{A}\|\|\mathbf{R}^{j}\mathbf{P}^{2}\mathbf{A}^{-1}\|\left(1+\|\mathbf{A}^{-1}\|\frac{\|\delta\vec{g}\|}{\|\vec{\omega}^{\circ}\|}\right)+$$

$$\|\Sigma\|\|\delta\mathbf{A}\|\|\mathbf{A}^{-1}\|\|\mathbf{R}^{j}\|\|\mathbf{P}^{2}\|\left[\chi(\mathbf{P}^{2})+\chi(\mathbf{R}^{j})\right]\left(1+\|\mathbf{A}^{-1}\|\frac{\|\delta\vec{g}\|}{\|\vec{\omega}^{\circ}\|}\right)$$

Further simplification comes through the norm inequality based on B.1

$$\frac{1}{\|\vec{\omega}^{\circ}\|} \le \frac{\|\mathbf{A}\|}{\|\vec{g}\|}$$

and an additional definition, the condition number of $\mathbf{A}$,

$$C_{\mathbf{A}} = \|\mathbf{A}\|\|\mathbf{A}^{-1}\|$$

Rewriting B.11 with these considerations gives

$$\frac{\|\delta\vec{\omega}\|}{\|\vec{\omega}^{\circ}\|} \le \|\mathbf{R}^{j}\|\|\mathbf{P}^{2}\|\left[\chi(\mathbf{P}^{2})+\chi(\mathbf{R}^{j})\right]+\|\mathbf{A}\|\|\mathbf{R}^{j}\mathbf{P}^{2}\mathbf{A}^{-1}\|\chi(\vec{g})+$$

$$C_{\mathbf{A}}\|\mathbf{R}^{j}\|\|\mathbf{P}^{2}\|\chi(\vec{g})\left[\chi(\mathbf{P}^{2})+\chi(\mathbf{R}^{j})\right]+$$

$$\|\mathbf{A}\|\|\Sigma\|\chi(\mathbf{A})\|\mathbf{R}^{j}\mathbf{P}^{2}\mathbf{A}^{-1}\|\left[1+C_{\mathbf{A}}\chi(\vec{g})\right]+$$

$$C_{\mathbf{A}}\|\mathbf{R}^{j}\|\|\mathbf{P}^{2}\|\|\Sigma\|\chi(\mathbf{A})\left[\chi(\mathbf{P}^{2})+\chi(\mathbf{R}^{j})\right]\left[1+C_{\mathbf{A}}\chi(\vec{g})\right]$$

For the final estimate remove the high order terms and neglect $\chi(\mathbf{R}^{j})$ and $\chi(\mathbf{P}^{2})$. Since the matrices $\mathbf{R}^{j}$ and $\mathbf{P}^{2}$ have error controlled by the truncation of the Chebyshev expansion, the errors are exponentially small when compared to those of the SBDF scheme found in $\mathbf{A}$. These simplifications lead to

B.12

$$\frac{\|\delta\vec{\omega}\|}{\|\vec{\omega}^{\circ}\|} \le \|\mathbf{A}\|\|\mathbf{R}^{j}\mathbf{P}^{2}\mathbf{A}^{-1}\|\chi(\vec{g})+\|\mathbf{A}\|\|\Sigma\|\chi(\mathbf{A})\|\mathbf{R}^{j}\mathbf{P}^{2}\mathbf{A}^{-1}\|=$$

$$\|\mathbf{A}\|\|\mathbf{R}^{j}\mathbf{P}^{2}\mathbf{A}^{-1}\|\left[\chi(\vec{g})+\|\Sigma\|\chi(\mathbf{A})\right]$$

The ratio of norms between the calculated value, $\vec{\omega}^{\circ}$, and the vorticity forms the inequality

$$\frac{1}{\|\mathbf{R}^{j}\|\|\mathbf{P}^{2}\|} \le \frac{\|\vec{\omega}^{\circ}\|}{\|\vec{\omega}\|} \le \frac{1}{\alpha}$$

and this inequality applied to B.12 giving the final form of the condition number bound

$$\frac{\|\delta\vec{\omega}\|}{\|\vec{\omega}\|} \le \frac{\|\mathbf{A}\|}{\alpha}\left\|\mathbf{R}^j\mathbf{P}^2\mathbf{A}^{-1}\right\|\left[\chi(\vec{g}) + \|\Sigma\|\chi(\mathbf{A})\right] \le \frac{\|\mathbf{A}\|}{\alpha}\left\|\mathbf{R}^j\mathbf{P}^2\mathbf{A}^{-1}\right\|\left[\chi(\vec{g}) + 2\chi(\mathbf{A})\right]$$

This bound is nearly the product of the condition number of $\mathbf{A}$ with the relative error in the problem.

APPENDIX C

Chebyshev recurrence relations

The Chebyshev polynomials provide an orthogonal basis for fast computation in numerical simulation. In addition to possessing a fast transform, Fourier Cosine Transform (FCT), these polynomials relate through several recurrence relations. The Chebyshev polynomials are defined by the relation

C.1 $$T_m(r) = 2rT_{m-1}(r) - T_{m-2}(r)$$

where $T_0 = 1$ and $T_1(x) = x$. An alternative identity for the polynomials relates to their cosine transform

C.2 $$T_m(\cos\theta) = \cos m\theta$$

Considering the Chebyshev polynomials within the range $-1 \le r \le 1$ provides additional relations. At the boundaries the polynomials are unitary

$$T_m(1) = 1$$

$$T_m(-1) = (-1)^m$$

and at the middle of the interval, $r = 0$, the behavior is

$$T_m(0) = \begin{cases} 0 & m \text{ odd} \\ (-1)^k & m = 2k \end{cases}$$

The zeros of the Chebyshev polynomials are distinct, and $T_m(r)$ has exactly n zeros in $-1 \le r \le 1$. The form for the zeros is

$$T_m(r_k) = 0 \text{ for } r_k = \cos\left(\tfrac{2k+1}{2m}\pi\right)$$

where $k = 0,1,\ldots,n-1$.

Multiplying two Chebyshev polynomials produces a relation through C.2. Consider the product of polynomials

$$T_n(\cos\theta)T_m(\cos\theta) = \cos n\theta \cos m\theta$$

and using

$$\cos n\theta \cos m\theta = \tfrac{1}{2}\left[\cos(n\theta + m\theta) + \cos(n\theta - m\theta)\right]$$

gives the relation

$$T_n T_m = \tfrac{1}{2}\left(T_{n+m} + T_{|n-m|}\right)$$

The product relation is used to derive the Chebyshev convolution in appendix E.

Differentiation of a Chebyshev polynomials also produces a recurrence. The derivative of C.1 with respect to r gives

$$T_m'(r) = 2rT_{m-1}'(r) + 2T_{m-1} - T_{m-2}'(r)$$

recursive substitutions of this form while shifting the index give

$$T_m' = m\left(2T_{m-1} + \tfrac{T_{m-2}'}{m-2}\right)$$

where $T_1' = T_0$ and $T_0' = 0$. The differentiation recurrence produces the Chebyshev differentiation matrix.

APPENDIX D

Chebyshev matrices

Multiplication and differentiation by the radius, r, appear throughout the Navier-Stokes equations. When the Fourier-Chebyshev expansions are truncated the problem can be solved using matrix-vector representation. Flow parameters are represented by their Fourier-Chebyshev coefficients. Since the problem uncouples through the Fourier modes, Chebyshev coefficients for a specific Fourier mode are rendered in a single vector

$$\vec{\zeta}_n(r) = \begin{bmatrix} \zeta_{n,0} & \zeta_{n,1} & \zeta_{n,2} & \cdots & \zeta_{n,M} \end{bmatrix}^{\mathrm{T}}$$

where $\vec{\zeta}_n$ is the vector of Chebyshev coefficients for Fourier mode n. The required linear operators in the Chebyshev basis are represented as matrices. Multiplication by r is nothing more than convolution with the coefficient vector

$$r = \begin{bmatrix} 0 & 1 & 0 & \cdots & 0 \end{bmatrix}^{\mathrm{T}}$$

Chebyshev convolution matrices are discussed in appendix E. The convolution matrix for r is

$$\mathbf{R} = \begin{bmatrix} 0 & \frac{1}{2} & 0 & 0 & 0 \\ 1 & 0 & \frac{1}{2} & 0 & 0 \\ 0 & \frac{1}{2} & 0 & \ddots & 0 \\ 0 & 0 & \ddots & \ddots & \frac{1}{2} \\ 0 & 0 & 0 & \frac{1}{2} & 0 \end{bmatrix}$$

Differentiation by r derives from the recurrence relation

$$T'_m = m\left(2T_{m-1} + \tfrac{T'_{m-2}}{m-2}\right)$$

where $T'_1 = T_0$ and $T'_0 = 0$. Expanding the recurrence and truncating at mode M gives

$$\mathbf{D} = \begin{bmatrix} 0 & 1 & 0 & 3 & 0 & 5 & \cdots & M \\ 0 & 0 & 4 & 0 & 8 & 0 & \ddots & 0 \\ 0 & 0 & 0 & 6 & 0 & 10 & \ddots & 2M \\ 0 & 0 & 0 & 0 & 8 & 0 & \ddots & 0 \\ 0 & 0 & 0 & 0 & 0 & 10 & \ddots & 2M \\ 0 & 0 & 0 & 0 & 0 & 0 & \ddots & 0 \\ 0 & 0 & 0 & 0 & 0 & 0 & \ddots & 2M \\ 0 & 0 & 0 & 0 & 0 & 0 & 0 & 0 \end{bmatrix}$$

Both $\mathbf{R}$ and $\mathbf{D}$ apply to a single Chebyshev coefficient vector. When the full vector form is required as with the secondary stability analysis, composition of matrices is required. The full vector form of the flow parameters follows

$$\vec{\zeta}(r,\theta)=\begin{bmatrix}\vec{\zeta}_0^c(r)\\ \vec{\zeta}_1^c(r)\\ \vdots\\ \vec{\zeta}_{\frac{N}{2}}^c(r)\\ 0\\ \vec{\zeta}_1^s(r)\\ \vdots\\ \vec{\zeta}_{\frac{N}{2}}^s(r)\end{bmatrix}$$

where $\vec{\zeta}(r,\theta)$ is either vorticity, $\vec{\omega}$, or stream function, $\vec{\psi}$, and $\vec{\zeta}_j^c$ / $\vec{\zeta}_j^s$ are the Chebyshev coefficient vectors for the j^{th} Fourier mode, cosine and sine, respectively. Since multiplication and differentiation by r impact only the Chebyshev coefficients, the matrix providing multiplication by r for the long vector problem is

$$\hat{\mathbf{R}}=\mathbf{I}_{\frac{N}{2}+1}\otimes\mathbf{R}=\begin{bmatrix}\mathbf{R} & 0 & \cdots & 0\\ 0 & \mathbf{R} & & \vdots\\ \vdots & & \ddots & 0\\ 0 & \cdots & 0 & \mathbf{R}\end{bmatrix}$$

Each $\mathbf{R}$ matrix has size $(M+1)\times(M+1)$, and there are $N+2$ $\mathbf{R}$ matrices along the diagonal. Similarly differentiation by r produces the matrix

$$\hat{\mathbf{D}}=\mathbf{I}_{\frac{N}{2}+1}\otimes\mathbf{D}=\begin{bmatrix}\mathbf{D} & 0 & \cdots & 0\\ 0 & \mathbf{D} & & \vdots\\ \vdots & & \ddots & 0\\ 0 & \cdots & 0 & \mathbf{D}\end{bmatrix}$$

Each $\mathbf{D}$ matrix has size $(M+1)\times(M+1)$, and there are $N+2$ $\mathbf{D}$ matrices along the diagonal. In addition to these basic operations within the Fourier-Chebyshev expansion, $\hat{\mathbf{R}}\equiv r$ and $\hat{\mathbf{D}}\equiv\partial_r$, Fourier modes require differentiation by θ. In the long vector environment a new matrix is defined for this purpose, $\hat{\mathbf{Q}}\equiv\partial_\theta$. The $\hat{\mathbf{Q}}$ matrix is formed by considering the differentiation of sine and cosine functions. Here the impact is strictly

upon the Fourier modes leaving the Chebyshev expansions unchanged. For differentiation by θ

$$\hat{\mathbf{Q}} = \begin{bmatrix} 0 & \mathbf{I}_{\frac{N}{2}+1} \otimes -n\mathbf{I}_{M+1} \\ \mathbf{I}_{\frac{N}{2}+1} \otimes -n\mathbf{I}_{M+1} & 0 \end{bmatrix} =$$

$$\begin{bmatrix} 0 & \cdots & \cdots & \cdots & 0 & 0 & \cdots & \cdots & \cdots & 0 \\ \vdots & \ddots & & & \vdots & \vdots & \mathbf{I} & & & \vdots \\ \vdots & & \ddots & & \vdots & \vdots & & 2\mathbf{I} & & \vdots \\ \vdots & & & \ddots & \vdots & \vdots & & & \ddots & 0 \\ 0 & \cdots & \cdots & \cdots & 0 & 0 & \cdots & \cdots & 0 & \frac{N}{2}\mathbf{I} \\ 0 & \cdots & \cdots & \cdots & 0 & 0 & \cdots & \cdots & \cdots & 0 \\ \vdots & -\mathbf{I} & & & \vdots & \vdots & \ddots & & & \vdots \\ \vdots & & -2\mathbf{I} & & \vdots & \vdots & & \ddots & & \vdots \\ \vdots & & & \ddots & 0 & \vdots & & & \ddots & \vdots \\ 0 & \cdots & \cdots & 0 & -\frac{N}{2}\mathbf{I} & 0 & \cdots & \cdots & \cdots & 0 \end{bmatrix}$$

where $n-1$ equates to the row of $\mathbf{I}_{\frac{N}{2}+1}$.

APPENDIX E

Chebyshev convolution matrix

The Chebyshev convolution matrix is used with the stability analysis. The convolution matrix is built using the Chebyshev multiplication recurrence relation

$$T_n T_m = \tfrac{1}{2}\left(T_{n+m} + T_{|n-m|}\right)$$

Additional notation is now introduced to provide a matrix-vector representation for the Chebyshev polynomials. After the expansions are truncated, every polynomial, T_j, can be written as a matrix, $\mathbf{T}_j$, which is defined as:

$$\mathbf{T}_j \equiv \begin{bmatrix} 0 & \cdots & 0 & \frac{1}{2} & 0 & \cdots & \cdots & 0 \\ \vdots & & \iddots & 0 & \frac{1}{2} & 0 & & \vdots \\ 0 & \frac{1}{2} & \iddots & & 0 & \frac{1}{2} & \ddots & \vdots \\ 1 & 0 & & \iddots & & 0 & \ddots & 0 \\ 0 & \frac{1}{2} & 0 & & \iddots & & \ddots & \frac{1}{2} \\ \vdots & 0 & \frac{1}{2} & 0 & & & & 0 \\ \vdots & & \ddots & \ddots & \ddots & & \iddots & \vdots \\ 0 & \cdots & \cdots & 0 & \frac{1}{2} & 0 & \cdots & 0 \end{bmatrix} \begin{array}{l} \\ \\ \\ \leftarrow j^{\text{th}}+1 \text{ row} \\ \\ \\ \\ \\ \end{array}$$

Here the convolution of two Chebyshev vectors is done only once so a computationally expensive matrix-vector multiplication is used. In general the convolution of two Chebyshev vectors $\vec{g}$ and $\vec{h}$ is accomplished in the following manner

$$\vec{g} \underset{c}{*} \vec{h} = \sum_{j=0}^{M} g_j \mathbf{T}_j \vec{h}$$

where each $\mathbf{T}_j \vec{h}$ is a matrix vector multiplication, and g_j is the coefficient for the j^{th} Chebyshev polynomial matrix, $\mathbf{T}_j$.

An example for our problem: let

$$\partial_r \vec{\omega}_{n,0} = \begin{bmatrix} \delta_{n,0} & \delta_{n,1} & \delta_{n,2} & \cdots & \delta_{n,M} \end{bmatrix}^{\mathrm{T}}$$

be the coefficient vector then the Chebyshev convolution matrix for $\partial_r \vec{\omega}_{n,0}$ is given by the following matrix

$$\overline{\partial_r \vec{\omega}_{n,0}} = \delta_{n,0}\mathbf{T}_0 + \delta_{n,1}\mathbf{T}_1 + \cdots + \delta_{n,M}\mathbf{T}_M$$

Note due to the non negative entries along the positive slope diagonal in each $\mathbf{T}_j$ matrix, the representation $\overline{\partial_r \bar{\omega}_{n,0}} = \sum_{j=0}^{M} \delta_{n,j} \mathbf{T}_j$ is only accurate for the $0 \to \frac{M}{2}$ Chebyshev modes. Convolution matrices created using $0 \to M$ modes and larger than $\left(\frac{M}{2}+1\right) \times \left(\frac{M}{2}+1\right)$ are missing meaningful data contributed by the $M+1$ and higher modes. Thus an M mode accurate Chebyshev convolution matrix requires $2M$ modes of data within the coefficient vector.

APPENDIX F

Fourier convolution matrix

As with the Chebyshev basis, the Fourier convolution of two functions generates linear operator by representing a vector of Fourier coefficients as an equivalent matrix. The convolution of two vectors within the Fourier trigonometric basis is more easily seen by converting the convolution represented in the exponential basis. Therefore, the Fourier convolution is initially derived for an exponential basis.

The Fourier convolution matrix resulting from an exponential basis rests upon the product rule for exponential expressions. Consider two expansions represented by exponential bases

$$c = \sum_{n=-\frac{N}{2}}^{\frac{N}{2}} c_n e^{in\theta}$$

$$\gamma = \sum_{n=-\frac{N}{2}}^{\frac{N}{2}} \gamma_n e^{in\theta}$$

The product of these two functions, $p = c\gamma$, can be represented within the same exponential basis

F.1 $$p = \sum_{n=-\frac{N}{2}}^{\frac{N}{2}} p_n e^{in\theta} = \left(\sum_{n=-\frac{N}{2}}^{\frac{N}{2}} c_n e^{in\theta}\right)\left(\sum_{n=-\frac{N}{2}}^{\frac{N}{2}} \gamma_n e^{in\theta}\right).$$

Every coefficient, p_n, is a sum of coefficient products e.g.

$$p_0 = c_{-\frac{N}{2}}\gamma_{\frac{N}{2}} + c_{-\frac{N}{2}+1}\gamma_{\frac{N}{2}-1} + \cdots + c_0\gamma_0 + \cdots + c_{\frac{N}{2}-1}\gamma_{-\frac{N}{2}+1} + c_{\frac{N}{2}}\gamma_{-\frac{N}{2}}$$

Using matrix-vector representation all of the functions are written as vectors containing their respective coefficients, $\vec{p}$, $\vec{c}$, and $\vec{\gamma}$. The functions c and γ in vector form

$$\vec{c} = \begin{bmatrix} c_{-\frac{N}{2}} & c_{1-\frac{N}{2}} & \cdots & c_{\frac{N}{2}-1} & c_{\frac{N}{2}} \end{bmatrix}^{\mathrm{T}}$$

$$\vec{\gamma} = \begin{bmatrix} \gamma_{-\frac{N}{2}} & \gamma_{1-\frac{N}{2}} & \cdots & \gamma_{\frac{N}{2}-1} & \gamma_{\frac{N}{2}} \end{bmatrix}^{\mathrm{T}}$$

lead to the following convolution matrix and product

$$\begin{bmatrix} c_0 & c_{-1} & c_{-2} & \cdots & c_{-\frac{N}{2}} & 0 & \cdots & \cdots & 0 \\ c_1 & c_0 & c_{-1} & \cdots & c_{-\frac{N}{2}+1} & c_{-\frac{N}{2}} & 0 & \cdots & 0 \\ \vdots & & \ddots & & & & \ddots & \ddots & \vdots \\ c_{\frac{N}{2}-1} & \cdots & \cdots & c_0 & \cdots & \cdots & \cdots & c_{-\frac{N}{2}} & 0 \\ c_{\frac{N}{2}} & c_{\frac{N}{2}-1} & \cdots & c_1 & c_0 & c_{-1} & \cdots & c_{-\frac{N}{2}+1} & c_{-\frac{N}{2}} \\ 0 & c_{\frac{N}{2}} & \cdots & \cdots & \cdots & c_0 & \cdots & \cdots & c_{-\frac{N}{2}+1} \\ \vdots & \ddots & \ddots & & & & \ddots & & \vdots \\ 0 & \cdots & 0 & c_{\frac{N}{2}} & c_{\frac{N}{2}-1} & \cdots & c_1 & c_0 & c_{-1} \\ 0 & \cdots & \cdots & 0 & c_{\frac{N}{2}} & \cdots & c_2 & c_1 & c_0 \end{bmatrix} \begin{bmatrix} \gamma_{-\frac{N}{2}} \\ \gamma_{-\frac{N}{2}+1} \\ \vdots \\ \gamma_{-1} \\ \gamma_0 \\ \gamma_1 \\ \vdots \\ \gamma_{\frac{N}{2}-1} \\ \gamma_{\frac{N}{2}} \end{bmatrix}$$

The result of this matrix vector multiplication is the vector $\vec{p}$. Each p_n coefficient is a vector dot product given by

F.2
$$\begin{aligned} p_n &= \sum_{k=0}^{2N+n} c_{\frac{N}{2}+n-k}\gamma_{k-\frac{N}{2}} \qquad -\tfrac{N}{2} \le n \le 0 \\ p_n &= \sum_{k=0}^{2N-n} c_{\frac{N}{2}-k}\gamma_{k-\frac{N}{2}+n} \qquad 0 > n \ge \tfrac{N}{2} \end{aligned}$$

It is important to note that the only p_n coefficient using all of the available information from both $\vec{c}$ and $\vec{\gamma}$ is p_0. The other coefficients in $\vec{p}$ are less accurate due to the truncated expansions of $\vec{c}$ and $\vec{\gamma}$. Thus to have an accurate Fourier convolution matrix for modes $-\frac{N}{2} \le n \le \frac{N}{2}$ requires a product of series having size $-N \le n \le N$. As with the Chebyshev convolution, the Fourier convolution matrix requires a vector twice the size of the final matrix. The actual convolution matrix representing $\vec{c}$ is

$$
\begin{bmatrix}
c_0 & c_{-1} & c_{-2} & \cdots & c_{-\frac{N}{2}} & c_{-\frac{N}{2}-1} & \cdots & \cdots & c_{-N} \\
c_1 & c_0 & c_{-1} & \cdots & c_{-\frac{N}{2}+1} & c_{-\frac{N}{2}} & c_{-\frac{N}{2}-1} & \cdots & c_{-N+1} \\
\vdots & & \ddots & & & & \ddots & \ddots & \vdots \\
c_{\frac{N}{2}-1} & \cdots & \cdots & c_0 & \cdots & \cdots & \cdots & c_{-\frac{N}{2}} & c_{-\frac{N}{2}-1} \\
c_{\frac{N}{2}} & c_{\frac{N}{2}-1} & \cdots & c_1 & c_0 & c_{-1} & \cdots & c_{-\frac{N}{2}+1} & c_{-\frac{N}{2}} \\
c_{\frac{N}{2}+1} & c_{\frac{N}{2}} & \cdots & \cdots & \cdots & c_0 & \cdots & \cdots & c_{-\frac{N}{2}+1} \\
\vdots & \ddots & \ddots & & & & \ddots & & \vdots \\
c_{N-1} & \cdots & c_{\frac{N}{2}+1} & c_{\frac{N}{2}} & c_{\frac{N}{2}-1} & \cdots & c_1 & c_0 & c_{-1} \\
c_N & \cdots & \cdots & c_{\frac{N}{2}+1} & c_{\frac{N}{2}} & \cdots & c_2 & c_1 & c_0
\end{bmatrix}
\begin{bmatrix}
\gamma_{-\frac{N}{2}} \\ \gamma_{-\frac{N}{2}+1} \\ \vdots \\ \gamma_{-1} \\ \gamma_0 \\ \gamma_1 \\ \vdots \\ \gamma_{\frac{N}{2}-1} \\ \gamma_{\frac{N}{2}}
\end{bmatrix}
=
\begin{bmatrix}
p_{-\frac{N}{2}} \\ p_{-\frac{N}{2}+1} \\ \vdots \\ p_{-1} \\ p_0 \\ p_1 \\ \vdots \\ p_{\frac{N}{2}-1} \\ p_{\frac{N}{2}}
\end{bmatrix}
$$

where the result is

F.3 $$p_n = \sum_{k=0}^{N} c_{\frac{N}{2}+n-k}\gamma_{k-\frac{N}{2}} \text{ for } -\tfrac{N}{2} \le n \le \tfrac{N}{2}.$$

With the convolution matrix defined for an exponential basis, we need convert from the exponential basis to the trigonometric basis. Using the standard form for the Fourier trigonometric expansion

F.4 $$\sum_{n=-N}^{N} c_n \mathrm{e}^{in\theta} = a_0 + \sum_{n=1}^{N} a_n \cos n\theta + b_n \sin n\theta$$

provides three cases to investigate

1) $n = 0$ -- resulting in $a_0 = c_0$

2) $1 \ge n \ge N$ -- then $\sum_{n=1}^{N} c_n \mathrm{e}^{in\theta} = \sum_{n=1}^{N} c_n \left(\cos n\theta + i \sin n\theta\right)$

3) $-N \le n \le -1$ (but make the following change of variables: $n = -n$ so the sum is $1 \to N$ as in case 2) - then $\sum_{n=1}^{N} c_{-n} \mathrm{e}^{-in\theta} = \sum_{n=1}^{N} c_{-n} \left(\cos n\theta - i \sin n\theta\right)$

Combining the above cases leads to the expansion

F.5 $$\sum_{n=-N}^{N} c_n \mathrm{e}^{in\theta} = c_0 + \sum_{n=1}^{N} \left[\left(c_n + c_{-n}\right)\cos n\theta + i\left(c_n - c_{-n}\right)\sin n\theta\right]$$

The results of interest obtained by equating F.4 and F.5 are $a_0 = c_0$, $a_n = c_n + c_{-n}$, and $b_n = i\left(c_n - c_{-n}\right)$. Rewriting the coefficient equations while solving for c_n and c_{-n} gives

F.6 $$c_n = \tfrac{a_n - ib_n}{2} \text{ and } c_{-n} = \tfrac{a_n + ib_n}{2}$$

Similarly we can write the coefficients for

$$\bar{\gamma} = \sum_{n=-\frac{N}{2}}^{\frac{N}{2}} \gamma_n e^{in\theta} = \alpha_0 + \sum_{n=1}^{N} \left(\alpha_n \cos n\theta + \beta_n \sin n\theta \right)$$

giving

F.7 $$\gamma_n = \tfrac{\alpha_n - i\beta_n}{2} \text{ and } \gamma_{-n} = \tfrac{\alpha_n + i\beta_n}{2}$$

Recall the form of the Fourier vectors in terms of the trigonometric basis then we need the form of the coefficients for the $\cos n\theta$ and $\sin n\theta$ terms. Consider the series product, $\bar{p}$, and its equivalent form using the trigonometric basis

F.8 $$\bar{p} = \sum_{n=-\frac{N}{2}}^{\frac{N}{2}} p_n e^{in\theta} = \mu_0 + \sum_{n=1}^{\frac{N}{2}} \left(\mu_n \cos n\theta + \eta_n \sin n\theta \right)$$

From the previous paragraph the trigonometric coefficients are given by $\mu_n = p_n + p_{-n}$ and $\eta_n = i\left(p_n - p_{-n}\right)$ where p_n and p_{-n} are given according to F.3 and c_n, c_{-n}, γ_n, and γ_{-n} are found in F.6 and F.7, respectively. Using these conversions between the exponential and trigonometric Fourier series in combination with the exponential Fourier convolution matrix gives the following trigonometric Fourier convolution matrix and product

$$\begin{bmatrix}
a_0 & \frac{1}{2}a_1 & \frac{1}{2}a_2 & \cdots & \frac{1}{2}a_{\frac{N}{2}} & 0 & \frac{1}{2}b_1 & \frac{1}{2}b_2 & \cdots & \frac{1}{2}b_{\frac{N}{2}} \\
a_1 & a_0 + \frac{1}{2}a_2 & \frac{1}{2}(a_1 + a_3) & \cdots & \frac{1}{2}\left(a_{\frac{N}{2}-1} + a_{\frac{N}{2}+1}\right) & 0 & \frac{1}{2}b_2 & \frac{1}{2}(b_1 + b_3) & \cdots & \frac{1}{2}\left(b_{\frac{N}{2}-1} + b_{\frac{N}{2}+1}\right) \\
a_2 & \frac{1}{2}(a_1 + a_3) & a_0 + \frac{1}{2}a_4 & \cdots & \frac{1}{2}\left(a_{\frac{N}{2}-2} + a_{\frac{N}{2}+2}\right) & 0 & \frac{1}{2}(b_3 - b_1) & \frac{1}{2}b_4 & \cdots & \frac{1}{2}\left(b_{\frac{N}{2}-2} + b_{\frac{N}{2}+2}\right) \\
\vdots & \vdots & \vdots & & \vdots & \vdots & \vdots & \vdots & & \vdots \\
a_{\frac{N}{2}} & \frac{1}{2}\left(a_{\frac{N}{2}-1} + a_{\frac{N}{2}+1}\right) & \frac{1}{2}\left(a_{\frac{N}{2}-2} + a_{\frac{N}{2}+2}\right) & \cdots & a_0 + \frac{1}{2}a_N & 0 & \frac{1}{2}\left(b_{\frac{N}{2}+1} - b_{\frac{N}{2}-1}\right) & \frac{1}{2}\left(b_{\frac{N}{2}+2} - b_{\frac{N}{2}-2}\right) & \cdots & \frac{1}{2}b_N \\
0 & \cdots & \cdots & \cdots & 0 & 0 & 0 & \cdots & \cdots & 0 \\
b_1 & \frac{1}{2}b_2 & \frac{1}{2}(b_3 - b_1) & \cdots & \frac{1}{2}\left(b_{\frac{N}{2}+1} - b_{\frac{N}{2}-1}\right) & 0 & a_0 - \frac{1}{2}a_2 & \frac{1}{2}(a_1 - a_3) & \cdots & \frac{1}{2}\left(a_{\frac{N}{2}-1} - a_{\frac{N}{2}+1}\right) \\
b_2 & \frac{1}{2}(b_1 + b_3) & \frac{1}{2}b_4 & \cdots & \frac{1}{2}\left(b_{\frac{N}{2}+2} - b_{\frac{N}{2}-2}\right) & 0 & \frac{1}{2}(a_1 - a_3) & a_0 - \frac{1}{2}a_4 & \cdots & \frac{1}{2}\left(a_{\frac{N}{2}-2} - a_{\frac{N}{2}+2}\right) \\
\vdots & \vdots & \vdots & & \vdots & \vdots & \vdots & \vdots & & \vdots \\
b_{\frac{N}{2}} & \frac{1}{2}\left(b_{\frac{N}{2}-1} + b_{\frac{N}{2}+1}\right) & \frac{1}{2}\left(b_{\frac{N}{2}-2} + b_{\frac{N}{2}+2}\right) & \cdots & \frac{1}{2}b_N & 0 & \frac{1}{2}\left(a_{\frac{N}{2}-1} - a_{\frac{N}{2}+1}\right) & \frac{1}{2}\left(a_{\frac{N}{2}-2} - a_{\frac{N}{2}+2}\right) & \cdots & a_0 - \frac{1}{2}a_N
\end{bmatrix}
\begin{bmatrix} \alpha_0 \\ \alpha_1 \\ \alpha_2 \\ \vdots \\ \alpha_{\frac{N}{2}} \\ 0 \\ \beta_1 \\ \beta_2 \\ \vdots \\ \beta_{\frac{N}{2}} \end{bmatrix}$$

The trigonometric Fourier convolution matrix consists of four distinct blocks with each block having size $\left(\frac{N}{2}+1\right) \times \left(\frac{N}{2}+1\right)$. Each blocks is produced by the cosine or sine

coefficients of a Fourier vector containing $N+1$ entries. The Fourier convolution matrix applies to vectors written in the full form. Consider the generic expansion

$$\bar{\zeta}(r,\theta)=\sum_{n=0}^{\frac{N}{2}}\left(\bar{\zeta}_n^c(r)\cos n\theta+\bar{\zeta}_n^c(r)\sin n\theta\right)$$

where ζ is either stream function or vorticity (ψ or ω) and $\bar{\zeta}_n^c(r)$ and $\bar{\zeta}_n^s(r)$ are the Chebyshev coefficient vectors for the n^{th} Fourier cosine and sine modes. Translating the above expression into a vector of coefficients yields the full vector form

$$\bar{\zeta}(r,\theta)=\begin{bmatrix}\bar{\zeta}_0^c(r) & \bar{\zeta}_1^c(r) & \cdots & \bar{\zeta}_{\frac{N}{2}}^c(r) & 0 & \bar{\zeta}_1^s(r) & \bar{\zeta}_2^s(r) & \cdots & \bar{\zeta}_{\frac{N}{2}}^s(r)\end{bmatrix}^{\mathbf{T}}$$

where the elements for the Fourier vector are the Chebyshev coefficient vectors. To produce a convolution matrix for the full vector requires two steps. First the Fourier convolution matrix is constructed from the Chebyshev coefficient vectors. As a result every element of the Fourier convolution matrix is a coefficient vector. In the second step each Chebyshev coefficient vector is expanded as a convolution matrix per appendix E.

An example for our problem: consider the expansions for the perturbed vorticity and stream function

$$\bar{\omega}_1(r,\theta)=\begin{bmatrix}\bar{\omega}_{0;1}^c(r) & \bar{\omega}_{1;1}^c(r) & \cdots & \bar{\omega}_{\frac{N}{2};1}^c(r) & 0 & \bar{\omega}_{1;1}^s(r) & \bar{\omega}_{2;1}^s(r) & \cdots & \bar{\omega}_{\frac{N}{2};1}^s(r)\end{bmatrix}^{\mathbf{T}}$$

$$\bar{\psi}_1(r,\theta)=\begin{bmatrix}\bar{\psi}_{0;1}^c(r) & \bar{\psi}_{1;1}^c(r) & \cdots & \bar{\psi}_{\frac{N}{2};1}^c(r) & 0 & \bar{\psi}_{1;1}^s(r) & \bar{\psi}_{2;1}^s(r) & \cdots & \bar{\psi}_{\frac{N}{2};1}^s(r)\end{bmatrix}^{\mathbf{T}}$$

The convolution terms are entirely represented by considering $\hat{\mathbf{R}}\hat{\mathbf{Q}}\bar{\psi}_0 \underset{F}{*} \hat{\mathbf{D}}\bar{\omega}_1$. This term is a convolution of the vectors $\hat{\mathbf{R}}\hat{\mathbf{Q}}\bar{\psi}_0$ and $\hat{\mathbf{D}}\bar{\omega}_1$. The application of the $\hat{\mathbf{Q}}$ matrix swaps the cosine and sine terms in $\bar{\psi}_0$ while applying the appropriate scaling and sign adjustment

$$\hat{\mathbf{Q}}\bar{\psi}_0=\begin{bmatrix}0 & \bar{\psi}_{1;0}^s & 2\bar{\psi}_{2;0}^s & \cdots & \frac{N}{2}\bar{\psi}_{\frac{N}{2};0}^s & 0 & -\bar{\psi}_{1;0}^c & -2\bar{\psi}_{2;0}^c & \cdots & -\frac{N}{2}\bar{\psi}_{\frac{N}{2};0}^c\end{bmatrix}^{\mathbf{T}}$$

Since the $\hat{\mathbf{R}}$ and $\hat{\mathbf{D}}$ matrices are block diagonal they apply to the inner Chebyshev vectors without introducing any cross vector interaction within the Fourier space. The final forms of the $\hat{\mathbf{R}}\hat{\mathbf{Q}}\bar{\psi}_0$ and $\hat{\mathbf{D}}\bar{\omega}_1$ vectors are

$$\hat{\mathbf{R}}\hat{\mathbf{Q}}\bar{\psi}_0=\begin{bmatrix}0 & \mathbf{R}\bar{\psi}_{1;0}^s & 2\mathbf{R}\bar{\psi}_{2;0}^s & \cdots & \frac{N}{2}\mathbf{R}\bar{\psi}_{\frac{N}{2};0}^s & 0 & -\mathbf{R}\bar{\psi}_{1;0}^c & -2\mathbf{R}\bar{\psi}_{2;0}^c & \cdots & -\frac{N}{2}\mathbf{R}\bar{\psi}_{\frac{N}{2};0}^c\end{bmatrix}$$

$$\hat{\mathbf{D}}\bar{\omega}_1 = \begin{bmatrix} \mathbf{D}\bar{\omega}^c_{0;1} & \mathbf{D}\bar{\omega}^c_{1;1} & \mathbf{D}\bar{\omega}^c_{2;1} & \cdots & \mathbf{D}\bar{\omega}^c_{\frac{N}{2};1} & 0 & \mathbf{D}\bar{\omega}^c_{1;1} & \mathbf{D}\bar{\omega}^c_{2;1} & \cdots & \mathbf{D}\bar{\omega}^s_{\frac{N}{2};1} \end{bmatrix}^{\mathbf{T}}$$

Returning to the convolution, $\hat{\mathbf{R}}\hat{\mathbf{Q}}\bar{\psi}_0 \underset{F}{*} \hat{\mathbf{D}}\bar{\omega}_1$, the Fourier convolution matrix for $\hat{\mathbf{R}}\hat{\mathbf{Q}}\bar{\psi}_0$ can be constructed in the manner described above. This convolution matrix is written as $\overline{\hat{\mathbf{R}}\hat{\mathbf{Q}}\bar{\psi}_0} = \begin{bmatrix} \mathbf{F}_{11} & \mathbf{F}_{12} \\ \mathbf{F}_{21} & \mathbf{F}_{22} \end{bmatrix}$ and the blocks of this matrix are

$$\mathbf{F}_{11} = \begin{bmatrix} 0 & \frac{1}{2}\mathbf{R}\bar{\psi}^s_{1;0} & \hat{\mathbf{R}}\bar{\psi}^s_{2;0} & \cdots & \frac{N}{4}\hat{\mathbf{R}}\bar{\psi}^s_{\frac{N}{2};0} \\ \mathbf{R}\bar{\psi}^s_{1;0} & \mathbf{R}\bar{\psi}^s_{2;0} & \mathbf{R}\left(\frac{1}{2}\bar{\psi}^s_{1;0} + \frac{3}{2}\bar{\psi}^s_{3;0}\right) & \cdots & \mathbf{R}\left(\frac{(N-2)}{4}\bar{\psi}^s_{\frac{N}{2}-1;0} + \frac{(N+2)}{4}\bar{\psi}^s_{\frac{N}{2}+1;0}\right) \\ 2\mathbf{R}\bar{\psi}^s_{2;0} & \mathbf{R}\left(\frac{1}{2}\bar{\psi}^s_{1;0} + \frac{3}{2}\bar{\psi}^s_{3;0}\right) & 2\mathbf{R}\bar{\psi}^s_{4;0} & \cdots & \mathbf{R}\left(\frac{(N-4)}{4}\bar{\psi}^s_{\frac{N}{2}-2;0} + \frac{(N+4)}{4}\bar{\psi}^s_{\frac{N}{2}+2;0}\right) \\ \vdots & \vdots & \vdots & & \vdots \\ \frac{N}{2}\mathbf{R}\bar{\psi}^s_{\frac{N}{2};0} & \mathbf{R}\left(\frac{(N-2)}{4}\bar{\psi}^s_{\frac{N}{2}-1;0} + \frac{(N+2)}{4}\bar{\psi}^s_{\frac{N}{2}+1;0}\right) & \mathbf{R}\left(\frac{(N-4)}{4}\bar{\psi}^s_{\frac{N}{2}-2;0} + \frac{(N+4)}{4}\bar{\psi}^s_{\frac{N}{2}+2;0}\right) & \cdots & \frac{N}{2}\mathbf{R}\bar{\psi}^s_{N;0} \end{bmatrix}$$

$$\mathbf{F}_{12} = \begin{bmatrix} 0 & -\frac{1}{2}\mathbf{R}\bar{\psi}^c_{1;0} & -\mathbf{R}\bar{\psi}^c_{2;0} & \cdots & -\frac{N}{4}\mathbf{R}\bar{\psi}^c_{\frac{N}{2};0} \\ 0 & -\mathbf{R}\bar{\psi}^c_{2;0} & -\mathbf{R}\left(\frac{1}{2}\bar{\psi}^c_{1;0} + \frac{3}{2}\bar{\psi}^c_{3;0}\right) & \cdots & -\mathbf{R}\left(\frac{(N-2)}{4}\bar{\psi}^c_{\frac{N}{2}-1;0} + \frac{(N+2)}{4}\bar{\psi}^c_{\frac{N}{2}+1;0}\right) \\ 0 & \mathbf{R}\left(\frac{1}{2}\bar{\psi}^c_{1;0} - \frac{3}{2}\bar{\psi}^c_{3;0}\right) & -2\mathbf{R}\bar{\psi}^c_{4;0} & \cdots & -\mathbf{R}\left(\frac{(N-4)}{4}\bar{\psi}^c_{\frac{N}{2}-2;0} + \frac{(N+4)}{4}\bar{\psi}^c_{\frac{N}{2}+2;0}\right) \\ \vdots & \vdots & \vdots & & \vdots \\ 0 & \mathbf{R}\left(\frac{(N-2)}{4}\bar{\psi}^c_{\frac{N}{2}-1;0} - \frac{(N+2)}{4}\bar{\psi}^c_{\frac{N}{2}+1;0}\right) & \mathbf{R}\left(\frac{(N-4)}{4}\bar{\psi}^c_{\frac{N}{2}-2;0} - \frac{(N+4)}{4}\bar{\psi}^c_{\frac{N}{2}+2;0}\right) & \cdots & -\frac{N}{2}\mathbf{R}\bar{\psi}^c_{N;0} \end{bmatrix}$$

$$\mathbf{F}_{21} = \begin{bmatrix} 0 & 0 & 0 & \cdots & 0 \\ -\mathbf{R}\bar{\psi}^c_{1;0} & -\mathbf{R}\bar{\psi}^c_{2;0} & \mathbf{R}\left(\frac{1}{2}\bar{\psi}^c_{1;0} - \frac{3}{2}\bar{\psi}^c_{3;0}\right) & \cdots & \mathbf{R}\left(\frac{(N-2)}{4}\bar{\psi}^c_{\frac{N}{2}-1;0} - \frac{(N+2)}{4}\bar{\psi}^c_{\frac{N}{2}+1;0}\right) \\ -2\mathbf{R}\bar{\psi}^c_{2;0} & -\mathbf{R}\left(\frac{1}{2}\bar{\psi}^c_{1;0} + \frac{3}{2}\bar{\psi}^c_{3;0}\right) & -2\mathbf{R}\bar{\psi}^c_{4;0} & \cdots & \mathbf{R}\left(\frac{(N-4)}{4}\bar{\psi}^c_{\frac{N}{2}-2;0} - \frac{(N+4)}{4}\bar{\psi}^c_{\frac{N}{2}+2;0}\right) \\ \vdots & \vdots & \vdots & & \vdots \\ -\frac{N}{2}\mathbf{R}\bar{\psi}^c_{\frac{N}{2};0} & -\mathbf{R}\left(\frac{(N-2)}{4}\bar{\psi}^c_{\frac{N}{2}-1;0} + \frac{(N+2)}{4}\bar{\psi}^c_{\frac{N}{2}+1;0}\right) & -\mathbf{R}\left(\frac{(N-4)}{4}\bar{\psi}^c_{\frac{N}{2}-2;0} + \frac{(N+4)}{4}\bar{\psi}^c_{\frac{N}{2}+2;0}\right) & \cdots & -\frac{N}{2}\mathbf{R}\bar{\psi}^c_{N;0} \end{bmatrix}$$

$$\mathbf{F}_{22} = \begin{bmatrix} 0 & 0 & 0 & \cdots & 0 \\ 0 & -\mathbf{R}\psi^s_{2;0} & \mathbf{R}\left(\frac{1}{2}\psi^s_{1;0} - \frac{3}{2}\psi^s_{3;0}\right) & \cdots & \mathbf{R}\left(\frac{(N-2)}{4}\psi^s_{\frac{N}{2}-1;0} - \frac{(N+2)}{4}\psi^s_{\frac{N}{2}+1;0}\right) \\ 0 & \mathbf{R}\left(\frac{1}{2}\psi^s_{1;0} - \frac{3}{2}\psi^s_{3;0}\right) & -2\mathbf{R}\psi^s_{4;0} & \cdots & \mathbf{R}\left(\frac{(N-4)}{4}\psi^s_{\frac{N}{2}-2;0} - \frac{(N+4)}{4}\psi^s_{\frac{N}{2}+2;0}\right) \\ \vdots & \vdots & \vdots & & \vdots \\ 0 & \mathbf{R}\left(\frac{(N-2)}{4}\psi^s_{\frac{N}{2}-1;0} - \frac{(N+2)}{4}\psi^s_{\frac{N}{2}+1;0}\right) & \mathbf{R}\left(\frac{(N-4)}{4}\psi^s_{\frac{N}{2}-2;0} - \frac{(N+4)}{4}\psi^s_{\frac{N}{2}+2;0}\right) & \cdots & -\frac{N}{2}\mathbf{R}\psi^s_{N;0} \end{bmatrix}$$

However, this representation is misleading as each element of $\mathbf{F}$ appears to be an $(M+1)\times 1$ Chebyshev vector. In reality these vectors must be replaced by the appropriate $(M+1)\times(M+1)$ Chebyshev convolution matrices e.g. $\mathbf{R}\bar{\psi}^s_{1;0}$ must be replaced by the Chebyshev convolution matrix $\overline{\mathbf{R}\bar{\psi}^s_{1;0}}$ using the method described in appendix E. Recall the definitions of the Fourier vector functions

$$\vec{\psi}^{c}_{0;n}(r) = \sum_{m=0}^{M} \psi^{c}_{n,m;0} T_m(r)$$

$$\vec{\psi}^{s}_{0;n}(r) = \sum_{m=0}^{M} \psi^{s}_{n,m;0} T_m(r)$$

The Chebyshev convolution matrix resulting from the vector $\mathbf{R}\vec{\psi}^{c}_{n;0}$ is given by

$$\mathbf{Y}_{\vec{\psi}^{c}_{n;0}} = \sum_{m=0}^{2M} \mathbf{T}_m \mathbf{R} \vec{\psi}^{c}_{n,m;0} .$$

The $\mathbf{Y}_{\vec{\psi}^{c}_{n;0}}$ matrix is cropped to $(M+1)\times(M+1)$ as to contain the full data for a $(2M+1)\times 1$ vector. $\mathbf{R}\vec{\psi}^{s}_{n;0}$ has a similar convolution matrix, $\mathbf{Y}_{\vec{\psi}^{s}_{n;0}}$.

After the Fourier convolution matrix, $\overline{\hat{\mathbf{R}}\hat{\mathbf{Q}}\vec{\psi}_0}$, is formed, multiplication by the Chebyshev differentiation matrix yields $\overline{\hat{\mathbf{R}}\hat{\mathbf{Q}}\vec{\psi}_0}\hat{\mathbf{D}}$. Since $\hat{\mathbf{D}}$ is block diagonal each element of $\overline{\hat{\mathbf{R}}\hat{\mathbf{Q}}\vec{\psi}_0}\hat{\mathbf{D}}$ has the form $\mathbf{Y}_{\vec{\psi}^{c}_{n;0}}\mathbf{D}$ or $\mathbf{Y}_{\vec{\psi}^{s}_{n;0}}\mathbf{D}$, a matrix product of the Chebyshev convolution matrix, $\mathbf{Y}_{\vec{\psi}^{c}_{0;n}}$ or $\mathbf{Y}_{\vec{\psi}^{s}_{0;n}}$, and the Chebyshev differentiation matrix $\mathbf{D}$. This is the final form of the matrix as a product with the unknown vector, $\vec{\omega}_1$.

BIBLIOGRAPHY

[1] Ascher, U.M., Ruuth, S.J., & Wetton, B.T.R. *Implicit-explicit Methods for Time-dependent PDEs*, (1995), SIAM J. Numer. Anal., **32**, pp. 797-823.

[2] Batchelor, G.K. *An introduction to Fluid Dynamics*, (1967), Cambridge University Press, Cambridge, UK.

[3] Bergeron, K., Coutsias, E.A., Lynov, J.P., & Nielsen A.H. *Self-organization in Circular Shear Layers*, (1996), Physica Scripta **T67**, pp. 33-37.

[4] Canuto, C., Hussaini, M.Y., Quarteroni, A., & Zang, T.A. *Spectral Methods in Fluid Dynamics*, (1988), Springer-Verlag, Springer Series in Computational Physics, New York, NY.

[5] Chandrasekhar, S. *Hydrodynamic and Hydromagnetic Stability*, (1981), Dover, New York, NY.

[6] Chomaz, J.M., Rabaud, M., Basdevant, C., & Couder, Y. *Experimental and Numerical Investigation of a Forced Circular Shear Layer*, (1988), J. Fluid Mech. **187**, pp.115-140.

[7] Churilov, S.M. & Shukhman, I.G. *Weakly Nonlinear Theory of the Alternation of Modes in a Circular Shear Flow*, (1992), J. Fluid Mech. **243**, pp. 155-169.

[8] Coutsias, E.A., & Lynov, J.P. *Fundamental Interactions of Vortical Structures with Boundary Layers in Two-dimensional Flows*, (1991), Physica D **51**, pp. 482-497.

[9] Danilov, S.D., Dolzhanskii, F.V., Dovshenko, V.A., & Krymov, V.A. *An Advanced Investigation of Interaction of Allocated Quasi-two-dimensional Vortices*, (1996), Chaos, Vol. 6, No. 3, pp. 297-308.

[10] Dolzhanskii, F.V. *On the Effect of External Friction on the Stability of Plane Parallel Shear Flows*, (1987), Izv. Acad. Sci. USSR Atmos. Ocean. Phys. **23**, pp. 348-356.

[11] Dolzhanskii, F.V., Krymov, V.A., & Manin, D.Y. *An Advanced Experimental Investigation of Quasi-two-dimensional Shear Flows*, (1992), J. Fluid Mech. **241**, pp. 705-722.

[12] Drazin, P.G. & Reid, W.H. *Hydrodynamic Stability*, (1981), Cambridge University Press, Cambridge, UK.

[13] Fornberg, B. *A Practical Guide to Pseudospectral Methods*, (1998), Cambridge University Press, Cambridge, UK.

[14] Früh, W. *personal note to A. H. Nielsen*, (2001)

[15] Früh, W. & Read, P.L., *Experiments on a Barotropic Rotating Shear Layer. Part 1. Instability and Steady Vortices*, (1999), J. Fluid Mech. **383**, pp. 143-173.

[16] Gottlieb, D. & Orszag, S.A. *Numerical Analysis of Spectral Methods: Theory and Applications*, (1977), SIAM, CBMS-NSF Reg. Conf. Ser. in Appl. Math. **26**, Philidelphia, PA.

[17] Greenspan, H.P. The Theory of Rotating Fluids, (1968), Cambridge University Press, Cambridge, UK.

[18] Hide, R. & Titman, C.W. *Detached Shear Layers in a Rotating Fluid*, (1967), J. Fluid Mech. **29**, pp. 39-60.

[19] Humphrey, J.A.C., & Gore, D. *Experimental Observations of an Unsteady Detached Shear Layer in Enclosed Corotating Disk Flow*, (1993), Phys. Fluids A **5**, pp. 2438-2442.

[20] Konijnenberg, J.A. van de, Nielsen, A.H., Rasmussen, J.J., & Stenum, B. *Shear-flow Instability in a Rotating Fluid*, (1999), J. Fluid Mech. 387, pp. 177-204.

[21] Manin, D. *Characteristic Size of Vortices in Developed Quasi-two-dimensional Flows*, (1990), Izv. Akad. Nauk. SSSR. Atmos. Ocean. Phys. 26 (6), pp. 426-429.

[22] Matsushima, T. & Marcus, P.S. A Spectral Method for Polar Coordinates, (1995), J. Comput. Phys. **120**, pp. 365-374.

[23] Niino, H. & Misawa, N. *An Experimental and Theoretical Study of Barotropic Instability*, (1984), J. Atmos. Sci. 41, pp. 1992-2011.

[24] Pedlosky, J. *Geophysical Fluid Dynamics*, (1987), Springer-Verlag, New York, NY.

[25] Rabaud, M. & Couder, Y. *A Shear-flow Instability in a Circular Geometry*, (1983), J. Fluid Mech. **136**, pp. 291-319.

[26] Rand, D., *Dynamics and Symmetry. Predictions for Modulated Waves in Rotating Fluids*, (1982), Arch. Rat. Mech. Anal. **79**, pp. 1-37.

[27] Read, P.L., Bell, M.J., Johnson, D.W., & Small, R.M. *Quasi-periodic and Chaotic Flow Regimes in a Thermally-driven, Rotating Fluid Annulus*, (1992), J. Fluid Mech. **238**, pp. 599-632.

[28] Schär, C. & Davies, H.C. *An Instability of Mature Cold Fronts*, (1990), J. Atmos. Sci. **47**, pp. 929-950.

[29] Simmons, A.J. & Hoskins, B.J. *The Life Cycles of Some Nonlinear Baroclinic Waves*, (1978), J. Atmos. Sci. **35**, pp. 414-432.

[30] Stewartson, K. *On Almost Rigid Rotations*, (1957), J. Fluid Mech. **3**, pp. 17-26.

[31] Tomasini, M., Dolez, N., & Léorat J. Instability of a Rotating Shear Layer in the Transonic Regime, (1996), J. Fluid Mech. **306**, pp. 59-82.

[32] Torres, D.J. & Coutsias, E.A. *Pseudospectral Solution of the Two-dimensional Navier-Stokes equations in a Disk*, (1998), SIAM J. Sci. Comp., Vol. 21, No. 1, pp. 378-403

[33] Trefethen, L.N., Trefethen, A.E., & Reddy, S.C. *Pseudospectra of the Linear Navier-Stokes Evolution Operator and Instability of Plane Poiseuille and Couette Flows*, (1992), TR 92-1291, Cornell University, Ithica, NY.

[34] Weber, H.C., & Smith, R.K. *The Stability of Barotropic Vortices – Implications for Tropical Cyclone Motion*, (1993), Geophys. Astrophys. Fluid Dyn. 70, pp. 1-30.

[35] Winant, C.D. & Browand, F.K. *Vortex Pairing: the Mechanism of Turbulent Mixing-layer Growth at Moderate Reynolds Number*, (1974), J. Fluid Mech. **63**, pp. 237.

[36] Yao, H.B. & Zabusky, N.J. *Axisymmetrization of an Isolated Vortex Region by Splitting and Partial Merging of Satellite Depletion Perturbations*, (1996) Phys. Fluids **8** (7), pp. 1842-1847.